Development of Optical Field Emitter Arrays

by

Yujia Yang

B.S. Electronics Science & Technology
Zhejiang University, 2011

SUBMITTED TO THE DEPARTMENT OF ELECTRICAL ENGINEERING AND COMPUTER SCIENCE IN PARTIAL FULFILLMENT OF THE REQUIREMENTS FOR THE DEGREE OF

MASTER OF SCIENCE IN ELECTRICAL ENGINEERING AND COMPUTER SCIENCE

AT THE

MASSACHUSETTS INSTITUTE OF TECHNOLOGY

SEPTEMBER 2013

Signature of Author: _____
Department of Electrical Engineering and Computer Science
August 30, 2013

Certified by: _____
Karl K. Berggren
Professor of Electrical Engineering and Computer Science
Thesis Supervisor

Accepted by: _____
Leslie A. Kolodziejski
Professor of Electrical Engineering and Computer Science
Chairman of the Committee on Graduate Students

Development of Optical Field Emitter Arrays

by

Yujia Yang

Submitted to the Department of Electrical Engineering and Computer Science on August 30, 2013 in Partial Fulfillment of the Requirements for the Degree of Master of Science in Electrical Engineering and Computer Science

ABSTRACT

Optical field emitters are electron emission sources actuated by incident light. Optically actuated field emitters may produce ultrafast pulses of electrons when excited by ultrafast optical pulses, thus making them of interest for specific applications such as ultrafast electron microscopy, diffraction and spectroscopy; and as electron sources for X-ray generation. Recently proposed intense, coherent, and compact X-ray sources require low emittance, high brightness and short duration electron bunches that form a periodic pattern in the transverse plane. This thesis theoretically developed optical field emitter arrays that are suitable for use as the electron source for this novel X-ray source. Studies of several optical field emitter array structures, including vertically-standing gold nanopillars and silicon tips, in-plane gold nanostructures, and metallic line gratings, were performed via theoretical analysis and numerical simulations. Enhancement of the optical near-field and power absorption was achieved by geometrical and plasmonic effects, leading to enhanced charge yield from the optical field emitter arrays.

Thesis Supervisor: Karl K. Berggren

Title: Professor of Electrical Engineering and Computer Science

Acknowledgements

First of all, I would like to express the deepest appreciation to my research supervisor, Prof. Karl Berggren, for his invaluable assistance, guidance and suggestions during the past two years of my graduate study. Without Karl, I would never have the chance to enter the wonderful nano-world and immerse myself in the beauty of nanoscience and nanotechnology, and the work in this thesis would have been impossible. And congratulations to Karl on his recent appointment as a full professor!

I would also like to express my sincere thanks to Dr. Richard Hobbs for his effort in developing the fabrication process and preparing most of the samples, his valuable discussions on my research work, his important suggestions on revising this thesis, and his patient guidance to improve my cleanroom experience and lab skills.

In addition to Karl and Richard, I would like to thank all the people on the project *Compact and Ultrafast Bright and Intense X-ray sources* (CUBIX), including but not limited to, Prof. Franz Kaertner, Dr. William Graves, Dr. Luis Velasquez-Garcia, Dr. Michael Swanwick, Dr. Arya Fallahi, Donnie Keathley and Eva De Leo. Their discussions and suggestions greatly improved my work.

Besides, I am grateful to Jim Daley, Mark Mondol and other NanoStructure Laboratory (NSL) staff for running a great lab where the samples were fabricated, and to Tim McClure for training me on UV-Vis measurement that optically characterized the samples.

Additionally, I would like to express my gratitude to Prof. James Fujimoto, my academic advisor and the lecturer of the course *6.631 Optics and Photonics*, for making me clear about and reminding me of the timeline of graduate study in EECS, MIT and giving me excellent lectures on optics, and to Prof. Terry Orlando for kindly guiding me through the process of finding a research home and releasing my confusion when I first started my graduate study two years ago.

Moreover, I want to thank all my colleagues, labmates, classmates and friends for bringing inspirations, knowledge and happiness to my graduate school experience.

In terms of funding, I would like to appreciate Jin Au Kong Memorial Fellowship for supporting my graduate study in Fall 2011 and DARPA for supporting the CUBIX project.

Finally, I am truly indebted to my Mom and Dad living thousands of miles away in China. Despite the distance between us, their love and support are always around me and beyond words can describe.

Contents

List of Figures

Chapter 1: Introduction

1.1 Electron Field Emission and Field Emitter Arrays (FEAs)

Electron field emission (also known as field emission, field electron emission and field-induced electron emission) refers to the phenomenon that materials emit electrons under a strong electric field. The devices that field-emit electrons are called field emitters. Generally speaking, the field emission materials can be of solid, liquid as well as molecular and atomic forms, but here we primarily focus on electron emission from solids, especially metals and semiconductors since sufficient supply of electrons is needed.

Electrons are held in solids or molecules by Coulombic forces due to the positive charge on the nuclei of atoms within. Extraction of electrons from a solid thus requires energy which has to be supplied to the electrons to overcome the material work function and escape to vacuum. The energy source can be heat or incident photons, with the corresponding electron emission phenomena termed thermionic emission and photoelectric effect, respectively. However, electrons can also escape a work function barrier via quantum tunneling, where no extra energy is required. The basic idea of field emission is to induce a strong electric field at the material surface, which reduces the thickness of a work function barrier and facilitates electron tunneling. As the energy of tunneling electrons is around the Fermi level (for metals) or the conduction band edge (for semiconductors) that is well below the vacuum energy level, field emission is also called cold field emission.

Field emission has a long history, dating back even before J. J. Thomson's identification of the electron [1]. The well-known electrical discharge around a sharp point, the so-called "lightning rod effect", is an example of field emission, where the small radius geometry of an electrically conducting material causes electric field line crowding and enhances the field strength at the tip, inducing electron emission. The first quantum mechanical explanation of field emission was proposed by R. H. Fowler and L. W. Nordheim [2], after whom the "Fowler-Nordheim equations" are named. Although this theoretical treatment was derived for bulk metals, it remains as a reasonably good approximation for various materials and emitter architectures.

Electron field emission has a wide range of applications. One example is the vacuum tubes, the building blocks of first generation electric computers. Another example is electron-gun sources. Modern high resolution micro-/nano- metrology and fabrication tools, such as scanning electron microscopy (SEM), transmission electron microscopy (TEM) and electron beam lithography (EBL), all benefit from a high brightness electron source, where field emission is advantageous over thermionic and Schottky emission (combination of thermal and field induced emission). Electron field emission sources are also widely used in particle accelerators.

A field emitter array (FEA) is an array of a large number of individual field emitters. It is a large-area field emission source capable of generating a field emission current thousands and even millions of times larger than that from an individual field emitter. The first form of FEAs was the Spindt array, named after the inventor, C. A. Spindt, consisting of an array of sharp, conical-shaped molybdenum tips embedded inside holes of an oxide film, on which an extraction gate was deposited [3]. The FEA is compatible with standard silicon-integrated-circuit fabrication techniques and has potential applications in field emission displays and multi-beam electron-beam lithography.

1.2 Photo-induced Electron Emission and Optical Field Emitters

Electron field emission can be achieved by applying a static electric field as well as optical illumination. Optical field emitters, also named as photocathodes, are electron emission sources excited by incident light.

A monochromatic continuous electromagnetic wave can be treated as a time-harmonically oscillating electric field at the emission site, and thus it is capable of inducing electron emission as long as the electric field amplitude is sufficient. The underlying physical mechanism is complicated by the photoelectric effect, where electrons are excited through the absorbing of photons. It is important to differentiate optical field emission, where the strong electric field associated with the electromagnetic wave induces electron emission, from single/multi-photon emission, where the energy of a single, or multiple, photons is absorbed by an electron allowing it to overcome the work function barrier.

Optical field emitters are superior to conventional static field emitters as ultrafast electron sources, from which the electron bunches have a temporal duration of picosecond and even femtosecond time scale. For static field emitters, the switching speed of control electronics is too low to achieve ultrafast electron emission, whereas optical field emitters can be triggered by a picosecond or femtosecond laser to generate electron bunches with very short time span, which is favored by specific applications such as ultrafast electron diffraction [4][5] and ultrafast electron microscopy [5][6].

Optical field emitter arrays can be used as the electron sources for X-ray generation. Short wavelength radiations such as X-rays can be produced by illuminating relativistic electrons with longer wavelength lasers. The energy is transferred from high energy, relativistic electrons to low energy, long wavelength photons and hence high energy, short wavelength photons are generated, a mechanism called inverse Compton scattering (ICS). Very recently, Graves *et al.* proposed an idea of intense, coherent and compact X-ray sources [7]. It starts with periodically bunched electrons accelerated to relativistic speed, and the transverse periodicity is then converted to longitudinal density modulation via emittance exchange, from which X-rays can be generated by ICS (Fig. 1.1). This emittance exchange ICS X-ray source requires low emittance, high brightness and short duration electron bunches that form a periodic pattern in the transverse plane. Therefore, nanoengineered and femtosecond laser actuated optical field emitter array is an ideal option as the electron source for this application.

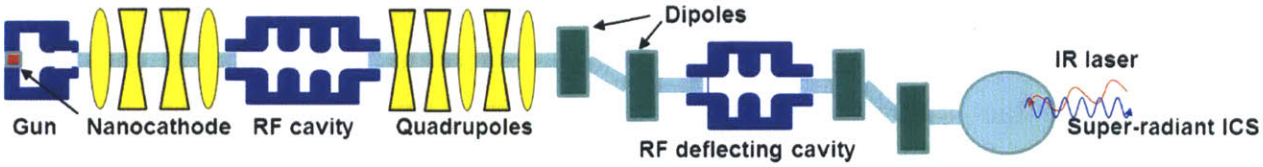

Fig. 1.1. Layout of the emittance exchange ICS X-ray source [7]. Key components are (from left to right): nano-photocathode, RF acceleration cavity, quadrupoles for emittance exchange, and inverse Compton scattering (ICS).

1.3 Metallic Photocathodes and Surface Plasmon Resonance

Photocathodes can be made of either metals or semiconductors. Semiconductor photocathodes usually have high quantum efficiency, but suffer from current saturation due to electron depletion and finite response time due to electron

velocity saturation and transit time in the depletion region. The response time can be worsened by inclusion of electron diffusion time if both depletion region and neutral region are illuminated. Moreover, since surface states and contaminations can dramatically change the electronic and optoelectronic properties of semiconductors, ultra high vacuum is required for semiconductor photocathodes. Metallic photocathodes, on the other hand, have short response times and reduced vacuum requirements due to their robustness. But their efficiency is usually low. For instance, the quantum efficiency of copper, a commonly used material for metallic photocathodes, is on the order of 10^{-5}.

One way to enhance the efficiency of metallic photocathodes is to excite surface plasmon resonances. The strong electric field required in electron emission is usually achieved via the lightning rod effect, where a sharp structure crowds the equipotential lines. Since the electric field strength is proportional to the equipotential line density, the field is enhanced around the structure. As for photoelectron emission from metals, an additional mechanism, surface plasmon resonance, helps to assist field enhancement and electron emission.

Surface plasmon resonance refers to the collective oscillation of electrons in a solid coupled with oscillating electromagnetic fields and is confined at the surface of the solid. A strongly enhanced electric near-field is always associated with the surface plasmon resonance. Both the field enhancement and field localization are favored by optical field emitter arrays, since the charge yield of the emitters can be greatly improved. The materials generally used in surface plasmon resonance applications at optical frequencies are metals with high electrical conductivity such as Au, Ag, Cu, and Al, due to their negative dielectric permittivities in the visible frequency range and the fact that damping of surface plasmon resonance in these metals is minimal so that the resonance has a long life time (up to tens of femtoseconds) and a long propagation distance (up to tens of micrometers). Among them, noble metals like Au and Ag are ideal choices because their resistance to oxidation and corrosion can improve the robustness and lifetime of the optical field emitter arrays.

There are two key elements in the area of surface plasmon resonance, surface plasmon polariton (SPP) and localized surface plasmon resonance (LSPR). The former refers to the propagating surface plasmon wave confined at a metal/dielectric interface, while the latter the plasmon resonance localized at the

surface of a nanoscale metallic particle. Both SPP and LSPR can be utilized to enhance the electric field of optical field emitters.

1.4 Previous Work on Optical Field Emitters

Photoelectron emission from a single metallic optical field emitter, especially the emission of femtosecond-scale electron pulses, has been intensively studied recently to reveal the underlying physics of electron emission triggered by the interaction between ultrafast laser pulses and electron emitters. Hommelhoff *et al.* first studied this phenomenon by illuminating a tungsten tip with 810 nm Ti:sapphire laser [8]. Dependence of electron emission on laser power, polarization and DC voltage was investigated. They showed two emission processes: single-photon assisted DC field tunneling and strong optical field tunneling. They also demonstrated sub-cycle photo-electron emission in the strong optical field tunneling regime and theoretically showed sub-femtosecond electron pulses can be produced [9]. Ropers et al. studied multiphoton electron emission using low power femtosecond Ti:sapphire laser pulses to illuminate metal tips [10]. They primarily focused on the effects of DC bias voltage and incident laser power on electron emission and observed different power dependences under different DC bias voltages. In their theoretical model, the incident laser gave rise to a non-equilibrium electron distribution and electron tunneling through the work function barrier was caused by the DC bias voltage. Barwick *et al.* studied the electron emission mechanism by measuring the electron counts from a sharp tungsten tip illuminated by a near-infrared laser [11]. Electron emission was shown to depend on laser power, polarization and applied DC voltage. Yanagisawa *et al.* showed photoelectron emission from a single crystal tungsten tip and the selectivity of the emission sites [12]. The emission from different crystal surfaces was controlled by the polarization and incident angles of the laser pulses. Bormann *et al.* studied photoelectron emission from a gold tip operating in optical field emission regime [13]. The transition from multiphoton emission to optical field emission was observed by increasing the laser pulse energy. Schenk *et al.* demonstrated above-threshold photoemission with a photon order up to 9 from a sharp single crystal tungsten tip [14]. Peak suppression and threshold shifting observed from the electron energy spectra were indicative of the onset of strong field effects. Krüger *et al.* investigated attosecond electron emission from a tungsten tip and showed

carrier-envelope-phase (CEP) modulation of the energy spectra of emitted electrons [15]. The spectra were shown to be affected by the interference of sub-cycle emitted electron wave packets and electron re-scattering from the tip surface.

In addition to single-tip optical field emitter, optical field emitter arrays based on various materials and device architectures have also been reported, starting from the study of semiconductor optical field emitter arrays dating back to 1970s. Photo-assisted field emission from Si tip arrays was investigated by Thomas and Nathanson [16], Schroder *et al.* [17], Aboubacar *et al.* [18][19], Liu *et al.* [20], and Chiang *et al.* [21]. Hudanski *et al.* designed a carbon nanotube (CNT) based photocathodes by attaching CNTs to silicon p-i-n photodiodes [22]. In their design, photon-electron conversion and electron emission were separately performed by photodiodes and CNTs, respectively. In these studies on semiconductor optical field emitter arrays, the electron emission was induced by the applied electrostatic field and the photo-modulation was achieved by generating electron-hole pairs, and thus increasing the supply of electrons, which is very different from recently proposed multiphoton emission and optical field emission mechanisms. Zeier *et al.* reported optically enhanced electron emission from gold nano-pin-forest cathode [23]. The laser energy was coupled into and heated the pins, inducing thermionic or thermo-field emission. Mustonen *et al.* recently developed gated molybdenum (Mo) optical field emitter arrays fabricated by molding [24]. The electrostatic field together with a femtosecond laser pulse induces the emission of 5 pC electron bunch from the array.

Surface plasmon enhanced electron emission also gained researchers' attention recently as surface plasmon resonance can offer a high field enhancement factor and thus high electron emission yield. Irvine *et al.* showed electron emission and acceleration by surface plasmon polaritons on a thin film silver surface [25]. Electrons were generated via three-photon-assisted multiphoton emission and accelerated by surface plasmons, gaining kinetic energies up to 0.4 keV. Iwami *et al.* reported plasmon-assisted field emission from fused silica tip arrays coated with gold thin film [26]. Linear fitting of data in a Fowler-Nordheim plot indicated the emission mechanism was field emission. Nagel et al. studied photo-induced electron emission from lithographically defined, electrochemical deposited gold nanopillar arrays [27]. The effect of surface plasmons on electron emission and acceleration were revealed from the energy spectra of emitted electrons. Li *et al.*

patterned copper photocathode surface with nano-hole arrays [28]. The excitation of surface plasmon polaritons on the periodically structured metal surface enhanced optical power absorption and hence photoelectron emission yield. Polyakov *et al.* fabricated a metallic grating structure as the photocathode, of which the optical power absorption was enhanced by metamaterial plasmonic resonance [29]. Thus, the photoelectron emission was greatly enhanced and showed dependence on the polarization of incident light.

1.5 Summary of Work

The goal of this thesis is to develop optical field emitter arrays that meet required specifications, which cannot be satisfied simultaneously by previously proposed design, as the electron source for emittance-exchange ICS X-ray sources. Specifically, the primary focus is on ultrafast response, low emittance, and enough charge yield of the optical field emitter arrays. Femtosecond and even sub-femtosecond ultrafast response can be achieved via actuation of metallic emitters with femtosecond laser pulses. Low emittance will be achieved by using small emitters with tens of nanometers scale and thus reducing the emission area. Requirements on charge yield can be met by making high density arrays and utilizing surface plasmon resonance enhancement.

Chapter 2: Theory of Electron Emission and Surface Plasmon Resonance

2.1 Electron Emission Theory

Depending on the driving mechanisms, there are several different mechanisms of electron emission: thermionic emission, static field emission and photo-electron emission.

2.1.1 Thermionic Emission

Thermionic emission is electron emission induced by heating the emitting material, where electrons gain enough thermal energy to overcome the vacuum potential barrier and escape the material surface. For simplicity, we take metals as example emission materials. Electrons confined in a metal can be treated as a free electron gas and have an energy distribution described by the Fermi-Dirac distribution:

$$f(E) = \frac{1}{e^{(E-E_F)/k_B T} + 1} \tag{2.1}$$

Here E_F is the Fermi level of the system (metal), T is the temperature and k_B is the Boltzmann constant:

$$k_B = 1.381 \times 10^{-23}\ m^2 \cdot kg \cdot s^{-2} \cdot K^{-1} \tag{2.2}$$

The situation under consideration is illustrated in Fig. 2.1.

According to the Fermi-Dirac distribution, at non-zero temperature there exists a non-zero probability that some electrons have energies higher than the vacuum energy level so that they can overcome the barrier and leave the metal. The proportionality of high energy electrons increases with temperature. Experimentally, hot metals can emit electrons in this way. Hence, the process is called thermionic emission.

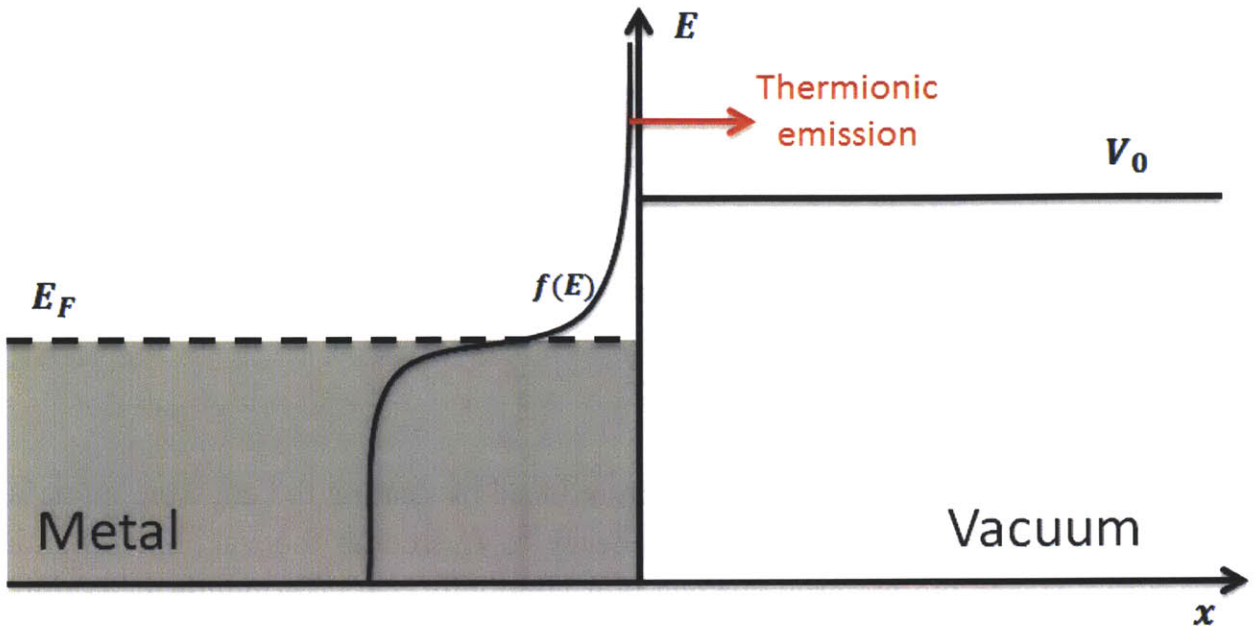

Fig. 2.1. Schematic for thermionic emission from metal to vacuum. The shaded region represents the free electron gas. E_F is the Fermi level and V_0 is the vacuum energy level. Electrons in a metal have a Fermi-Dirac distribution $f(E)$. At a finite temperature, some electrons have energy higher than the vacuum energy level and can be emitted into vacuum.

The thermionic current density in this model is

$$J = -g_s \int_{-\infty}^{\infty} \frac{dk_y}{2\pi} \int_{-\infty}^{\infty} \frac{dk_z}{2\pi} \int_{k_0}^{\infty} \frac{dk_x}{2\pi} e v_x(\boldsymbol{k}) \frac{1}{e^{(E(\boldsymbol{k})-E_F)/k_B T} + 1} \tag{2.3}$$

where g_s is the spin degeneracy and k_0 is the minimum value of k_x required for an electron to escape from the metal. For energies well above the Fermi level, the Fermi-Dirac distribution can be approximated by the Boltzmann distribution:

$$f(E) = e^{-(E-E_F)/k_B T} \tag{2.4}$$

And for a free electron gas,

$$E(\boldsymbol{k}) = \frac{\hbar^2 |\boldsymbol{k}|^2}{2m} \tag{2.5}$$

So the minimum x-directed momentum for an electron to escape is

$$k_0 = \sqrt{\frac{2mV_0}{\hbar^2}} \tag{2.6}$$

And velocity

$$v_x(\boldsymbol{k}) = \frac{\hbar k_x}{m} \tag{2.7}$$

Therefore, the integral in equation (2.3) can be readily evaluated as

$$J = -\frac{em}{2\pi^2\hbar^3}(k_B T)^2 e^{-(V_0 - E_F)/k_B T} \tag{2.8}$$

Note the work function of the metal is defined as

$$\Phi = V_0 - E_F \tag{2.9}$$

Equation (2.8) can be re-written as

$$J = A_0 T^2 e^{-\Phi/k_B T} \tag{2.10}$$

which is the well-known Richardson-Dushman equation, and A_0 is termed as the Richardson constant.

It can be easily seen that the thermionic current density increases drastically with increasing temperature of the emitter, and the Richardson constant is a material-dependent parameter determining which material is appropriate for thermionic emission applications. Thermionic electron emission guns are usually made of materials like W, LaB_6 and ZrO/W, because of their large Richardson constants and high melting temperature. Thermionic emitters are usually enhanced by the Schottky effect which will be discussed in the following section.

2.1.2 Static Field Emission

Static field emission refers to the phenomenon of electron emission from materials when an electrostatic field is applied. The emission mechanism can be explained by the quantum tunneling effect. Again, we consider a metal with the band diagram as shown in Fig. 2.2. In contrast to the situation shown in Fig. 2.1, the vacuum energy level in Fig. 2.2 is bent down from V_0 to $V_0 - eE_0x$ by the electrostatic field E_0 (note both energy and electric field were denoted with E; to avoid ambiguity, we use E_0 to represent the electric field in this section). The resultant vacuum energy barrier has a triangular shape and electrons can tunnel through this barrier, forming a static field emission current. In static field emission, electrons do not need to gain extra energy to overcome the work function barrier and emission can happen at temperature $T = 0K$. Therefore, static field emission is also termed as "cold" field emission.

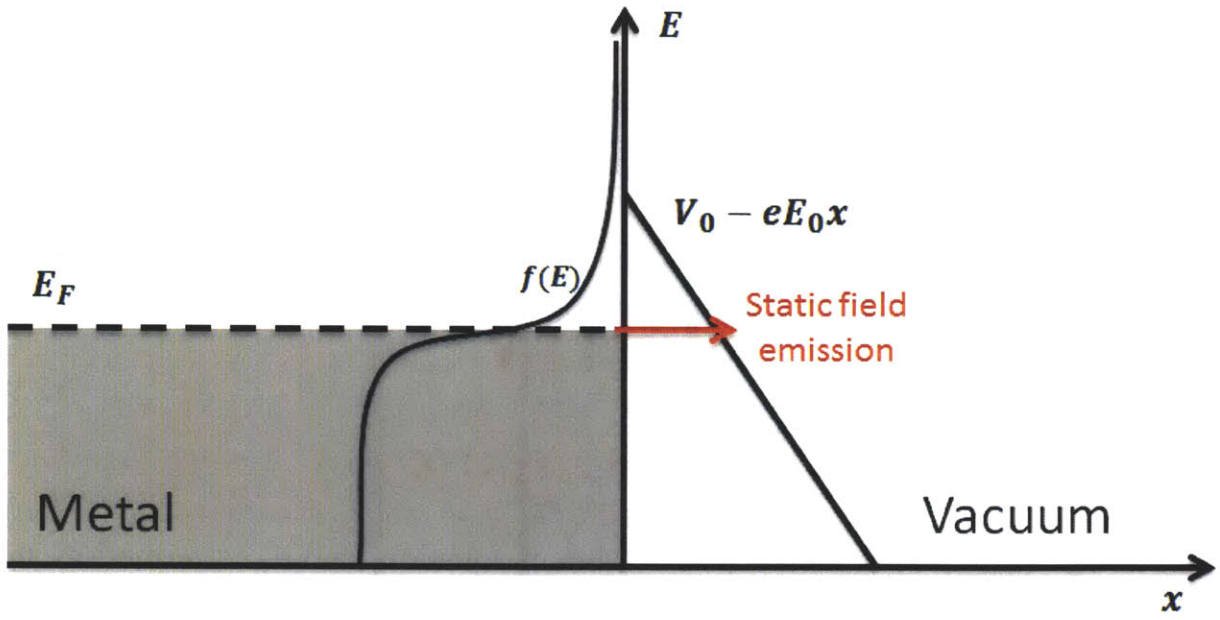

Fig. 2.2. Schematic for static field emission from metal to vacuum. The shaded region represents the free electron gas. E_F is the Fermi level and V_0 is the vacuum energy level. Electrons in a metal have a Fermi-Dirac distribution $f(E)$. The applied electrostatic field E_0 bends down the vacuum energy level from V_0 to $V_0 - eE_0x$. Hence, a triangular vacuum barrier is formed. Electrons can tunnel through this vacuum barrier and lead to static field emission.

We assume the temperature of the metal is 0 K, and according to Fermi-Dirac distribution, all states below the Fermi level are filled while all state above the Fermi level are empty. Within the WKB approximation, the tunneling probability is

$$T(E_x) = \exp[-2\int_{x_1}^{x_2}(\frac{2m}{\hbar^2})^{1/2}[V(x) - E_x]^{1/2}dx] \tag{2.11}$$

where the x-directed electron kinetic energy

$$E_x = \frac{\hbar^2 k_x^2}{2m} \tag{2.12}$$

For a triangular barrier, assuming the tunneling electrons are in the narrow range around the Fermi level, thus

$$T(E_x) \approx T_0 \exp[2(\frac{2m}{\hbar^2})^{1/2} \frac{\Phi^{1/2}(E_x - E_F)}{eE_0}] \tag{2.13}$$

with

$$T_0 = \exp[-\frac{4}{3}(\frac{2m}{\hbar^2})^{1/2} \frac{\Phi^{3/2}}{eE_0}] \tag{2.14}$$

The total tunneling current is

$$J = -g_s \int \frac{dk_y}{2\pi} \int \frac{dk_z}{2\pi} \int \frac{dk_x}{2\pi} \frac{e\hbar k_x}{m} T(E_x) f(E) \tag{2.15}$$

Considering the Fermi-Dirac distribution at 0 K, $f(E)$ can be suppressed and the integral is over a sphere with radius $k_F = \sqrt{\frac{2mE_F}{\hbar^2}}$ in k-space. Also, we neglect the negative sign as the direction of the emission current is always pointing into the material so we are only interested in its magnitude. Finally, we arrive at the Fowler-Nordheim equation which correlates the electron emission current density with the local electric field and the material work function:

$$J = \frac{e^3 E^2}{8\pi h \Phi} exp[-\frac{8\pi\sqrt{2m}\Phi^{3/2}}{3heE}] \tag{2.16}$$

where J is the electron emission current density, h is Planck's constant, m is the mass of the electron, Φ is the work function of the emission material, e is the charge of the electron and E is the local electric field at the emission region (since the energy of the electron is no longer explicitly shown, we switch back to E as the denotation of the electric field).

In reality, the vacuum potential barrier is not perfectly triangular. The local electric field can round the top of the triangular potential barrier and reduce the height of the barrier, known as the Schottky effect:

$$\Phi_{eff} = \Phi - e[eE/(4\pi\epsilon_0)]^{1/2} \tag{2.17}$$

where Φ_{eff} is the effective barrier height, Φ is the original barrier height, e is the charge of the electron and E is the local electric field at the emission region.

When applying a static field to thermionic electron guns, the Schottky effect can reduce the effective work function and hence increase the thermionic emission current. The resultant emitters are termed as thermal Schottky guns or thermal field

emission (TFE) guns, in contrast to cold field emission guns relying on pure field emission.

As with static field emission guns, the electrostatic field is always present. Moreover, the image force potential induced by the image charge can also modify the shape and height of vacuum potential barrier. All of these effects lead to a modified form of Fowler-Nordheim equation [30]:

$$J = \frac{e^3 E^2}{8\pi h \Phi t^2(w)} exp[-\frac{8\pi\sqrt{2m}\Phi^{3/2}}{3heE} v(w)] \tag{2.18}$$

where $v(w)$ is a slowly varying function taking into account the image force of the tunneling electron with $0.4 < v(w) < 0.8$, and the value of function $t(w)$ is approximately 1 with $w = e^{3/2}(E/4\pi\epsilon_0)^{1/2}/\Phi$.

2.1.3 Photoelectron Emission

Photoelectron emission is the electron emission induced by incident photons. The photo-electric effect, discovered by Einstein more than a hundred years ago, is the first demonstration of photo-electron emission. However, the complexity of the photo-electron emission physics is not fully revealed until recently [8-15].

Photo-electron emission can be further divided into optical field emission and single-/multi-photon emission, both illustrated in Fig. 2.3. Due to different operating regimes, optical field emission and single-/multi-photon emission are observed. For optical field emission, the electrons are ripped off from emitters by the electric field of the incident laser; or equivalently, the electrons tunnel through the emitter-vacuum potential barrier assisted by the electric field of the laser pulse. For single-/multi-photon emission, the electron absorbs one or more photons of the laser, hence gaining enough energy to overcome the work function barrier, followed by over-the-barrier emission. Whether the emitters are operating in the optical field emission regime or single-/multi-photon emission regime depends on the drive laser power. For low laser power, single-/multi-photon emission dominates, while for high laser power, optical field emission supercedes. The existence of a strong DC electric field comparable to the optical field also assists the transformation from single-/multi-photon regime to optical field regime [10]. The Keldysh parameter [31] provides a quantitative method to determine the operation regimes. The Keldysh parameter γ is calculated by

$$\gamma = \omega(2m\Phi)^{1/2}/eE \tag{2.19}$$

where ω is the angular frequency of the incident light, m is the mass of the electron, Φ is the work function of the emission material, e is the charge of the electron and E is the local electric field at the emission region. For $\gamma \gg 1$, single-/multi-photon emission makes the major contribution, while optical field emission dominates for $\gamma \ll 1$. For $\gamma \sim 1$, the photo-induced electron emission is in the transition regime between single-/multi-photon emission and optical field emission.

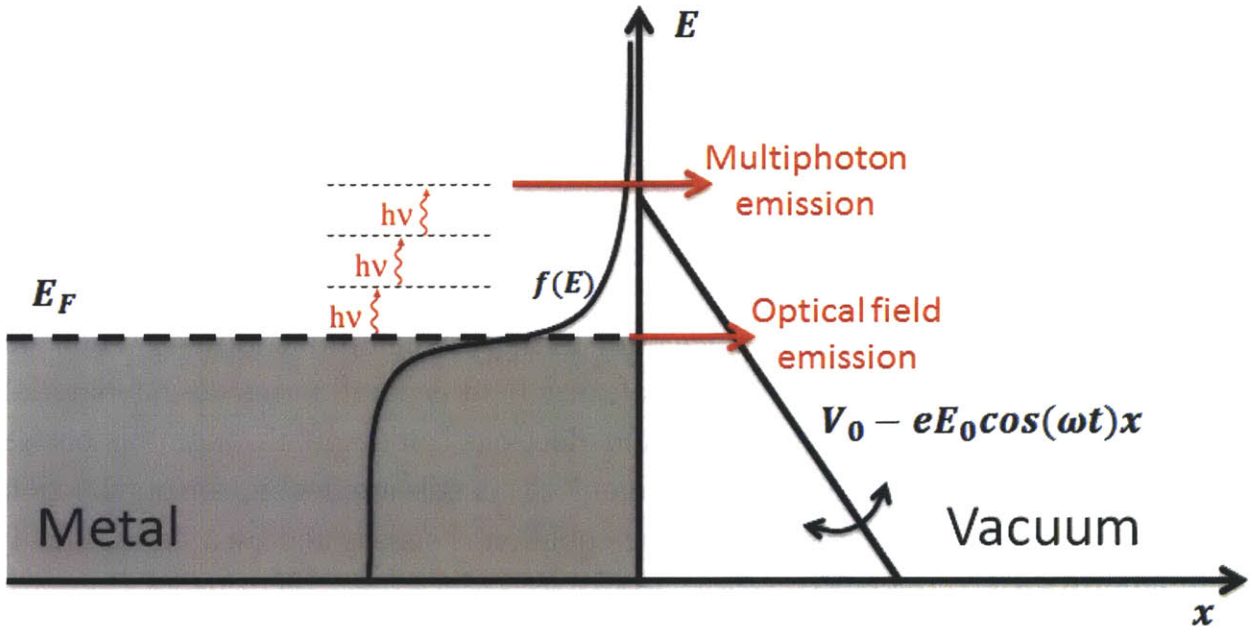

Fig. 2.3. Schematic for optical field emission and multiphoton emission from a metal to vacuum. The shaded region represents the free electron gas. E_F is the metal Fermi level and V_0 is the vacuum energy level. Electrons in a metal have a Fermi-Dirac distribution $f(E)$. The applied optical field $E_0\cos(\omega t)$ bends the vacuum energy level up and down from V_0 to $V_0 - eE_0\cos(\omega t)x$. For optical field emission, the electron tunnels through the vacuum barrier when the optical field bends down the vacuum energy level and thins the barrier. For multiphoton emission (three-photon emission in the figure), the electron absorbs multiple photons so that it gains enough energy to overcome the work function barrier.

For single-/multi-photon emission, since the electron needs to absorb n photons simultaneously to overcome the work function barrier, the electron emission current density is proportional to the n^{th} power of the incident laser intensity:

$$J \propto (I)^n \tag{2.20}$$

and hence proportional to the (2n)th power of the incident laser field:

$$J \propto (E)^{2n} \tag{2.21}$$

where n is the number of photons required for an electron to overcome the work function barrier:

$$n\hbar\omega \geq \Phi \tag{2.22}$$

The probability of photon absorption also depends on polarization and reaches a maximum when the incident electric field is polarized perpendicular to the surface [11]. Thus, equation (2.21) can be modified to

$$J \propto (E\cos\theta)^{2n} \tag{2.23}$$

where θ is the polarization angle of the incident light, with $\theta = 0$ indicating the electric field is polarized perpendicular to the emission surface.

For optical field emission, on the other hand, the electrons are emitted via quantum tunneling effect. The electric field of incident light can be treated as a harmonically oscillating field which bends the vacuum energy level up and down. When the vacuum level is bent down, namely the electric field is pointing inside the material, a triangular potential barrier is formed and electrons can tunnel through this barrier. Therefore, the Fowler-Nordheim equation (2.18) is still applicable for optical field emission, as long as the static field in the equation is substituted by a harmonically oscillating field.

The above discussions did not present a complete and accurate theoretical treatment of photo-electron emission. However, the physical picture is clear and the theory is enough to guide the design of optical field emitters and interpret experimental results qualitatively and quantitatively. The most important result is that increasing the local electric field (near-field) strength can greatly improve the photo-electron emission yield. This is explicit for optical field emission, where the emission current density can be calculated from the Fowler-Nordheim equation

$$J = AE^2\exp(-B/E) \tag{2.24}$$

where A and B are material dependent constants. The emission current density is dramatically increased with increasing near-field. This is also valid for single-/multi-photon emission. The probability for the material to absorb n photon is proportional to the n^{th} power of local intensity and hence the $(2n)^{th}$ power of local electric field

$$P_{abs} \propto (I)^n \propto (E)^{2n} \tag{2.25}$$

Thus, a strong near-field will result in increased absorption probability and hence increased single-/multi-photon emission yield. This indicates that the analysis of the non-linear process of photoelectron emission can be decoupled into two steps: first calculation of the near-field and then calculation of the photo-electron emission current or yield. Near-field calculations can be done by solving Maxwell's equations, as discussed in the next section, while electron emission can be analyzed with the theory discussed in this section.

2.2 Electromagnetics Theory

2.2.1 Maxwell's Equations

Electromagnetic problems can be solved via the Maxwell's equations:

$$\text{Faraday's Law } \nabla \times \boldsymbol{E} = -\frac{\partial \boldsymbol{B}}{\partial t} \text{ or } \oint_C \boldsymbol{E} \cdot d\boldsymbol{s} = -\iint_S \frac{\partial \boldsymbol{B}}{\partial t} \cdot d\boldsymbol{a} \tag{2.26}$$

$$\textit{Ampere's Law } \nabla \times \boldsymbol{H} = \frac{\partial \boldsymbol{D}}{\partial t} + \boldsymbol{J} \textit{ or } \oint_C \boldsymbol{H} \cdot d\boldsymbol{s} = \iint_S \left(\frac{\partial \boldsymbol{D}}{\partial t} + \boldsymbol{J}\right) \cdot d\boldsymbol{a} \tag{2.27}$$

$$\textit{Electric Gauss's Law } \nabla \cdot \boldsymbol{D} = \rho \textit{ or } \oiint_S \boldsymbol{D} \cdot d\boldsymbol{a} = \iiint_V \rho dV \tag{2.28}$$

$$\textit{Magnetic Gauss's Law } \nabla \cdot \boldsymbol{B} = 0 \textit{ or } \oiint_S \boldsymbol{B} \cdot d\boldsymbol{a} = 0 \tag{2.29}$$

Here, both the differential and integral forms of the equations are shown.

We are particularly interested in the situation in which the fields vary time-harmonically, namely, at a single frequency. This is because in the frequency domain, the time derivatives can be replaced by simple multiplication. Also, according to Fourier's theorem, an arbitrary electromagnetic wave can be represented as the superposition of time-harmonic waves with different frequencies. Moreover, the material properties usually have a frequency dependence, while their time-dependent response is usually less clear. Solving Maxwell's equations in frequency domain is a more natural and accurate approach.

In frequency domain, phasor notation is introduced for electromagnetic fields. For example,

$$\boldsymbol{E}(\boldsymbol{r},t) = Re[\boldsymbol{E}(\boldsymbol{r})e^{j\omega t}] \tag{2.30}$$

where the complex vector $\boldsymbol{E}(\boldsymbol{r})$ is the phasor of time-dependent electric field $\boldsymbol{E}(\boldsymbol{r},t)$. Hence, Maxwell's equations become complex in frequency domain:

$$\nabla \times \boldsymbol{E} = -j\omega\boldsymbol{B} \tag{2.31}$$
$$\nabla \times \boldsymbol{H} = j\omega\boldsymbol{D} + \boldsymbol{J} \tag{2.32}$$
$$\nabla \cdot \boldsymbol{D} = \rho \tag{2.33}$$
$$\nabla \cdot \boldsymbol{B} = 0 \tag{2.34}$$

2.2.2 Wave Equation

Combining Faraday's and Ampere's laws, the following equation can be derived:

$$\nabla \times \nabla \times \boldsymbol{E} + \mu\epsilon\frac{\partial^2}{\partial t^2}\boldsymbol{E} = 0 \tag{2.35}$$

And for piecewise homogeneous media, equation (2.35) can be reduced to

$$\nabla^2\boldsymbol{E} - \mu\epsilon\frac{\partial^2}{\partial t^2}\boldsymbol{E} = 0 \tag{2.36}$$

Equations (2.35) and (2.36) can also be written in the frequency domain:

$$\nabla \times \nabla \times \boldsymbol{E} - \omega^2\mu\epsilon\boldsymbol{E} = 0 \tag{2.37}$$
$$\nabla^2\boldsymbol{E} + \omega^2\mu\epsilon\boldsymbol{E} = 0 \tag{2.38}$$

Equations (2.35), (2.36), (2.37) and (2.38) are all widely used forms of the wave equation, which describes the propagation of electromagnetic waves. Take equation (2.38) and assume a frequency-dependent wave vector $k(\omega)$, the following equation can be derived

$$k(\omega)^2 = \omega^2\mu\epsilon \tag{2.39}$$

This equation characterizes the dispersion relation of the medium in which the electromagnetic wave is propagating.

2.2.3 Boundary Conditions

Electric and magnetic fields at a boundary between two media have to satisfy certain boundary conditions. By applying the four Maxwell's equations to an infinitesimal region across the boundary, the following four boundary conditions can be obtained:

$$\boldsymbol{n} \times (\boldsymbol{E}_1 - \boldsymbol{E}_2) = 0 \tag{2.40}$$
$$\boldsymbol{n} \times (\boldsymbol{H}_1 - \boldsymbol{H}_2) = \boldsymbol{J}_s \tag{2.41}$$

$$\boldsymbol{n} \cdot (\boldsymbol{D}_1 - \boldsymbol{D}_2) = \rho_s \quad (2.42)$$

$$\boldsymbol{n} \cdot (\boldsymbol{B}_1 - \boldsymbol{B}_2) = 0 \quad (2.43)$$

where $\boldsymbol{J_s}$ is the surface current density, ρ_s is the surface charge density, and subscripts 1 and 2 indicate field components in medium 1 and medium 2, respectively. In other words, the boundary conditions require: (i) tangential electric field $\boldsymbol{E}$ is continuous across the boundary; (ii) tangential magnetic field strength $\boldsymbol{H}$ changes values at a boundary in accordance with the surface current density; (iii) normal electric displacement field $\boldsymbol{D}$ changes values at a boundary in accordance with the surface charge density; and (iv) normal magnetic field $\boldsymbol{B}$ is continuous across the boundary.

It is interesting to look at equation (2.42), the boundary condition resulting from electric Gauss's law. For a perfect conductor, the fields within the conductor are zero. Hence,

$$n \cdot \boldsymbol{D}_1 = \rho_s \quad (2.44)$$

In other words, the surface charge density is the normal electric displacement field. If we define surface (electric) field as the (electric) field normal to the interface between a prefect conductor and a dielectric, then the surface charge density is proportional to the surface field. For non-perfect conductors, such as gold in optical frequency, this proportionality relation still holds as a reasonably good approximation. This relation between surface charge density and surface field for conductors is very important. In numerical simulations, the charge distribution can be difficult to determine as its calculation involves taking derivatives of the fields and huge numerical artifacts caused by discontinuous values of the fields can emerge. In this situation, the calculation of surface fields provides an easier way to investigate the charge distribution.

2.2.4 Constitutive Relations and Material Properties

Constitutive relations are

$$\boldsymbol{D} = \epsilon \boldsymbol{E} \quad (2.45)$$

$$\boldsymbol{B} = \mu \boldsymbol{H} \quad (2.46)$$

Permittivity ϵ and permeability μ reflect the electromagnetic properties of materials. The ratio of the material permittivity (permeability) to vacuum permittivity (permeability) is called relative permittivity (permeability). Since the

vacuum permittivity and permeability are physical constants, ϵ and μ are sometimes used as notations for relative permittivity and permeability without ambiguity.

At optical frequency, the permeability is usually the same as its value in vacuum except for some engineered metamaterials. However, the permittivity is quite different from its value in vacuum and determines materials' response to optical waves.

2.2.5 Quasi-Static Approximation

One consequence of the Maxwell's equations is that changes of charges and currents in time are not synchronized with changes of electromagnetic fields, which are often delayed due to the finite speed of electromagnetic wave propagation. This is called the retardation effect, which usually complicates the analysis of problems. Also, solving Maxwell's equations usually requires intensive computation efforts. In certain kinds of problems, approximations can be made to simplify the equations. One of the most frequently encountered situations is electrostatics (magnetostatics), where the electric (magnetic) field is static or oscillating at a very low frequency. Hence, the electromagnetic wavelength is so large that the phase shift or phase gradient is caused only by inductive or capacitive material properties rather than by wave propagation delays. Therefore, quasi-static approximation can be applied, where the retardation effect and phase shift due to wave propagation can be safely neglected. As a result, for electrostatic problems only the electric Gauss' law needs to be considered and Maxwell's equations are reduced to

$$\nabla \cdot (\epsilon \boldsymbol{E}) = \rho \tag{2.47}$$

where ρ is the charge density and $\boldsymbol{E}$ is the electric field, satisfying

$$\boldsymbol{E} = -\nabla \phi \tag{2.48}$$

where ϕ is the electrostatic potential. If the medium is piece-wise homogeneous, the above equation can be further rewritten as the famous Poisson equation:

$$\nabla^2 \phi = -\rho/\epsilon \tag{2.49}$$

and it yields the Laplace equation in a charge-free region of space:

$$\nabla^2 \phi = 0 \tag{2.50}$$

Before applying the quasi-static approximation, its validity should be carefully reviewed. In general, it is valid if the electromagnetic wavelength is ten times larger than the spatial dimension of the problem. The longer the wavelength, the higher accuracy the approximation possesses. The interaction between light and subwavelength structures can usually be analyzed with the quasi-static approximation. For the extreme situation where the electric field does not change with respect to time, the approximation becomes the exact representation.

2.2.6 Nano Optics

Nano optics refers to the study of interactions between light and nanoscale objects. It has been under heated investigation recently thanks to the development of nanofabrication methods, numerical computation power and optical techniques.

According to the Heisenberg uncertainty principle,

$$\Delta(\hbar k)\Delta x \geq \frac{\hbar}{2} \tag{2.51}$$

where Δx and Δk are the spatial and momentum spread of a photon, respectively. The maximum momentum spread is the free space wavevector [32]

$$k = 2\pi/\lambda \tag{2.52}$$

Thus, the maximum spatial spread is

$$\Delta x \geq \frac{\lambda}{4\pi} \tag{2.53}$$

This is one form of the well-known diffraction limit of light, telling that the spatial confinement of optical energy (e.g. light focused by a lens) cannot be smaller than a certain fraction of its wavelength. However, this limit can be broken by near-field light, of which the wavevector can be decomposed into a transverse component and a propagating component:

$$k = \sqrt{k_{\perp}^2 + k_{\parallel}^2} \tag{2.54}$$

For light interacting with subwavelength structures with a dimension much smaller than wavelength and hence below the diffraction limit, the transverse wavevector is larger than the free space wavevector:

$$k_{\perp} > k \tag{2.55}$$

Combining (2.54) and (2.55), the propagating wavevector can only be imaginary:

$$k_{\parallel} = i\alpha \tag{2.56}$$

Therefore, the light cannot propagate away from the subwavelength structure, hence the name "near-field".

Light has a wavelength ranging from several hundred nanometers to a few micrometers while nanostructures usually have a sub-100 nm dimension. As a result, the interactions between light and nanoscale objects, or nano optics, are essentially the interactions between subwavelength structures and near-field.

2.3 Surface Plasmon Resonance

Surface plasmon resonance (SPR) is the collective oscillation of electrons in a solid stimulated by incident light. The resonance condition is established when the frequency of light photons matches the natural frequency of surface electrons oscillating against the restoring force of positive nuclei. The study of surface plasmons, *plasmonics*, is an important sub-area of nano optics as it usually involves the evanescent field (near-field) or light interacting with subwavelength nanostructures, and one important feature of surface plasmon resonance is its capability of confining electromagnetic energy to subwavelength dimensions.

Plasmonics contains two main components, surface plasmon polariton (SPP), originating from the work of Sommerfeld [33] and Zenneck [34] on surface waves propagating along the surface of a finite conductor, and localized surface plasmon resonance (LSPR), originating from the work of Mie [43] on light scattering by metallic particles.

2.3.1 Electromagnetic Properties of Metals

Most of the materials exhibiting SPR are metals, so it is important to first understand the electromagnetic properties of metals.

We start by considering a homogeneous free electron gas responding to a harmonically oscillating electric field $\boldsymbol{E} = \boldsymbol{E}_0 e^{j\omega t}$ [32]:

$$m\frac{\partial^2 \boldsymbol{r}}{\partial t^2} = -e\boldsymbol{E}_0 e^{j\omega t} \tag{2.57}$$

where m is the mass of electron, e is the charge (absolute value) of an electron and $\boldsymbol{r}$ is the position of the electron.

The solution of equation (2.57) gives

$$\boldsymbol{r} = \frac{e}{m\omega^2}\boldsymbol{E} \tag{2.58}$$

Moreover, the macroscopic polarization caused by the displacement of free electron gas is

$$\boldsymbol{P} = -ne\boldsymbol{r} \tag{2.59}$$

where n is the number of electrons per unit volume. Thus,

$$\boldsymbol{P} = -\frac{ne^2}{m\omega^2}\boldsymbol{E} \tag{2.60}$$

Recall that polarization can be expressed as

$$\boldsymbol{P} = \epsilon_0\chi(\omega)\boldsymbol{E} \tag{2.61}$$

where $\chi(\omega)$ is the frequency-dependent electric susceptibility relating to (relative) permittivity or dielectric function ϵ by

$$\epsilon(\omega) = 1 + \chi(\omega) \tag{2.62}$$

Combining equations (2.60), (2.61) and (2.62), the permittivity of free electron gas is

$$\epsilon(\omega) = 1 - \frac{\omega_P^2}{\omega^2} \tag{2.63}$$

where ω_P is the free electron gas plasma frequency defined as

$$\omega_P = \sqrt{\frac{ne^2}{m\epsilon_0}} \tag{2.64}$$

By using the Drude model, which treats the metal as a free electron gas, equation (2.63) is thus the frequency-dependent permittivity of the metal.

It is interesting to further discuss equation (2.63) as the metal permittivity. At frequency below the plasmon frequency ($\omega < \omega_P$), the metal permittivity is negative ($\epsilon(\omega) < 0$). According to the dispersion relation given by equation (2.39), the wave number is purely imaginary, namely, electromagnetic wave cannot propagate within the metal. This is the exact reason that metals can be treated as

perfect conductors and are usually used as the materials for mirrors and waveguides at low frequencies. On the other hand, at frequencies above the plasmon frequency ($\omega > \omega_P$), the wave number is positive and the metal becomes transparent for high frequency electromagnetic waves.

When an electron is oscillating in a metallic solid, scattering by ion cores can cause damping of the oscillation. We can also include the damping effect into the Drude model and modify equation (2.57) as

$$m\frac{\partial^2 \boldsymbol{r}}{\partial t^2} + m\Gamma\frac{\partial \boldsymbol{r}}{\partial t} = -e\boldsymbol{E}_0 e^{j\omega t} \tag{2.65}$$

where the second term on the L.H.S. characterizes the damping effect. With the same approach, metal permittivity can be written as

$$\epsilon(\omega) = 1 - \frac{\omega_P^2}{\omega^2 + i\Gamma\omega} \tag{2.66}$$

Now the permittivity possesses an imaginary part which corresponds to the damping or absorption effect of electromagnetic waves.

The Drude model is reasonably accurate as long as the metal can be approximated as a free electron gas. However, at high frequencies, interband transitions arise and the Drude model permittivity deviates from experimental data. In this situation, the more accurate Drude-Lorentzian model should be used:

$$m\frac{\partial^2 \boldsymbol{r}}{\partial t^2} + m\Gamma\frac{\partial \boldsymbol{r}}{\partial t} + m\omega_0^2\boldsymbol{r} = -e\boldsymbol{E}_0 e^{j\omega t} \tag{2.67}$$

The third term, a harmonic oscillating term, is added on the L.H.S. This is because interband transitions involve valence electrons which are bound to the ion cores so that they can be modeled by a Lorentzian oscillator, oscillating with respect to the cores. The permittivity is thus

$$\epsilon(\omega) = 1 - \frac{\omega_P^2}{\omega^2 - \omega_0^2 + i\Gamma\omega} \tag{2.68}$$

In fact, the (Drude-)Lorentzian model is a more generalized model compared to the free electron Drude model, and it can also be used to model the permittivity of dielectric materials and not merely metals.

2.3.2 Surface Plasmon Polariton (SPP)

SPP refers to a quasiparticle consists of the surface charge oscillation coupled to the electromagnetic excitation (the name "polariton" indicates the coupling effect). It is a wave existing at the interface between two materials where the real part of the permittivity changes sign across the interface. The SPP wave propagates along the interface and decays in the direction norm to the interface. Hence, it can be treated as an evanescent wave bound to an interface.

We first analyze the surface plasmon wave confined at a metal/dielectric surface. The schematic and coordinate system is shown in the inset of Fig. 2.4(a). The surface plasmon wave is confined at the metal/dielectric interface ($z = 0$) and propagates in $+\hat{x}$ direction. For the free electron Drude model, neglecting damping, the metal permittivity can be represented as a function of frequency:

$$\epsilon_1(\omega) = 1 - \omega_P^2/\omega^2 \tag{2.69}$$

where ω_P is the plasmon frequency. For dielectrics, we assume permittivity, ϵ_2, as a constant, which is usually valid for a wide spectral range. By solving the wave equation, we find that only the TM mode exists at the interface, and expressions for the fields are:

For $z < 0$

$$H_y = A_1 e^{-j\beta x} e^{k_1 z}, \tag{2.70}$$

$$E_x = jA_1 (k_1/\omega\epsilon_0\epsilon_1) e^{-j\beta x} e^{k_1 z}, \tag{2.71}$$

$$E_z = -A_1(\beta/\omega\epsilon_0\epsilon_1) e^{-j\beta x} e^{k_1 z}; \tag{2.72}$$

For $z > 0$

$$H_y = A_2 e^{-j\beta x} e^{-k_2 z}, \tag{2.73}$$

$$E_x = -jA_2 (k_2/\omega\epsilon_0\epsilon_2) e^{-j\beta x} e^{-k_2 z}, \tag{2.74}$$

$$E_z = -A_2(\beta/\omega\epsilon_0\epsilon_2) e^{-j\beta x} e^{-k_2 z}. \tag{2.75}$$

where A_1 and A_2 are amplitude coefficients, β is the propagation constant, and $k_1^2 = \beta^2 - k_0^2\epsilon_1$, $k_2^2 = \beta^2 - k_0^2\epsilon_2$, $k_0 = \omega\sqrt{\mu_0\epsilon_0}$.

Boundary conditions that tangential electric and magnetic fields are continuous at $z = 0$ require that

$$\frac{k_2}{k_1} = -\frac{\epsilon_2}{\epsilon_1} \tag{2.76}$$

For the SPP wave confined at the interface, the field amplitudes should decay in the direction normal to the interface, namely, both k_1 and k_2 should be positive. Therefore, it is clear that SPP can only exist at the boundary between two materials with dielectric permittivities of opposite signs.

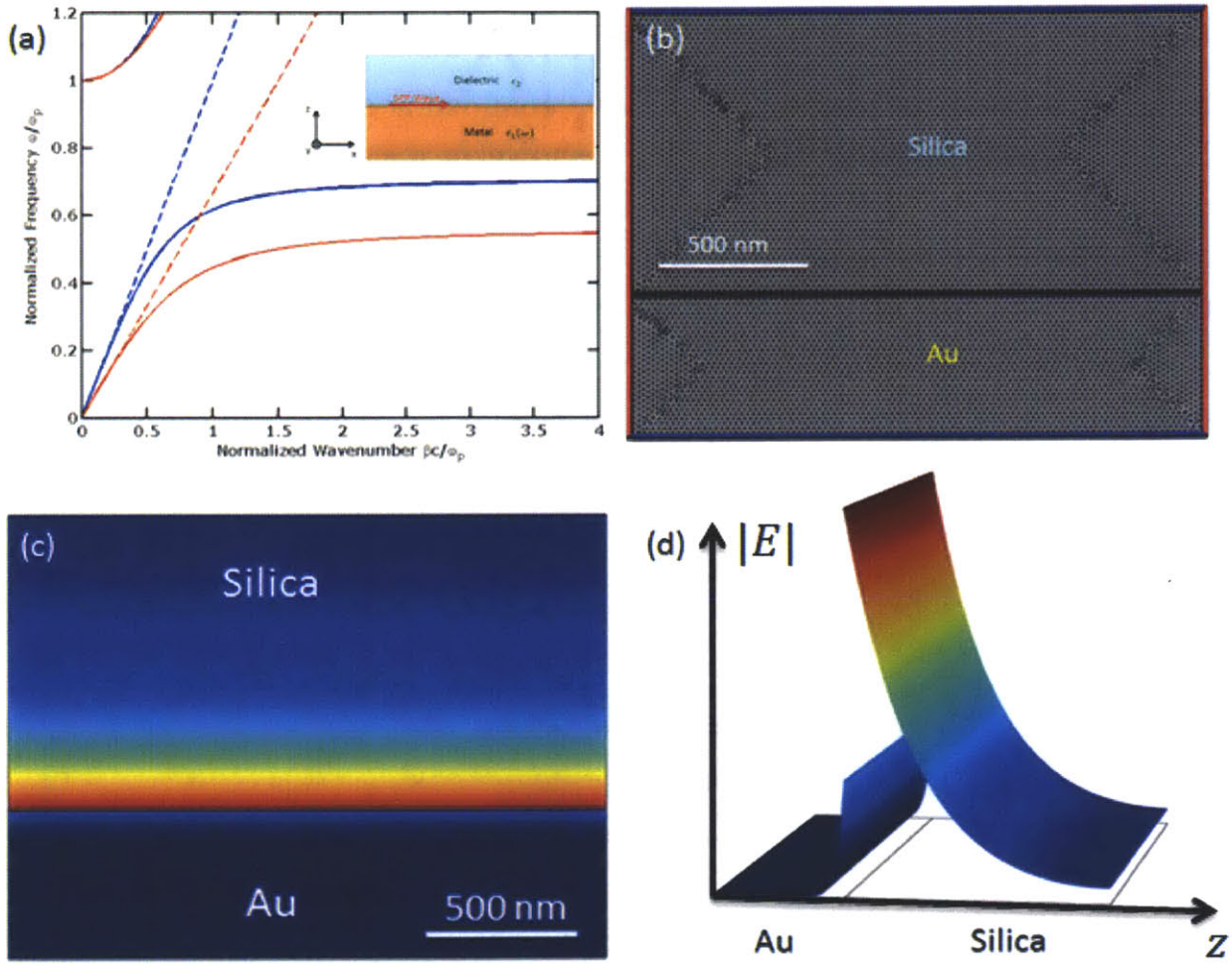

Fig. 2.4. Surface plasmon polariton wave confined at a metal/dielectric interface. (a) Solid curves: dispersion relation of surface plasmon wave. Dashed lines: dispersion relation of light in the dielectrics. Blue curves use air as the dielectric, while red curves use silica as the dielectric. Inset: schematic and coordinate system. (b) Model schematic and finite element meshing in COMSOL. (c) Electric field intensity of the surface plasmon polariton mode at Au/silica interface. (d) The same as (c), but uses height to represent the electric field intensity and better displays the exponential decay.

It can be seen that all field components are exponentially decaying away from the metal/dielectric interface ($z = 0$). Thus, the surface plasmon polariton wave is an

evanescent wave confined at the interface. The field intensity decay lengths are $L_1 = 1/k_1 = \sqrt{\epsilon_1 + \epsilon_2}/k_0|\epsilon_1|$, and $L_2 = 1/k_2 = \sqrt{\epsilon_1 + \epsilon_2}/k_0|\epsilon_2|$ for metal and dielectric, respectively.

By matching the boundary conditions across the interface, we arrive at the dispersion relation of the surface plasmon polariton wave:

$$\beta = k_0\sqrt{(\epsilon_1\epsilon_2)/(\epsilon_1 + \epsilon_2)} \tag{2.77}$$

The dispersion relations (normalized frequency vs. normalized propagation constant) for surface plasmon polariton waves at metal/air and metal/silica interfaces are plotted in Fig. 2.4(a) in blue solid curves and red solid curves. The dashed lines show the light dispersion in the dielectrics (air and silica). It can be seen the propagation constant of the surface plasmon polariton wave is smaller than the wavenumber in the dielectric. As a result, the wave cannot propagate into the dielectric. Moreover, for electromagnetic waves with frequency below the plasmon frequency, metal permittivity is negative and wave propagation in metal is forbidden. Therefore, the wave can only be confined at the interface and propagate along the interface as an evanescent wave. Hence, a single metal/dielectric interface can perform the function of confining surface plasmon polariton waves and act as a plasmonic "slab waveguide".

We also numerically simulated the plasmonic slab waveguide with the 2D mode solver in *COMSOL Multiphysics*. We chose the interface between Au and silica, the optical wavelength is 800 nm, and the model schematic and finite element meshing are illustrated in Fig. 2.4(b). The boundary conditions are also indicated, with perfect electric conductor shown as blue boundaries (top and bottom) and perfect magnetic conductor shown as red boundaries (left and right). These conditions match with the boundary fields of the TM mode. The fundamental mode is the surface plasmon polariton mode and its electric field distribution is shown in Figs. 2.4(c) and 2.4(d). The effective index calculated from the closed-form theoretical dispersion relation is 1.5758, and the effective index given by the numerical simulation is 1.5756, corresponding to a 0.01% relative numerical error. Moreover, the theoretical decay lengths are 25 nm and 264 nm in Au and silica, which can be verified by the field distribution calculated numerically (Fig. 2.4(c)). As for electromagnetic energy confinement, the decay lengths are only half of these values. All these results indicate perfect agreement between theoretical and

numerical analysis and demonstrate subwavelength confinement and guiding of SPP waves.

The most common ways of exciting SPP optically are prism coupling (Kretschmann & Otto configuration) and grating coupling. The central idea is to compensate the momentum mismatch between SPP and optical wave. Specifically, for a grating coupler, the following equation has to be satisfied in order to excite SPP:

$$\beta = k_0 \sin\theta \pm \frac{2\pi n}{P}, n = 1, 2, ... \tag{2.78}$$

where β is the SPP momentum, k_0 is the optical wave momentum in free space, θ is the incident angle and P is the grating pitch. The momentum kick provided by the grating satisfies the phase matching condition and excites SPP.

2.3.3 Localized Surface Plasmon Resonance (LSPR)

LSPR is associated with the non-propagating charge oscillation of a metallic particle excited by electromagnetic oscillation. The quantum of the oscillation is called a plasmon. LSPR can be interpreted as the oscillation of the electron gas with respect to the background ions and core electrons under the external electromagnetic field. Displacement of the electron gas creates local polarizations upon the metallic particle. Geometry of the particle determines the discrete LSPR modes that can be supported.

For a particle of size much smaller than the electromagnetic wavelength, quasi-static approximation discussed in section 2.2.5 can be used to analyze it. We first consider a spherical particle of radius R in a homogeneous medium. The dielectric permittivity of the particle is $\epsilon_1(\omega)$ with explicit frequency dependence, and the dielectric permittivity of the medium is ϵ_2 with no frequency dependence as is the case for most dielectrics in a wide range of optical frequency. With the quasi-static approximation, a uniform static electric field $\boldsymbol{E} = E_0\hat{\boldsymbol{z}}$ is applied. Solving the Laplace equation (2.50) in a spherical coordinate, the electric potential is [35] [36]

$$\Phi(r, \theta) = \sum_{l=0}^{\infty} \left[A_l r^l + B_l r^{-(l+1)}\right] P_l(cos\theta) \tag{2.79}$$

where P_l is the l-th order Legendre polynomial. Since the potential has to be finite at the origin, the solutions for the electric potentials inside and outside the particle are

$$\Phi_{in}(r,\theta) = \sum_{l=0}^{\infty} A_l r^l P_l(cos\theta) \tag{2.80}$$

$$\Phi_{out}(r,\theta) = \sum_{l=0}^{\infty} \left[B_l r^l + C_l r^{-(l+1)}\right] P_l(cos\theta) \tag{2.81}$$

The boundary conditions for this problem are

$$-\frac{1}{R}\frac{\partial \Phi_{in}}{\partial \theta}|_{r=a} = -\frac{1}{R}\frac{\partial \Phi_{out}}{\partial \theta}|_{r=a} \tag{2.82}$$

$$-\epsilon_1 \frac{\partial \Phi_{in}}{\partial r}|_{r=a} = -\epsilon_2 \frac{\partial \Phi_{out}}{\partial r}|_{r=a} \tag{2.83}$$

Applying these boundary conditions to equations (2.80) and (2.81), the final solutions can be retrieved

$$\Phi_{in}(r,\theta) = -\frac{3\epsilon_2}{\epsilon_1 + 2\epsilon_2} E_0 r cos\theta \tag{2.84}$$

$$\Phi_{out}(r,\theta) = -E_0 r cos\theta + \frac{\epsilon_1 - \epsilon_2}{\epsilon_1 + 2\epsilon_2} E_0 R^3 \frac{cos\theta}{r^2} \tag{2.85}$$

The electric potential outside the particle Φ_{out} can be rewritten by introducing the dipole moment $\boldsymbol{p}$

$$\Phi_{out} = -E_0 r cos\theta + \frac{\boldsymbol{p}\cdot\boldsymbol{r}}{4\pi\epsilon_0\epsilon_2 r^3} \tag{2.86}$$

$$\boldsymbol{p} = 4\pi\epsilon_0\epsilon_2 R^3 \frac{\epsilon_1 - \epsilon_2}{\epsilon_1 + 2\epsilon_2}\boldsymbol{E} \tag{2.87}$$

We further introduce the polarizability

$$\boldsymbol{\alpha} = \frac{\boldsymbol{p}}{\epsilon_0\epsilon_2\boldsymbol{E}} = 4\pi R^3 \frac{\epsilon_1 - \epsilon_2}{\epsilon_1 + 2\epsilon_2} \tag{2.88}$$

It is clear the polarizability shows resonance when

$$\epsilon_1(\omega) = -2\epsilon_2 \tag{2.89}$$

which is called the Fröhlich condition. The resonant mode associated with this condition is the dipole LSPR model of the particle. Obviously, the resonance is frequency dependent.

The electric field can be evaluated from previous solutions of the electric potential

$$\boldsymbol{E}_{in} = \frac{3\epsilon_2}{\epsilon_1 + 2\epsilon_2}\boldsymbol{E} \tag{2.90}$$

$$\boldsymbol{E}_{out} = \boldsymbol{E} + \frac{3\boldsymbol{n}(\boldsymbol{n}\cdot\boldsymbol{p}) - \boldsymbol{p}}{4\pi\epsilon_0\epsilon_2}\frac{1}{r^3} \tag{2.91}$$

Therefore, the resonance of polarizability suggests resonant enhancement of the electric fields.

The time varying fields can be treated simply by including a harmonic oscillating factor $\cos(\omega t)$. The accompanying magnetic fields can be calculated from the oscillating electric fields. In the viewpoint of optics, it is more practical to characterize the particle with its absorption and scattering cross sections, which are calculated from the Poynting vector determined by the electric and magnetic fields [37]

$$C_{abs} = kIm[\alpha] = 4\pi kR^3 Im[\frac{\epsilon_1 - \epsilon_2}{\epsilon_1 + 2\epsilon_2}] \tag{2.92}$$

$$C_{sca} = \frac{k^4}{6\pi}|\alpha|^2 = \frac{8\pi}{3}k^4R^6\left|\frac{\epsilon_1 - \epsilon_2}{\epsilon_1 + 2\epsilon_2}\right|^2 \tag{2.93}$$

and the extinction cross section is the sum of the two

$$C_{ext} = C_{abs} + C_{sca} \tag{2.94}$$

For a sphere with volume V under the Fröhlich condition, the extinction cross section is [38]

$$C_{ext} = 9\frac{\omega}{c}\epsilon_2^{3/2}V\frac{\epsilon_i}{[\epsilon_r + 2\epsilon_2]^2 + \epsilon_i^2} \tag{2.95}$$

where $\epsilon_1 = \epsilon_r + i\epsilon_i$.

For an ellipsoidal particle specified by $\frac{x^2}{R_1^2} + \frac{y^2}{R_2^2} + \frac{z^2}{R_3^2} = 1$, analytical treatment under quasi-static approximation is still applicable [37]. The polarizability

$$\alpha_i = 4\pi R_1R_2R_3\frac{\epsilon_1 - \epsilon_2}{3\epsilon_2 + 3L_i(\epsilon_1 - \epsilon_2)} \tag{2.96}$$

where $i = x, y, z$ and L_i is a geometrical factor

$$L_i = \frac{R_1R_2R_3}{2}\int_0^\infty \frac{dq}{(R_i^2 + q)f(q)} \tag{2.97}$$

where $f(q) = \sqrt{(q + R_1^2)(q + R_2^2)(q + R_3^2)}$.

For spheroids where two of the three axes are equal, equation (2.96) reveals that a spheroidal particle exhibit two resonances. For nanorods which will be discussed in Chapter 4 in details, it can be inferred even in the absence of analytical treatment that there are two LSPR peaks corresponding to transverse mode and longitudinal mode. This is also confirmed in literature [39-42].

It should be noted that under the quasi-static approximation, the particle acts like an electric dipole. Thus the resonant mode is the dipole LSPR mode. This retreatment is valid for small nanoparticles. However, for particles with larger dimensions, the phase change and retardation effect have to be taken into account. As a result, higher order LSPR modes will emerge. A full, rigorous electrodynamic treatment of the LSPR of nanoparticles was developed by Mie [43] and known as Mie theory. We will rely on numerical simulations in this thesis to perform full electrodynamic calculations to investigate LSPR on nanoparticles with various shapes and dimensions beyond analytical treatments (quasi-static approximation and Mie theory).

2.4 Electromagnetic Heating and Heat Transfer

When an electromagnetically lossy material is illuminated by a laser, heat will be deposited into the material caused by electromagnetic heating, where materials absorb electromagnetic energy and transform it into heat. This effect is favorable in some applications where the laser is used to modify (e.g. heat, cut, reshape, etc.) the material. However, for laser-driven optical field emitters, electromagnetic heating can damage the emitter structure and degrade device performance. Therefore, it is important to study the electromagnetic heating and heat transfer in the optical field emitters ensure that the device operates below the damage threshold in the experiment.

The heat transfer in rigid solid materials can be modeled by

$$\rho C_P \frac{\partial T}{\partial t} - \nabla \cdot (k \nabla T) = Q \tag{2.98}$$

where ρ is the density, C_P is the heat capacity, k is the thermal conductivity, Q is the heat source (or sink), and T is the temperature. For electromagnetic heating, the heat source Q equals approximately the amount of electromagnetic energy absorbed by the material.

Equation (2.98) characterizes the conduction of electromagnetically generated heat in solid materials. Another path of heat dissipation besides conduction is radiation, where the excess energy of heated materials is carried away by emitted photons. The heat radiation from a solid material can be modeled by surface-to-ambient radiation described by the following equation:

$$-\boldsymbol{n} \cdot (-k\nabla T) = \epsilon\sigma(T_{amb}^4 - T^4) \tag{2.99}$$

where $\boldsymbol{n}$ is the normal unit vector of the surface, T is the surface temperature, k is the thermal conductivity, ϵ is the material-dependent surface emissivity, σ is the Stefan-Boltzmann constant and T_{amb} is the ambient temperature.

2.4.1 Absorption Cross Section and Temperature Rise

For an object, the absorption of incident electromagnetic power can be characterized by the absorption cross section

$$P_{abs} = I\sigma_{abs} \tag{2.100}$$

where σ_{abs} is the absorption cross section, I is the power flow (time averaged Poynting vector) of an incident electromagnetic plane wave, and P_{abs} is the absorbed electromagnetic power by the object.

Thus, a simple calculation can be performed for the temperature rise after electromagnetic heating for a certain period of time

$$\Delta T = \frac{P_{abs}t}{\rho V C_P} = \frac{I\sigma_{abs}t}{\rho V C_P} \tag{2.101}$$

where ΔT is the temperature rise, t is the heating time, ρ is the density, V is the volume and C_P is the heat capacity.

For a spherical particle in a uniform medium, the temperature rise at a distance r away from the center of the particle, $\Delta T(r)$, can be modeled by [44]

$$\Delta T(r) = \frac{I\sigma_{abs}}{4\pi r k} \tag{2.102}$$

where k is the thermal conductivity of the medium. In most of the situations to be discussed, the particle is not spherical and it is usually placed on a substrate instead of in a uniform medium. As a result, equation (2.102) requires two corrections. First, it has been proven that for nonspherical particles it still applies as long as $r > R_{eff}$, where R_{eff} is the effective radius leading to a sphere with the same

volume as the non-spherical particle [45]. Second, for non-uniform media like the interface between a substrate and a surrounding medium, the thermal conductivity k should be replaced by the effective thermal conductivity $k_{eff} = k/b(r)$, and the distance dependent parameter $b(r)$ is calculated via [46]

$$b(r) = 1 + \frac{k_1 - k}{k_1 + k} \frac{r}{\sqrt{r^2 + 4R_{eff}^2}} \tag{2.103}$$

where k_1 is the thermal conductivity of the substrate and k is the thermal conductivity of the surrounding medium.

2.4.2 Femtosecond Laser Photothermal Damage of Plasmonic Nanoparticles

For plasmonic nanoparticles, the electromagnetic heating or photothermal effect is more pronounced due to the enhanced absorption cross section caused by LSPR. Also, because of the increased surface-to-volume ratio of the nanoparticles, there are more surface atoms which are more loosely bound compared to atoms in the bulk, causing the nanostructures to be more easily damaged by the incident laser. Moreover, for a laser pulse with femtosecond time duration, its interaction with the material under irradiation may not be described by the macroscopic electromagnetic heating and heat transfer theory in equation (2.98). The microscopic mechanism of femtosecond laser heating of nanoparticles needs to be investigated. Sun *et al.* studied electron and phonon thermalization in gold illuminated by a femtosecond laser [47][48]. The excited electron gas was thermalized via electron-electron scattering and the thermalization time was found to be hundreds of femtoseconds, while the electron-phonon was thermalized via electron-phonon scattering and the thermalization time was of the order of a picosecond. They utilized the two temperature model, considering the electron and lattice (phonon) temperatures, to explain the experimentally observed femtosecond laser induced change in the optical constants of a thin gold film. Ahmadi *et al.* used a pump-probe technique and the two temperature model to study the effects of femtosecond laser pulses on gold nanoparticles, and observed damping of the plasmon resonance due to the excitation of the cold electron gas [49]. The excitation of the electron gas showed two characteristic decay times of 2.5 ps and 50 ps, caused by electron-phonon and phonon-phonon interactions, respectively. Perner *et al.* demonstrated the same optical damping effect on plasmon resonance

and the characteristic decay times were 4 ps and 200 ps [50]. Link *et al.* studied the time scale of photothermal melting of gold nanorods [51]. Gold nanorods were melted and reshaped into nanospheres after 30-35 ps laser irradiation, independent of laser power and nanorod aspect-ratio. Link *et al.* investigated the laser pulse energy and pulse length dependence of the photothermal melting of gold nanorods via TEM imaging and UV-Vis spectroscopy [52]. The on-resonance, LSPR enhanced nanorods were shown to be more easily damaged by the incident laser pulse. Horiguchi *et al.* investigated the photothermal reshaping of gold nanorods via femtosecond pump-probe study [53]. Gold nanorods were heated to about 300-500 K and reshaped by picosecond laser pulse irradiation, and the heating effect was affected by the ligand capping layer on the nanorods. Bendix *et al.* showed the temperature measurement of electromagnetically heated gold nanoparticles via lipid bilayers and fluorescent molecules [54]. The temperature rise ranged from a few to hundreds of degrees Celsius depending on laser power and particle size. Ma *et al.* used the same method to investigate the polarization dependent photothermal heating of gold nanorods [44]. The heating effect was strongest when the incident laser was polarized along the long axis of the nanorods and the temperature rise was two orders of magnitude higher than the nanorods heated by the incident laser polarized perpendicular to the long axis of the nanorods. The nanorods were reshaped at a temperature of about 200-300 $°C$.

Summarizing the results found in the literature, a qualitative model consisting of different phases for femtosecond laser electromagnetic heating and photothermal reshaping or damage of plasmonic nanoparticles can be built. This model is especially applicable to, gold nanorods and can, reveal the microscopic picture of the physical mechanism. After illumination by a laser pulse, the electron gas immediately absorbs photon energy and a non-equilibrium distribution is built up. This is the phase of electron-photon interaction. Then, within several tens and up to hundreds of femtoseconds, the electron gas is thermalized and relaxes to an equilibrium distribution, but at a higher (electron) temperature. This is the phase of electron-electron interaction and the characteristic electron-electron scattering time is a few tens to hundreds of femtoseconds, consistent with the experimentally observed electron gas thermalization time. After a few picoseconds, the energy is transferred from the high temperature electron gas to the low temperature lattice or phonons. This is the phase of electron-phonon interaction, as the picosecond time

scale agrees with the characteristic electron-phonon scattering time. Lastly, the heat is dissipated into the environment (e.g. solution or substrate) after tens of picoseconds. This is the phase of phonon-phonon interaction and can be well described by the heat transfer theory in equation (2.98). The reshaping or damage occurs in the phonon-phonon interaction phase. If the heating is minor, the extra heat will be transferred to the environment and the nanoparticles are unlikely to be damaged. However, if the heating and (phonon) temperature rise are not negligible, the gold nanorods can be melted and reshaped. As discussed above, nanoscale gold particles are subject to a lower melting temperature (typically 400-600 K) due to LSPR enhanced absorption and a higher ratio of more weakly bound, highly mobile surface atoms. If the duration of the laser pulse is prolonged to nanosecond time scale, severe damage such as evaporation or fragmentation of the nanoparticles can take place [52].

2.4.3 Electron Temperature

As discussed in the previous section, the interactions of femtosecond laser pulse with metals and the associated electromagnetic heating effect are complicated, multi-step processes. Complete treatment of the problem requires a two-temperature model that considers the electron gas and lattice vibration (phonons) as two separate systems with their own temperatures and heat transfer between one another. Here, for simplicity, we primarily focus on the responses of the electron gas. Separating the electronic subsystem is valid since its response time is on the fs-scale, and much smaller than the ps-scale electron-phonon interactions and phonon-phonon interactions. Thus, the electron gas can be treated as an adiabatic system when it responds to the femtosecond laser pulse.

Assuming the initial and final temperatures of the electron gas are T_0 and T_f, the heat capacity of the electron gas is C_e, the volume of the system is V, and the deposited electromagnetic energy is Q, the following equation can be written:

$$\int_{T_0}^{T_f} C_e V dT = Q \tag{2.104}$$

According to the Sommerfeld model, the electron gas heat capacity scales linearly with temperature if the temperature is not very low (the standard of "very low"

varies from material to material but is usually in the range of tens of degrees Kelvin):

$$C_e = \gamma T \tag{2.105}$$

where γ is a material-dependent parameter.

Thus, the integral in equation (2.104) can be evaluated and the final temperature of the electron gas can be calculated:

$$T_f = \sqrt{\frac{2Q}{\gamma V} + T_0^2} \tag{2.106}$$

2.5 Numerical Simulations

Due to complex device structures, nanoscale dimensions and frequency-dependent material properties, the electromagnetic response of nanostructured photocathodes is simulated numerically. We use finite element method (FEM) based, commercial electromagnetic simulation software *COMSOL Multiphysics* to investigate the interactions between optical frequency electromagnetic waves and nanostructured photocathodes. The use of the FEM enables adaptive and highly non-uniform discretized mesh to deal with the problems involving various different dimensions, such as light interaction with subwavelength nanostructures where the optical wavelength is several hundred nanometers and the size of nanostructures is usually below 100 nm; and especially for plasmonic structures, the near-field decay length is tens of nanometers and the metal skin depth is only a few nanometers. Moreover, FEM usually solves the electromagnetic problems in frequency domain. Considering the frequency-dependent optical properties of materials, especially metals of which the permittivity values have a strong frequency dependence, the frequency-domain is a natural and accurate approach. It also matches with our experiment that uses a single frequency laser to drive the optical field emitters.

Electromagnetic simulation in *COMSOL* can be performed in AC/DC module or RF module. For AC/DC module, the quasi-static approximation is applied. There is no retardation effect or wave propagation; instead, electric and magnetic fields are oscillating harmonically with frequency ω (for electrostatics and magnetostatics, $\omega = 0$). For RF module, on the other hand, no approximation is made and solutions come from full electrodynamic treatment of the model.

FEM simulation of electromagnetic heating can also be performed within *COMSOL* by coupling the RF module with the heat transfer module.

Chapter 3: Modeling of Vertically-Standing Gold Nanopillars and Si Tips

The most commonly used geometry of (optical) field emitters is a sharp tip. The tip usually stands vertically on a substrate. In this chapter, we will study vertically standing optical field emitters made of Au or Si via numerical simulation. Electromagnetic heating of the emitter will also be investigated theoretically.

The enhancement of optical field by metallic tips has been studied previously in the literature. Novotny *et al.* theoretically studied the optical field enhancement around a laser-illuminated metal tip in water with potential applications as optical tweezers [55]. They showed the field enhancement and charge distribution under two different optical field polarizations of the incident laser and concluded that polarization along the tip axis resulted in larger field enhancement factor. Bachelot *et al.* experimentally studied the tip-enhanced optical field with a photosensitive thin film and compared the results with numerical simulations [56]. They systematically investigated the effect of tip geometry and illumination parameters on enhancement of the field. Zhang *et al.* numerically investigated the optical field enhancement of a conical metal tip illuminated by a focused beam and its application in tip-enhanced Raman spectroscopy (TERS) [57]. They correlated the field enhancement factor with the tip geometry and showed the contributions of LSPR at the tip apex and SPP propagating along the tip to the optical field enhancement. Enhancement factor up to 30X was shown, mainly due to LSPR of the finite metal tip structures.

3.1 Infinite Length Conical Gold Tip in Water

We first considered the local optical field enhancement around an Au tip illuminated by a laser and immersed in water, which is exact the situation discussed in [55], as a check for correctness of our model to be used in numerical investigations of optical field emitters with various structures and materials.

3.1.1 Two-Dimensional (2D) Model

The simulation was run for a 2D model in COMSOL. The Au tip had a conical shape with radius R=5 nm and half angle θ=8 degree. Boundaries of the model were set to scattering boundary condition that was a first-order absorbing boundary

condition for a plane wave and had almost zero reflection of electromagnetic waves. As the tip was connected to one of the boundaries, its length was effectively infinite. One of the boundaries was set as the excitation port and had a linearly polarized plane wave input. The electromagnetic frequency was set to that of 810 nm free-space wavelength light. Gold permittivity was $\epsilon = -24.9 + 1.57i$ and water permittivity was $\epsilon = 1.77$. The geometry was adaptively meshed with triangular elements of 0.5 nm minimum dimensions at the tip apex. Above simulation parameters were almost identical to the ones used in [55].

We considered two situations: the electric field of the optical wave was polarized along the tip axis or transverse to the tip axis. Simulation results are shown in Fig. 3.1, with the color scale indicating the field enhancement factor. The wave propagation vector **k** and polarization vector **E** are also illustrated. Now we define the field enhancement (factor) as

$$FE = \frac{E_{local}}{E_{optical}} \tag{3.1}$$

where $E_{optical}$ is the electric field amplitude of the incident optical wave and E_{local} is the maximum local electric field amplitude the at tip region. For electric field polarized transverse to the tip axis, about 1.5X field enhancement is achieved (Fig. 3.1(a)) and for electric field polarized along the tip axis, about 4.5X field enhancement is achieved. This polarization dependence is consistent with [55].

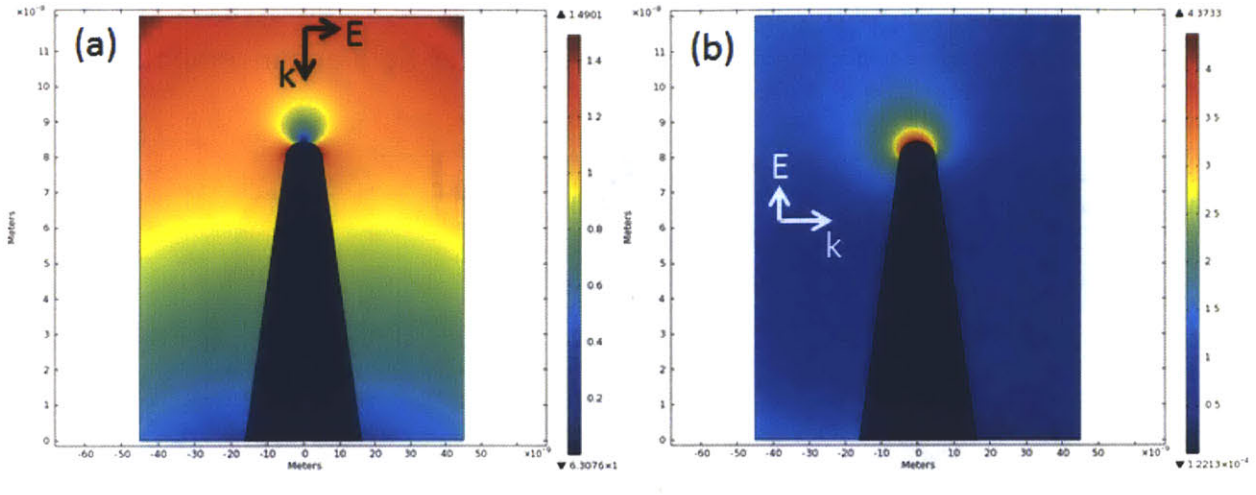

Fig. 3.1. Simulation of optical field enhancement by a 2D subwavelength conical Au tip in water. The wave incident directions are shown as **k** vectors and its polarizations indicated by **E** vectors. The color scale illustrates the field enhancement factor and the axes illustrate spatial dimensions. (a) Electric field is polarized transverse to the tip axis. The field enhancement factor is ~1.5. (b) Electric field is polarized along the tip axis. The field enhancement factor is ~4.5.

3.1.2 Three-Dimensional (3D) Model

Our results are in good agreement with [55] where the optical field enhancement by a 3D tip was studied. The difference comes from the 2D nature of our model, which assumes homogeneity in the third dimension. To address this problem, we also ran the 3D simulation of the tip, with the same parameters stated in Section 3.1.1. For 3D model FEM meshing, tetrahedral-shaped elements were used and the minimum element size was 0.5 nm at the tip apex. The simulated field enhancement profiles at the cut-plane through the tip axis and at the Au tip surface are shown in Fig. 3.2. Again, incident field polarized both along and transverse to the tip axis were considered. Local field enhancement is shown in Figs. 3.2 (a)&(c), which agrees perfectly with the results of [55]. For incident field polarized along the tip axis, the field enhancement is about 5X; while for incident field polarized perpendicular to the tip axis, the enhancement is only 2X. The surface field is also illustrated in Figs. 3.2 (b)&(d), indicating the charge distribution according to the discussion in section 2.2.3. The surface field profile or charge distribution also agrees with results in [55]. With incident field polarized along the tip axis, stronger field enhancement is achieved, consistent with the previous 2D model. The strong field is caused by the charge accumulation at the tip apex indicated by Fig. 3.2(b).

On the other hand, if incident field is polarized transverse to the tip axis, the charge is not accumulated at the tip apex and results in weaker field enhancement.

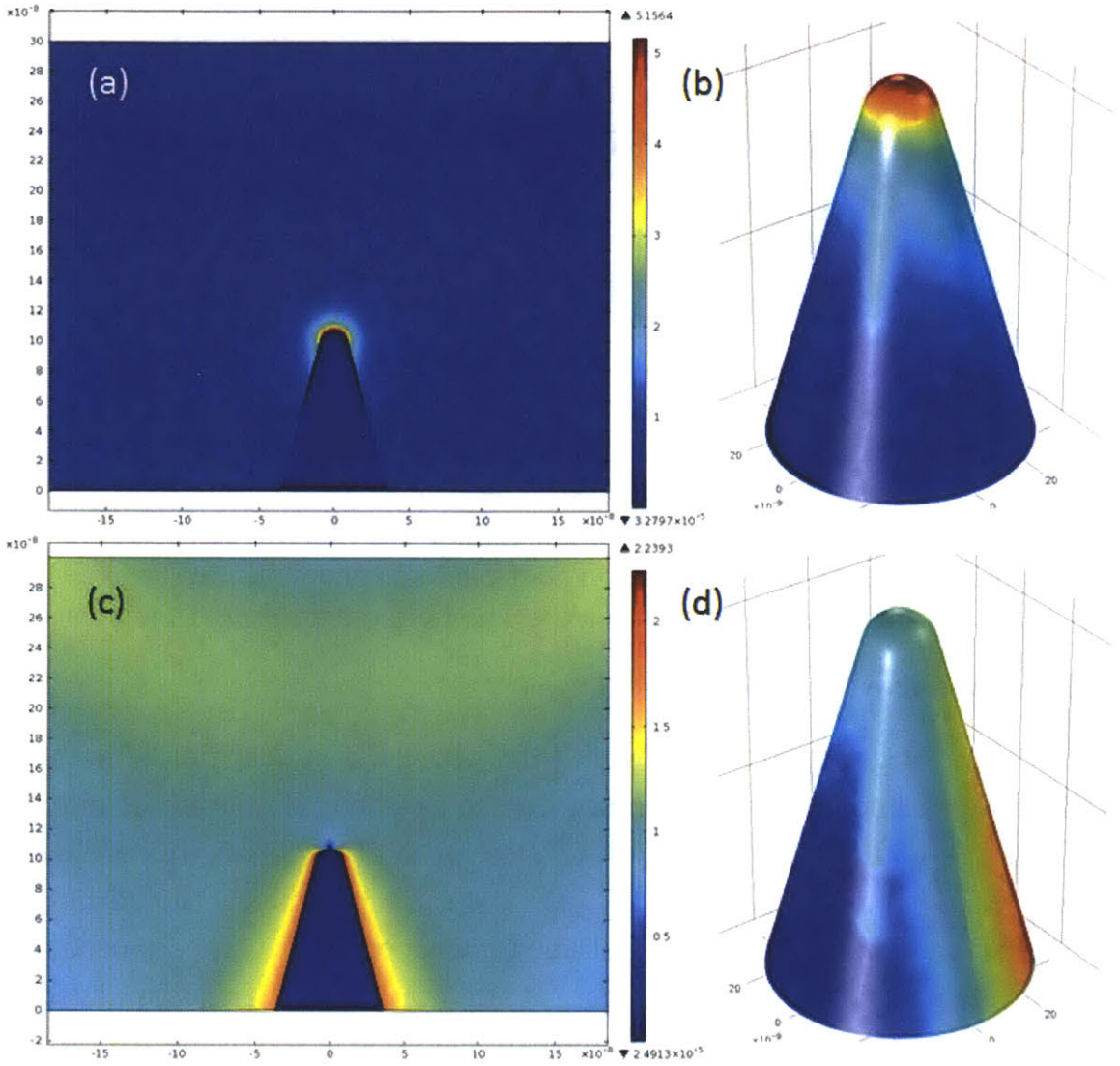

Fig. 3.2. Simulation of optical field enhancement by a 3D subwavelength conical Au tip in water. (a) Local field enhancement is shown in color scale for incident field polarized along the tip axis. Maximum field enhancement factor is ~5X. (b) Surface electric field (approximated charge accumulation) at the tip surface for incident field polarized along the tip axis. (c) Local field enhancement is shown in color scale for incident field polarized transverse to the tip axis. Maximum field enhancement factor is ~2X. (d) Surface electric field (approximated charge accumulation) at the tip surface for incident field polarized transverse to the tip axis.

This simple model of infinite length conical gold tip in water reproduced the results of [55], indicating that the optical field is enhanced around a metal tip with sub-wavelength dimensions and the enhancement factor is largely dependent on the polarization of incident optical field.

3.2 Gold Islands and Gold Pillars

Although conical-shaped tip structures are widely used in the science community to achieve both electrostatic and optical field enhancement [8-15][55-57], there are two shortcomings for this structure to be applied to compact and intense X-ray sources. First, compared to its small radius of curvature at the tip apex, the large-sized bottom prevents the integration of this structure into a compact array. Second and more importantly, this structure is non-uniform in the vertical direction, which imposes a serious challenge on today's planar micro-/nano-fabrication technology. Therefore, based on our capability of fabricating sub-10 nm structures, we proposed some non-conically nanostructured optical-field emitters. These nanostructures are easy to fabricate, and thousands and even millions of them should be able to be integrated as an array on an area of a few tens of microns with high yield.

3.2.1 Gold Islands

We first investigated the idea of small gold island optical-field emitters (Fig. 3.3(a)). The island was essentially a hemisphere with 5 nm radius. The edge at the bottom of the island was rounded in the model to avoid unwanted high field enhancement caused by sharp edges. The model was in 3D and the material properties and electromagnetic excitation parameters were chosen the same as previous models of gold tips in water. The illumination light had a wavelength $\lambda = 810\ nm$. Gold ($\epsilon = -24.9 + 1.57\text{i}$) and water ($\epsilon = 1.77$) were chosen as tip and dielectric materials, respectively. The 3D structure was meshed with tetrahedral-shaped elements with a 0.5 nm minimum dimension. Fig. 3.3(b) shows the simulation result of optical-field enhancement of this structure. The optical triggering field propagates in x-direction (from left to right) and is polarized in y-direction (in-plane and along the center axis of the island). The simulation result indicates a 1.5X optical field enhancement factor.

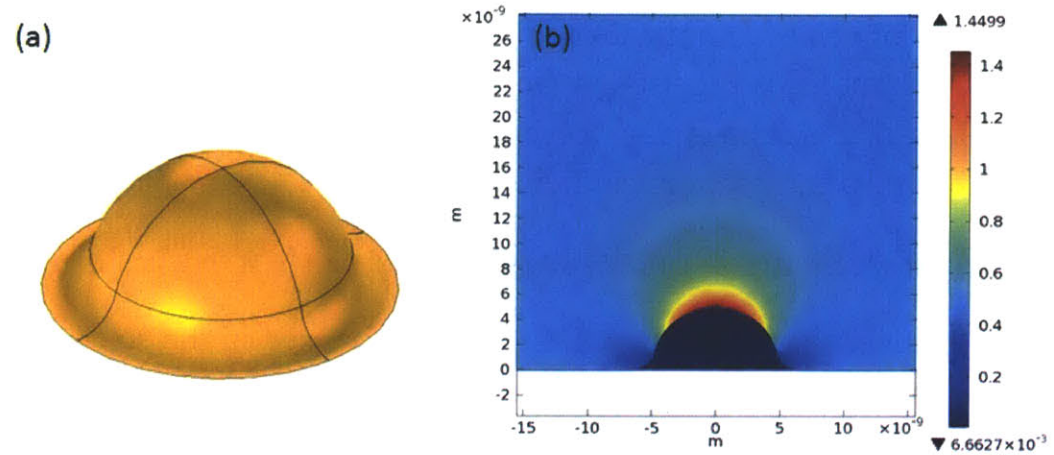

Fig. 3.3. Gold island optical-field emitter. (a) Geometry of the emitter; (b) simulated electric field enhancement factor around the emitter. Radius of the hemisphere emitter R=5nm. The illumination light has a wavelength $\lambda = 810\ nm$. Gold ($\epsilon = -24.9 + 1.57\text{i}$) and water ($\epsilon = 1.77$) were chosen as tip and dielectric materials, respectively. The optical triggering field propagates in x-direction (from left to right) and is polarized in y-direction (in-plane and along the tip axis). The field enhancement factor is ~1.5X.

3.2.2 Gold Pillars

We noticed the field enhancement factor of the gold island emitter is relatively small (< 2). We attributed this fact to the limited emitter height in the vertical direction. To verify this, we proposed another 3D bullet structure which was essentially a cylinder with a round end (Fig. 3.4(a)). The radius of the cylinder and the hemisphere top was 5 nm, while the length of the cylinder was 30 nm. Again, the structure was meshed with tetrahedral elements having a 0.5 nm minimum dimension. For this model, the dielectric material around the pillar was changed from water to vacuum, as photocathodes should be emitting electrons into the vacuum. Also, the optical wavelength was also changed from 810 nm to 800 nm, which was exactly the center wavelength of the Ti:sapphire laser to be used as the driving laser for our photocathodes. Fig. 3.4(b) shows the simulation result of optical-field enhancement of this structure. The polarization direction of the incident optical field was chosen to be along the axis of the pillar to result in a stronger field enhancement. Propagation (**k**) and polarization (**E**) directions are illustrated as arrows in the figure. Simulation result shows a field enhancement of about 3.7X at the top of the pillar.

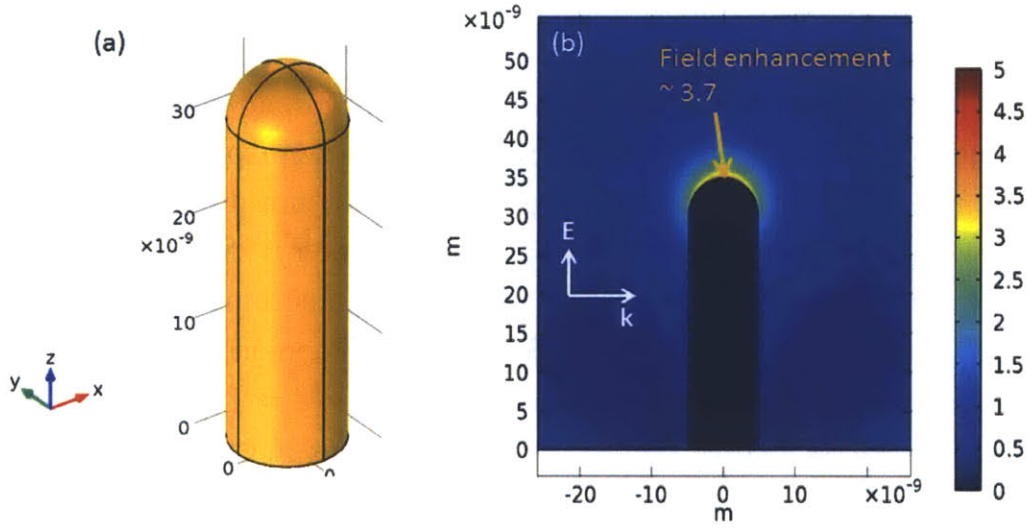

Fig. 3.4. Gold pillar optical-field emitter. (a) Geometry of the emitter; (b) simulated electric field strength around the emitter. Radius of the cylinder and hemisphere top is $R = 5\,nm$. Length of the cylinder is $L = 30\,nm$. The illumination light has a wavelength $\lambda = 800\,nm$. Gold ($\epsilon = -24.9 + 1.57\text{i}$) and vacuum ($\epsilon = 1$) were chosen as tip and dielectric materials, respectively. The optical triggering field propagates in x-direction (from left to right) and is polarized in y-direction (in-plane and along the tip axis). Propagation (**k**) and polarization (**E**) directions are illustrated as arrows. The color scale indicates the field enhancement, and the field enhancement factor of the Au pillar is ~3.7X.

Hence, the gold nanopillar is a suitable structure for optical field emitters. It maintains a small radius of curvature at the top to enhance the optical field, while its shape is more uniform in the vertical direction which simplifies the fabrication process and allows integration into large arrays with thousands and even millions of emitters.

3.3 Plasmonics Enhanced Gold Nanopillar

The Au pillars modeled in previous sections were connected to the boundary to which scattering boundary condition was applied. Thus, electromagnetic wave was absorbed and the pillar could be treated as of infinite length. For a finite tip or truncated tip, however, the electromagnetic wave, especially the surface wave, can be reflected, leading to a resonant behavior, localized surface plasmon resonance (LSPR), discussed in section 2.3.3.

3.3.1 Gold Nanopillar in Vacuum

LSPR is known to be wavelength and geometry dependent. As we are primarily interested in the optical field enhancement for light with 800 nm free space wavelength, we fixed the wavelength and studied the optimal geometry. The finite length Au nanopillar was modeled by a cylinder with hemisphere caps at the two ends. The diameter of the nanopillars was fixed to 10 nm and the length of the nanopillars was swept to find the optimal geometry. Scattering boundary conditions were applied to the excitation and absorbing boundaries. The illumination light has a wavelength $\lambda = 800\ nm$ and is polarized along the axis of the nanopillar. Gold ($\epsilon = -24.9 + 1.57\text{i}$) and vacuum ($\epsilon = 1$) were chosen as tip and dielectric materials, respectively. The structure was meshed with tetrahedral-shaped elements with a 3 nm minimum dimension.

Simulation results are shown in Fig. 3.5. for three nanopillars with 50 nm, 60 nm and 70 nm lengths. The 60 nm length Au nanopillar provides the strongest field enhancement factor of 55X. Hence, the field enhancement of the nanopillar does not monotonically change with increasing length and shows a clear resonant behavior.

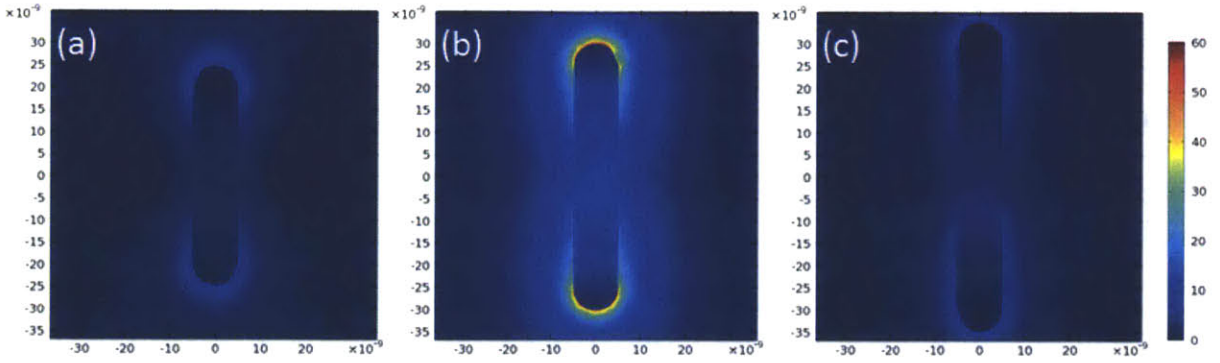

Fig. 3.5. Simulated near-field enhancement profile for Au nanopillars in vacuum. The nanopillar diameters are 10 nm and lengths are (a) 50 nm, (b) 60 nm, and (c) 70 nm. The illumination light has a wavelength $\lambda = 800\ nm$ and is polarized along the axis of the nanopillar. Gold ($\epsilon = -24.9 + 1.57\text{i}$) and vacuum ($\epsilon = 1$) are chosen as tip and dielectric materials, respectively. The 60 nm length Au nanopillar provide the strongest field enhancement factor of 55X.

3.3.2 Gold Nanopillar on Silicon Substrate with Titanium Adhesion Layer

We chose Si as the substrate for the Au nanopillar optical field emitters due to its easy accessibility. The substrate should be able to supply electrons to the

photocathodes and this can be done by doping the Si. For lithographically defined Au nanostructures deposited via evaporation, an adhesion promoting layer is usually deposited before the Au evaporation to improve the adhesion between Au nanostructures and the substrate. Commonly used materials for the adhesion layer are titanium (Ti), palladium (Pd) and chromium (Cr).

To more accurately simulate the optical field emitter structure that we will fabricate, we included a Si substrate as well as a Ti adhesion layer between the Au nanopillar and the substrate in the model. The diameter of the nanopillars was fixed to 10 nm and the height of the nanopillars was swept to find the optimal geometry. The thickness of Ti adhesion layer was 3 nm. Scattering boundary conditions were applied to the excitation and absorbing boundaries. The illumination light had a wavelength $\lambda = 800\,nm$ and was polarized along the axis of the nanopillar. Gold ($\epsilon = -24.9 + 1.57\mathrm{i}$) and silicon ($n = 3.69 + 6.5 \times 10^{-3}\mathrm{i}$) were chosen as tip and dielectric substrate materials, respectively, and a thin Ti ($n = 2.86 + 3.32\mathrm{i}$) layer was in between. The surrounding medium above the substrate was vacuum ($\epsilon = 1$). Tetrahedral meshing elements had a 1 nm minimum dimension for the adhesion layer and a 3 nm minimum dimension for the rest of the structure.

The simulated near-field enhancement profile is illustrated in Fig. 3.6. The field enhancement factors for the 25 nm, 35 nm and 45 nm height Au nanopillars are 9.3X, 13.2X and 6.1X. The resonant behavior associated with LSPR is clearly demonstrated. The 35 nm height Au nanopillar provides the strongest optical field enhancement and thus is the optimal geometry.

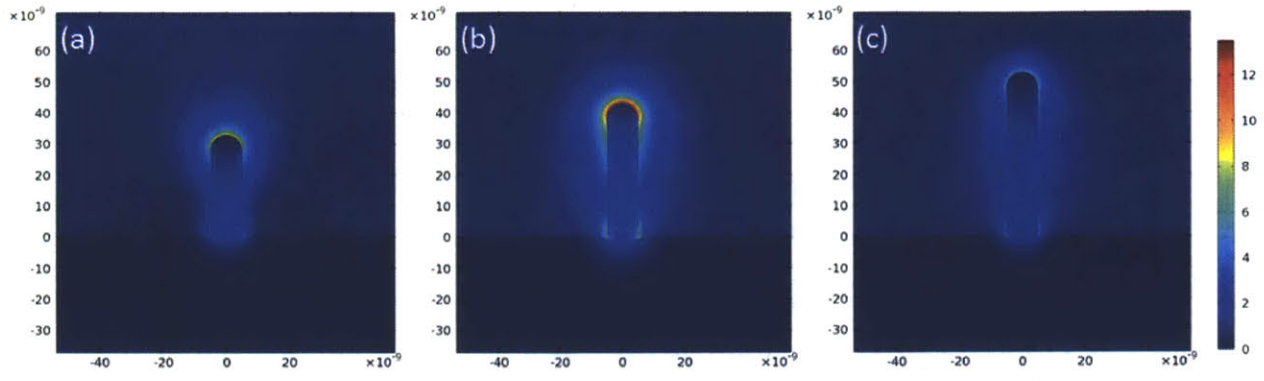

Fig. 3.6. Simulated near-field enhancement profile for Au nanopillars on Si substrate with Ti adhesion layer. The nanopillar diameters are 10 nm and lengths are (a) 25 nm, (b) 35 nm, and (c) 45 nm. The thickness of Ti adhesion layer is 3 nm. The illumination light has a wavelength $\lambda = 800\ nm$ and is polarized along the axis of the nanopillar. Gold ($\epsilon = -24.9 + 1.57\text{i}$) and silicon ($n = 3.69 + 6.5 \times 10^{-3}\text{i}$) are chosen as tip and dielectric substrate materials, respectively, and a thin Ti ($n = 2.86 + 3.32\text{i}$) layer is in between. The surrounding medium above the substrate is vacuum ($\epsilon = 1$). The 35 nm height Au nanopillar provides the strongest field enhancement factor of ~13X.

3.3.3 Tungsten Nanopillar on Silicon Substrate

For a nanoparticle to exhibit LSPR, it is required that its dielectric permittivity should have a negative real part. As to the Au nanopillar, its permittivity at 800 nm is $\epsilon = -24.9 + 1.57\text{i}$ so that LSPR is associated with it.

As a comparison, we also consider the nanopillar made of tungsten (W). At 800 nm, the refractive index of W is $n = 3.56 + 2.73\text{i}$, so its dielectric permittivity is $\epsilon = n^2 = 5.22 + 19.4\text{i}$. Note the real part is positive, so the W nanopillar does not have LSPR. Optical simulation results of W nanopillars are shown in Fig. 3.7. The diameter of the nanopillars was fixed to 10 nm and the height of the nanopillars was swept. Scattering boundary conditions were applied to the excitation and absorbing boundaries. The illumination light had a wavelength $\lambda = 800\ nm$ and was polarized along the axis of the nanopillar. The structure was meshed with tetrahedral-shaped elements with a 3 nm minimum dimension.

Fig. 3.7 shows three nanopillars with 30 nm, 50 nm and 70 nm heights. The field enhancement factors are 2.8X, 2.9X and 3.0X, respectively. No resonance with respect to geometry is observed. As expected, W nanopillars do not exhibit LSPR.

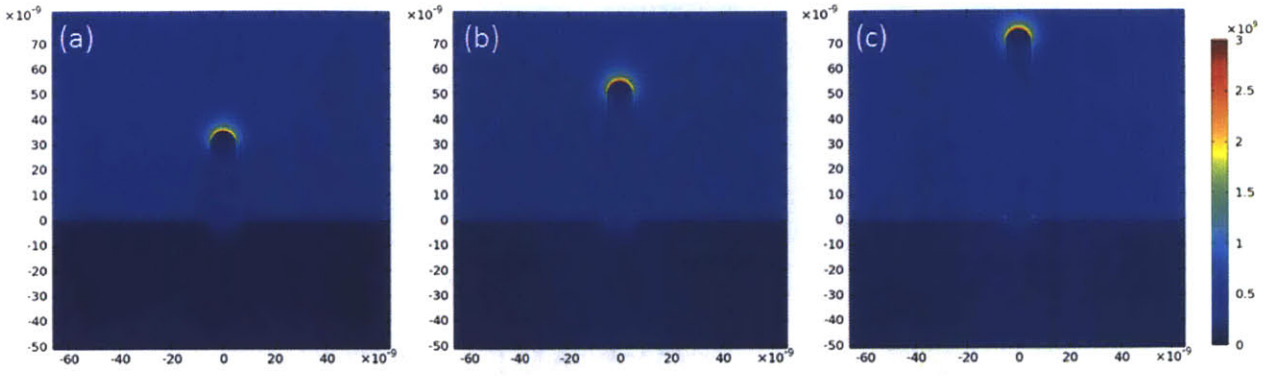

Fig. 3.7. Simulated near-field profile for W nanopillars on Si substrate. The nanopillar diameters are 10 nm and heights are (a) 30 nm, (b) 50 nm, and (c) 70 nm. The illumination light has a wavelength $\lambda = 800\ nm$ and is polarized along the axis of the nanopillar. Tungsten ($n = 3.56 + 2.73\mathrm{i}$) and silicon ($n = 3.69 + 6.5 \times 10^{-3}\mathrm{i}$) are chosen as tip and dielectric substrate materials, respectively. The surrounding medium above the substrate is vacuum ($\epsilon = 1$). The field enhancement factor slightly increases from 2.8X to 3.0X as the nanopillar height increases from 30 nm to 70 nm. No resonance with respect to geometry is observed.

3.4 Fabricated Gold Optical Field Emitters

In the models discussed in previous sections, the geometry of nanostructured gold optical field emitters was modeled by a cylinder with a hemisphere cap. Fig. 3.8 shows a SEM image of fabricated Au nanopillar arrays. It can be seen the geometry deviates from the ones in previous models. The fabricated Au optical field emitters have a tapered structure and the sidewall is not perfectly vertical, as suggested in Fig. 3.8 where the sidewall and bottom form an 80° angle. This tapered structure is caused by the closure of the holes in the resist during Au evaporation (the fabrication process will be discussed in Chapter 6). Moreover, the Au optical field emitters are embedded in a 10 nm thick silicon dioxide (SiO_2) film preventing electron emission from the substrate. Also, as discussed in section 3.3.3, there is a Ti adhesion layer between lithographically defined Au nanoparticles and Si substrate. The change of geometry as well as the dielectric environment can both affect the LSPR of the Au nanostructure. Thus, it is important to model the optical field emitter with the device architecture and geometrical parameters taken from the SEM image and fabrication process.

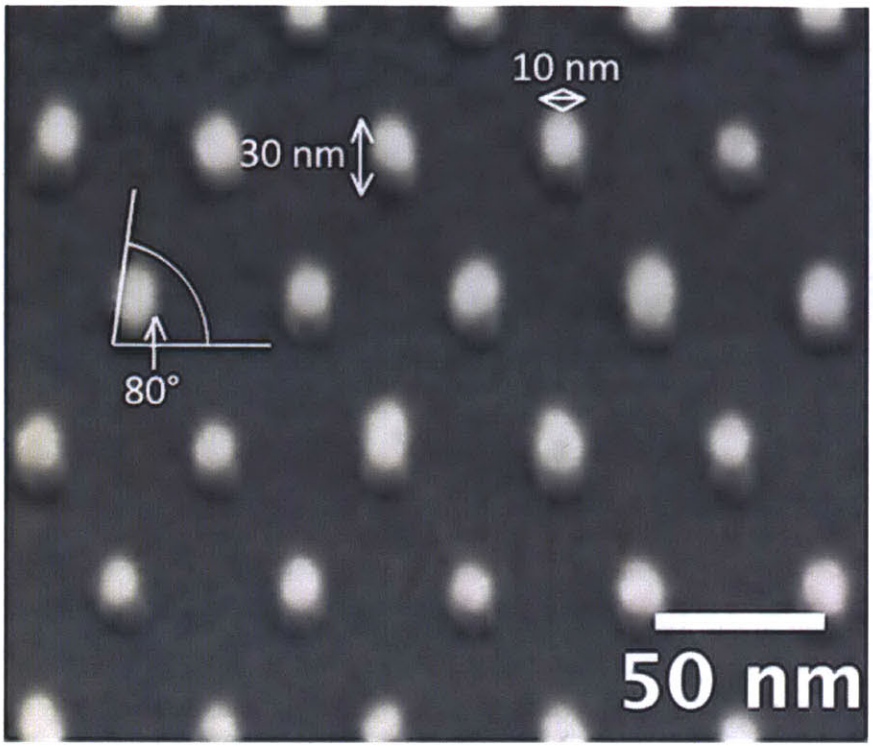

Fig. 3.8. SEM image of fabricated Au nanopillars with a pitch of 50 nm, tip diameter, height and sidewall angle are highlighted in the figure (*Courtesy of Dr. R. G. Hobbs*).

3.4.1 Near-field Profile and Field Enhancement Spectrum

We modeled the optical field enhancement of the fabricated Au optical field emitter and the result is shown in Fig. 3.9(a). The tip of the tapered nanopillar was modeled by a hemisphere with 10 nm diameter. The part of the emitter above the SiO_2 top surface was modeled by a cone with 80° sidewall angle and 17 nm bottom diameter, agreeing with the SEM image in Fig. 3.8. The part of the emitter embedded in SiO_2 was modeled by a cylinder. The total height of the Au optical field emitter was 40 nm. The thickness of Ti adhesion layer was 3 nm and the thickness of the SiO_2 film was 10 nm. Scattering boundary conditions were applied to the excitation and absorbing boundaries. The illumination light had a wavelength $\lambda = 800\ nm$ and was polarized along the axis of the nanopillar. Gold ($\epsilon = -24.9 + 1.57\mathrm{i}$) and silicon ($n = 3.69 + 6.5 \times 10^{-3}\mathrm{i}$) were chosen as tip and dielectric substrate materials, respectively, and a thin Ti ($n = 2.86 + 3.32\mathrm{i}$) layer was in between. The emitter was embedded in SiO_2 ($n = 1.5$). The surrounding medium above was vacuum ($\epsilon = 1$). The tetrahedral meshing elements had a 1 nm

minimum dimension for the adhesion layer and a 3 nm minimum dimension for the rest of the structure. The simulated optical field enhancement profile shows an enhancement factor of 9.8X.

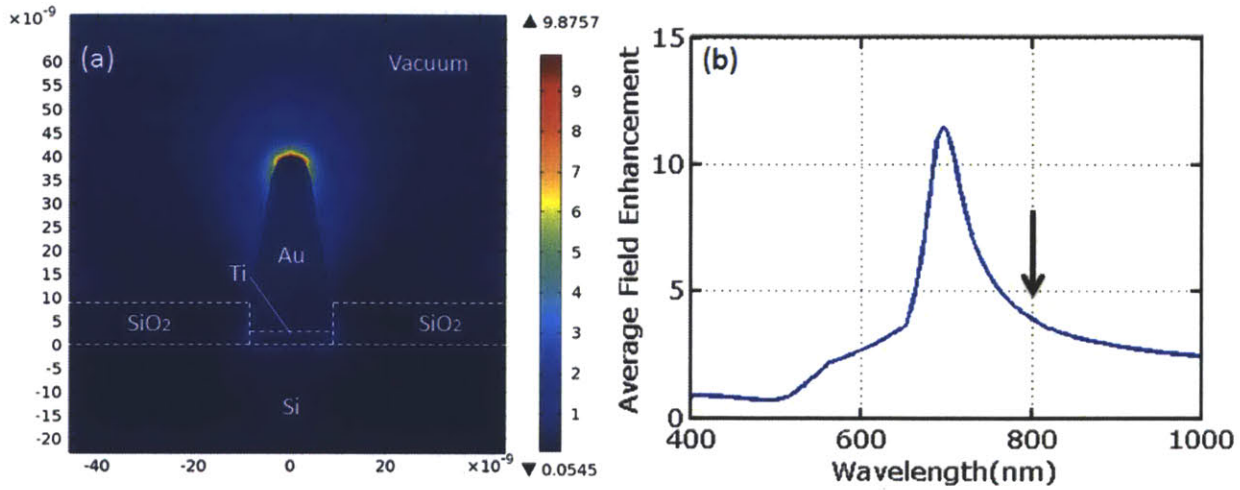

Fig. 3.9. Simulated optical field enhancement of the fabricated Au optical field emitter. (a) Simulated near-field enhancement profile on a cross section of the Au optical field emitter. The axes show dimensions in meter. Device structure and materials are illustrated. The illumination light has a wavelength $\lambda = 800\ nm$ and is polarized along the axis of the tapered nanopillar. The color scale shows the field enhancement factor. Peak field enhancement of 9.9X is achieved. (b) Simulated field enhancement spectrum of the optical field emitter. Average field enhancement is plotted as a function of the wavelength of incident light. Device structure is the same as in (a). The near-field profile shown in (a) corresponds to the black arrow in (b), at 800 nm. The LSPR peak is at 700 nm.

In order to identify the plasmon resonance band, we also swept the incident light wavelength from 400 nm to 1 um and plotted the simulated field enhancement spectrum (field enhancement factor as a function of wavelength). The device structure, material and FEM meshing were the same as described above. The material dielectric constants were implemented as frequency dependent functions taken from experiment. For Au and Ti, the dielectric functions were taken from Johnson & Christy [58]; for Si and SiO_2, the dielectric functions were taken from Palik [59]. As with the field enhancement factor, we took the average field enhancement at the surface S of the hemisphere atop the optical field emitter

$$Average\ FE = \frac{\frac{1}{S}\iint_S E_{local} \cdot da}{E_{optical}} \tag{3.2}$$

to avoid any meshing dependent numerical artifacts that have a strong effect on the value of the peak strength of the local electric field. The average field enhancement spectrum is shown in Fig. 3.9(b), with the black arrow at 800 nm indicating the optical wavelength of Fig. 3.9(a). The longitudinal LSPR mode of the tapered Au nanopillar is indicated by the peak of the spectrum, centered around 700 nm. To achieve a stronger field enhancement at 800 nm used in experiment, the optical field emitter structure needs to be optimized so that the LSPR peak can be shifted to 800 nm.

3.4.2 Geometry Optimization of the Fabricated Au Optical Field Emitter

As discussed in the previous section, the fabricated Au optical field emitter does not exhibit LSPR right at 800 nm, the wavelength of the driving laser used in experiment. Moreover, its complex geometry due to embedding in SiO_2 and tapering caused by evaporating Au through a small hole in the resist, as well as the complicated dielectric environment such as electrical contact provided by Si substrate and Ti adhesion layer, are all unique to our application and unlike any of the plasmonic structures investigated in literature, while strongly modifying the plasmonic resonances of our nanostructured optical field emitters. Therefore, we need to optimize the structure so that strongest optical field enhancement can be achieved via LSPR, and photocathode efficiency and charge yield can be maximized.

The complex structure of the fabricated Au optical field emitter results in several geometrical parameters to be optimized. The structure was outlined previously and here we point out some key dimensions: emitter base radius/diameter (radius/diameter of the hole in SiO_2 thin film defined by lithography), emitter height above the Si substrate, emitter sidewall tapering angle (angle between sidewall and bottom), emitter tip radius of curvature (radius of the hemisphere atop the emitter), thickness of the SiO_2 thin film, and thickness of the Ti adhesion layer. In the model, the boundary conditions and electromagnetic excitations, materials and their properties, as well as FEM meshing are all identical to the model discussed in the previous section.

We first considered the two most conveniently adjustable parameters, the emitter height, which is controlled by evaporated Au thickness, and the emitter base diameter, which is controlled by lithography defined pattern. Fig. 3.10 shows optical modeling of three fabricated Au optical field emitters with various emitter heights: 40 nm (Fig. 3.10(a)), 55 nm (Fig. 3.10(b)) and 70 nm (Fig. 3.10(c)). The SiO_2 thickness was fixed to 10 nm, the Ti thickness was fixed to 3 nm, sidewall angle was fixed to 80°, and the base radius was fixed to 8.5 nm. The emitter geometry was constructed with smooth surface (tangential transition), so that the tip radius changed slightly with varying emitter height. Again, resonant field enhancement is observed from the simulation results. Emitter with 40 nm, 55 nm and 70 nm height induce peak field enhancement factors of 11.6X, 47.6X and 13.5X, respectively. With other parameters fixed to values stated above, a 55 nm height emitter represents the optimal geometry that has the strongest optical field enhancement.

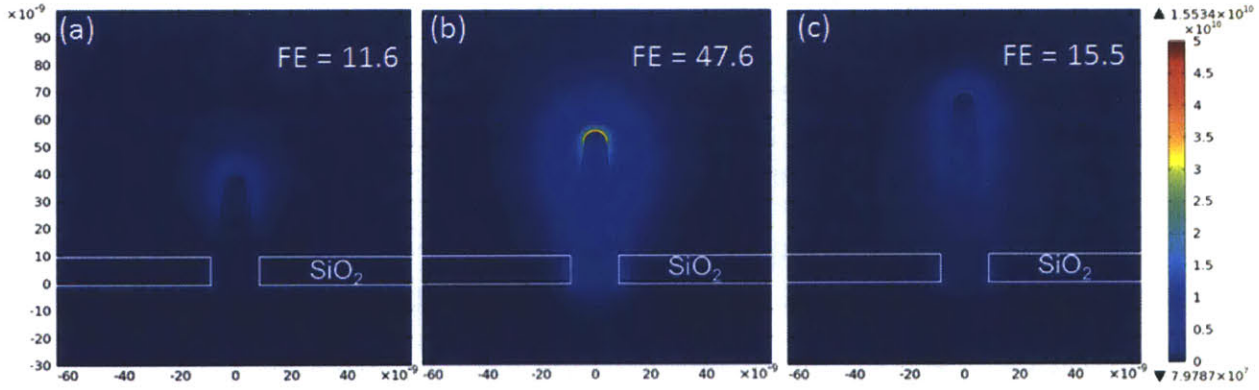

Fig. 3.10. Simulated optical near-field of fabricated Au optical field emitters with various emitter heights (above the Si substrate): (a) 40 nm; (b) 55 nm; and (c) 70 nm. The incident field of the 800 nm plane wave is 1 GV/m. The color scale shows the optical near-field. Peak field enhancements of the three emitters with different heights are labeled in the figures. Emitter with 55 nm height has the strongest field enhancement and the peak enhancement factor reaches 47.6X.

As for the optimization of base radius, Fig. 3.11 shows optical modeling of three fabricated Au optical field emitters with various emitter base radii: 5 nm (Fig. 3.11(a)), 5.5 nm (Fig. 3.11(b)) and 6.5 nm (Fig. 3.11(c)). The SiO_2 thickness was fixed to 10 nm, the Ti thickness was fixed to 3 nm, the tip radius was fixed to 4 nm, and the height was fixed to 40 nm. The emitter geometry was constructed with smooth surface (tangential transition), so that the sidewall angle changed slightly

with varying emitter base radii. Again, resonant field enhancement is observed from the simulation results. Emitter with 5 nm, 5.5 nm and 6.5 nm base radii induce peak field enhancement factors of 19.4X, 25.3X and 16.9X, respectively. With other parameters fixed to values stated above, a 5.5 nm base radius emitter represents the optimal geometry that has the strongest optical field enhancement.

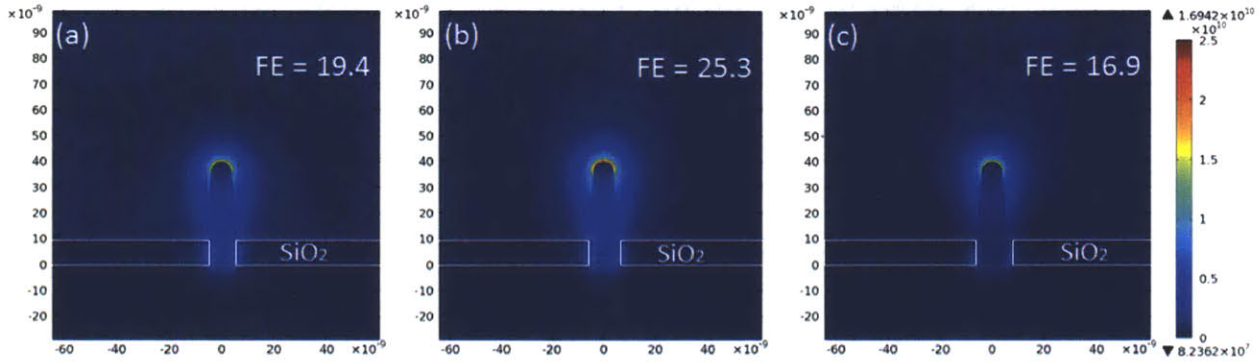

Fig. 3.11. Simulated optical near-field of fabricated Au optical field emitters with various emitter base radii: (a) 5 nm; (b) 5.5 nm; and (c) 6.5 nm. The incident field of the 800 nm plane wave is 1 GV/m. The color scale shows the optical near-field. Peak field enhancements of the three emitters with different base radii are labeled in the figures. Emitter with 5.5 nm radius has the strongest field enhancement and the peak enhancement factor reaches 25.3X.

The parametric sweeps of emitter height and emitter base radius discussed above were achieved by varying one parameter while maintaining the values of other parameters. However, the shape of the emitter was thus changed, as can be seen from Fig. 3.10 and Fig. 3.11. We also ran optical modeling of the fabricated Au emitter with varying sizes while maintaining the shape of the emitter. This was accomplished by fixing the sidewall angle so that the emitter height and base radius were interlocked. Fig. 3.12 shows the *average* field enhancement (introduced in section 3.4.1) of the emitters with varying base radius (and height since it changes with base radius). The tip radius was fixed to 3 nm, the Ti thickness was fixed to 3 nm, and sidewall angle was fixed to 80°. Average field enhancement was calculated by averaging the local field enhancement at the surface of the hemisphere atop the optical field emitter for base radius ranging from 5 nm to 25 nm. The effect of SiO_2 thickness was also investigated by choosing different thickness values.

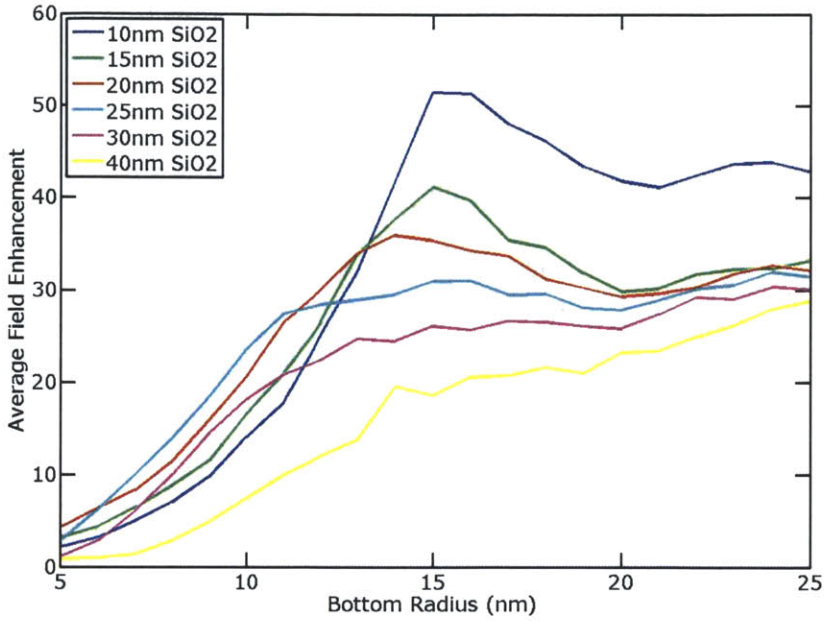

Fig. 3.12. Simulated average field enhancement for fabricated Au optical field emitters with a fixed shape and varying size (see text for details). The effect of SiO_2 thickness is also investigated by choosing different thickness values indicated in the figure legend.

Care must be taken when interpreting Fig. 3.12. Since the shape (sidewall angle) is fixed, the emitter height can be calculated from its base radius. A base radius of 10 nm thus corresponds to a height of 58 nm, which is about the upper limit of the Au thickness that can be evaporated in the fabrication process (see Chapter 6 for more details). Thus, the valid range of our Au optical field emitters is in 5-10 nm base radius. In this regime, *no* resonant field enhancement with respect to emitter size was observed. Therefore, when the shape of the Au nanostructure is fixed, its optical response depends only weakly on its size. The strong shape dependence and weak size dependence are typical for LSPR of metallic nanoparticles.

It can also be inferred from Fig. 3.12 that there is resonant field enhancement with respect to SiO_2 thickness. Within the fabrication-process-limited regime (5-10 nm base radius), the strongest field enhancement was achieved for 20-25 nm thick SiO_2 thin film. The varying SiO_2 thickness can be viewed to change the effective average medium index around the Au nanostructure. The resonance with respect to medium dielectric permittivity for a fixed geometry metallic nanostructure at a fixed frequency (free-space optical wavelength) is another footprint of LSPR.

From the above analyses, we can conclude that both the shape and the size of the Au optical field emitter, as well as the dielectric environment, have an effect on its LSPR. The shape is primarily determined by the sidewall angle of the tapered Au emitter, and the size is determined by the emitter base radius and emitter height, which are interlocked if the sidewall angle is fixed. The dielectric environment, on the other hand, is modified by varying the thickness of SiO_2 thin film. Thus, we performed a systematic multi-variable optimization to find the maximum optical field enhancement: the shape (sidewall angle) and the size (base radius) of the emitter were varied simultaneously and three different thicknesses of SiO_2 were considered.

The numerically calculated average field enhancement factor for different combinations for variables are shown in Figs. 3.13, 3.14 and 3.15. The sidewall angle of the emitter was varied from 75° to 85°, which is the range measure from the SEM image. The base radius of the emitter was varied from 5 nm to 15 nm. The SiO_2 thicknesses were 10 nm (Fig. 3.13), 20 nm (Fig. 3.14) and 30 nm (Fig. 3.15). By fixing the base radius and varying the sidewall angle (one "row" in the figures), resonance of average field enhancement can be observed. On the other hand, by fixing the sidewall angle and varying the base radius (one "column" in the figures), the average field enhancement is either less affected or monotonically changing and no obvious resonance can be seen. Moreover, there is a trend that for smaller base radius emitter, the optimal geometry is shifted to larger sidewall angle. As known for LSPR, smaller nanoparticle size usually leads to a blueshift of the resonance peak in the spectrum. But a larger sidewall angle results in higher aspect-ratio, leading to a redshift of the resonance peak. Hence, these two effects can cancel each other and generate the trend mentioned above. This trend is strongest for the 10 nm SiO_2 thickness situation, and becomes less notable with increasing SiO_2 thickness. This is because the emitter part embedded in the SiO_2 was modeled by a cylinder and with increasing SiO_2 thickness, it gradually turns into a major part of the emitter, thus diminishing the effect of sidewall angle on the aspect-ratio of the whole emitter.

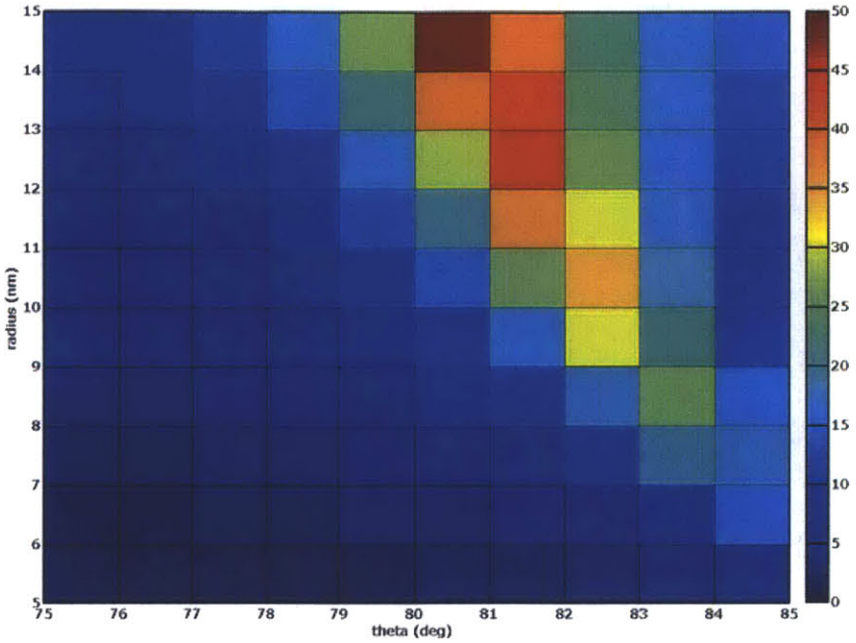

Fig. 3.13. Numerically calculated average field enhancement factor of varying sidewall angle and base radius. The SiO_2 thickness is 10 nm. The color scale illustrates the value of the average field enhancement.

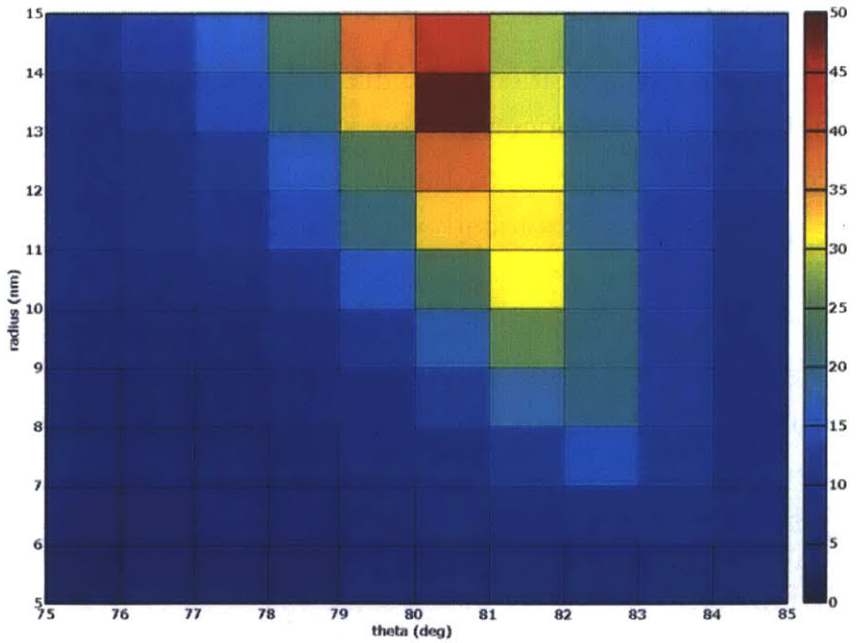

Fig. 3.14. Numerically calculated average field enhancement factor of varying sidewall angle and base radius. The SiO_2 thickness is 20 nm. The color scale illustrates the value of the average field enhancement.

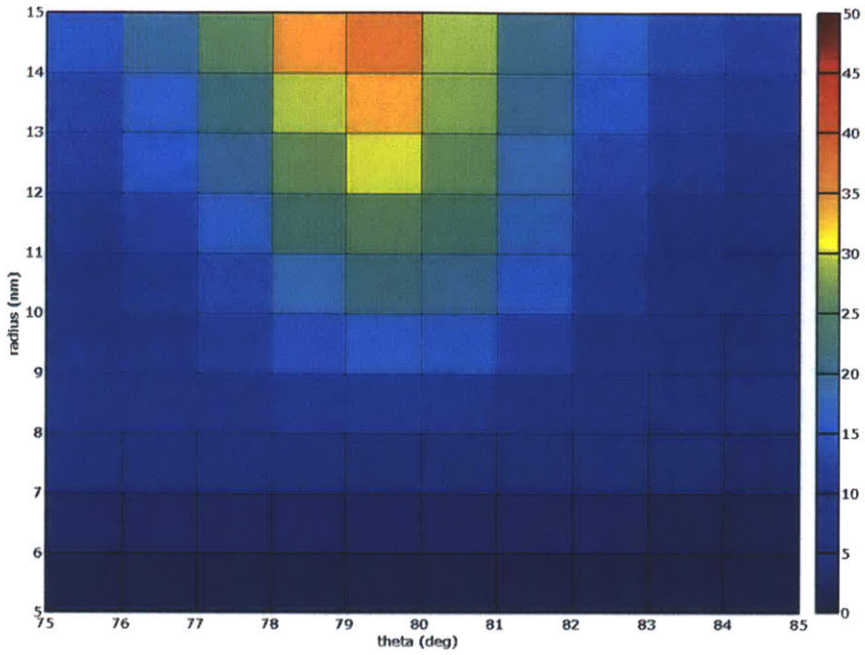

Fig. 3.15. Numerically calculated average field enhancement factor of varying sidewall angle and base radius. The SiO_2 thickness is 30 nm. The color scale illustrates the value of the average field enhancement.

3.5 Field Enhancement by Silicon Tips

For comparison with the plasmonics enhanced metallic nanopillars, we also modeled the optical field enhancement by silicon (Si) tips. Silicon is the most commonly used material for semiconductor electronic devices and its processing techniques are quite mature. Photocathodes made of arrays of Si tips have been discussed in [16-21]. Recently, [60] presented a simple way of fabricating atomically sharp Si tips with relatively low-resolution optical projecting lithography. The Si was first selectively oxidized so that two adjacent oxidized regions could form a sharp Si structure. The tip radius of curvature, or sharpness, can be controlled by varying the oxidation time. Then, the oxide was removed to reveal the Si tips.

3.5.1 Sharp Si Tip

The cut-plane of 3D geometry and optical modeling results of Si tips are shown in Fig. 3.16 with tip radius ranging from 10 nm to 50 nm. The smoothly curved side of the tip was modeled by taking points from the SEM image in [60] and fitting

with a cubic function. The structure was meshed with tetrahedral elements with a 1 nm minimum dimension at the tip apex. The 800 nm wavelength optical triggering field propagates in x-direction (from left to right) and is polarized in y-direction (in-plane and along the tip axis). Scattering boundary conditions were used for plane wave excitation and absorption of most of the outgoing optical waves. The model consists of Si tip and substrate in vacuum environment. The optical constant of intrinsic silicon at 800 nm, $n = 3.69 + 6.5 \times 10^{-3}\mathrm{i}$, was used and doping caused permittivity change was neglected at the point. The incident field strength was set to $E_{optical} = 2\ GV/m$, and the local field strength is illustrated in the figures. Field enhancement factor was calculated from equation (3.1) and also illustrated.

As expected, the optical field enhancement increases with decreasing radius of curvature of the tip. This can be immediately understood from the lightning rod effect. With smaller structures, the electric field lines will be more crowded, leading to a higher field enhancement. It is also interesting to compare the Si tips discussed here with the metal tips discussed in previous sections. With the similar dimensions (e.g. 10-20 nm radius), metal tips at plasmonic resonance (Figs. 3.10 & 3.11) can induce a much stronger near-field than Si tips (Fig. 3.16). According to the discussion in section (2.3), the strong near-field associated with the plasmonc resonance is beneficial for increasing the electron emission yield from optical field emitters, indicating a higher emission current density from plasmonics enhanced metal tips than from Si tips.

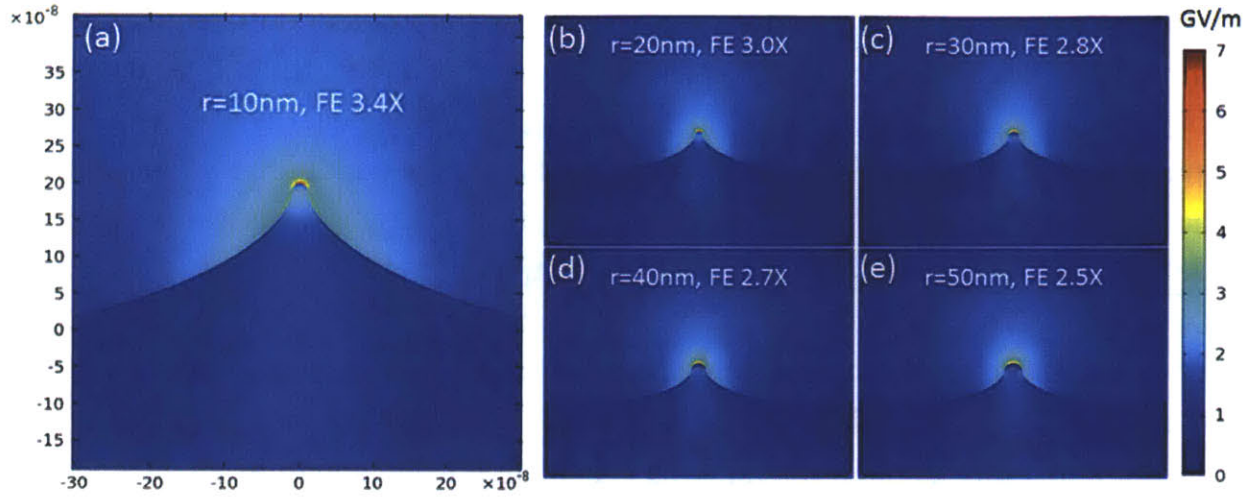

Fig. 3.16. Optical field enhancement by Si tips. (a)-(e), Si tips with radius of 10, 20, 30, 40 and 50 nm. The smoothly curved side of the tip is modeled by taking points from the SEM image in [60] and fitting with a cubic function. Silicon ($n = 3.69 + 6.5 \times 10^{-3}\mathrm{i}$) and vacuum ($n = 1$) are chosen as materials for the tip and surrounding medium, respectively. The color scale shows the local field strength while the incident optical field strength is 2 GV/m. The calculated field enhancement factors for the five tips are 3.4X, 3.0X, 2.8X, 2.7X and 2.5X, respectively. The 800 nm wavelength optical triggering field propagates in x-direction (from left to right) and is polarized in y-direction (in-plane and along the tip axis).

3.5.2 Blunt Si Mesa

By changing the oxidation time in the fabrication process, blunt Si tips, or mesa structures, can be made. Due to the large emission area, blunt tips can generate higher emission current [8]. Fig. 3.17(a) shows the SEM image of one blunt Si mesa structure with the key dimensions labeled in the figure: mesa height is 200 nm, diameter of the top is 240 nm, radius of curvature of the edge is 7 nm, and radius of curvature of the sidewall is 261 nm. Geometry of the 3D model is shown in Fig. 3.17(b) with dimensions taken from the SEM image. Electromagnetic excitation is also shown in the figure, with 800 nm incident plane wave propagation direction in the x-z plane with 60° away from z-axis and its polarization also in the x-z plane. In order to achieve this oblique incidence condition, we adopted a new way of defining boundary conditions. The top boundary used port boundary condition as electromagnetic excitation of 800 nm

plane wave with designated propagation direction (**k** vector) and polarization. Consistent with the port boundary condition, Floquet periodic boundary conditions were applied to the four sidewall boundaries of the model. The combination of port boundary condition and Floquet periodic boundary condition applied to one "unit cell" of an array (Fig. 3.17(b)) is best suited for simulating an array of identical structures with an oblique incident plane wave, which is exactly the situation for our optical field emitter arrays. The size of the unit cell was $2\ \mu m \times 2\ \mu m$, corresponding to a square array with $2\ \mu m$ pitch. This pitch should be large enough to prevent strong mutual coupling between adjacent structures in the array. A perfectly matched layer (PML) was added to the bottom of the model to perfectly absorb the electromagnetic waves and avoid any reflection from the boundary. The structure was meshed with tetrahedral elements with a 1 nm minimum dimension at the mesa edge. Periodic boundary condition pairs had identical triangular element meshing to avoid numerical artifacts associated with different meshing of periodically identical boundaries. Material properties were identical to the model in the previous section.

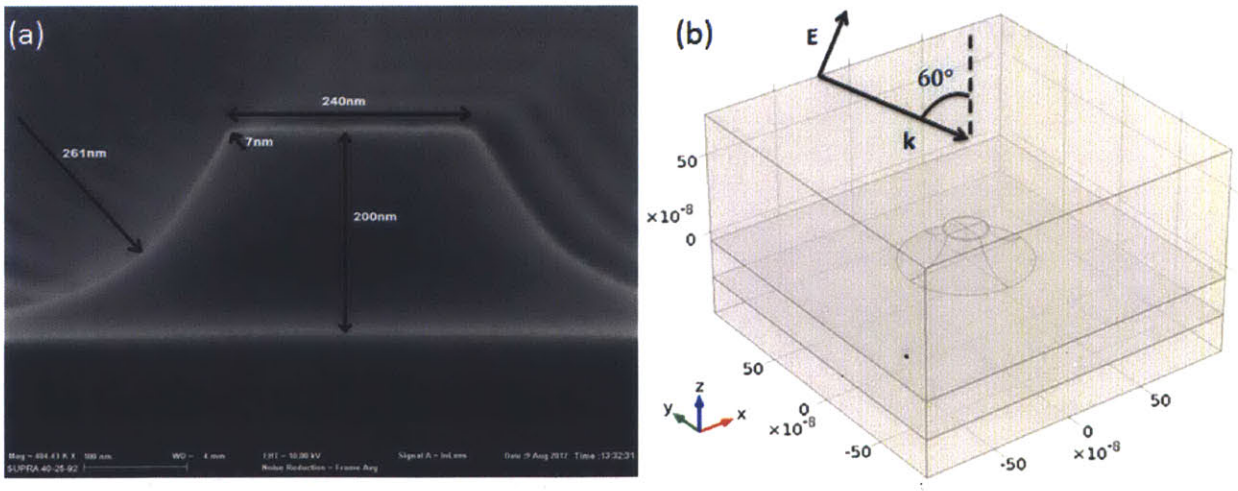

Fig. 3.17. Blunt Si mesa structure. (a) SEM image of an array of the mesa structures (Courtesy of Dr. M. Swanwick). Key dimensions are labeled in the figure: mesa height is 200 nm, diameter of the top is 240 nm, radius of curvature of the edge is 7 nm, and radius of curvature of the sidewall is 261 nm. (b) Model setup of the mesa structure with geometrical dimensions taken from the SEM image. Electromagnetic excitation is also shown. Incident plane wave propagation direction is in the x-z plane with 60° away from z-axis. Its polarization is also in the x-z plane.

The simulated optical near-field enhancement profile of the mesa structure is illustrated in Fig. 3.18. The y-z and x-z cut planes are shown in Figs. 3.18 (a)&(b), respectively. In the y-z cut plane (Fig. 3.18(a)), the peak field enhancement is about 2.8X; and in the x-z cut plane (Fig. 3.18(b)), the peak field enhancement is about 5.3X. To get a better understanding of the optical field enhancement of the whole mesa structure, Figs. 3.18 (c)&(d) illustrate the 3D field enhancement profile evaluated at the surface of the mesa structure. It can be seen the strongest field enhancement is located at the edge of the mesa structure, which is expected due to the edge sharpness. Thus, the 3D field enhancement profile forms a ring shape at the edge surrounding the top surface of the mesa, indicating high photo-induced emission current density at this ring. Therefore, the increased photoemission current is not due to the large area of the top of the mesa, but due to the long, sharp edge of the top surface. Since we do not need a ring-shape photoemission current profile from the optical field emitter and the emittance of the mesa structure optical field emitter can be huge due to the large emitter area, the blunt Si mesa structure is not suited for the nanostructured photocathodes of compact X-ray sources. Nevertheless, it may be used in applications requiring a high photoelectron emission current.

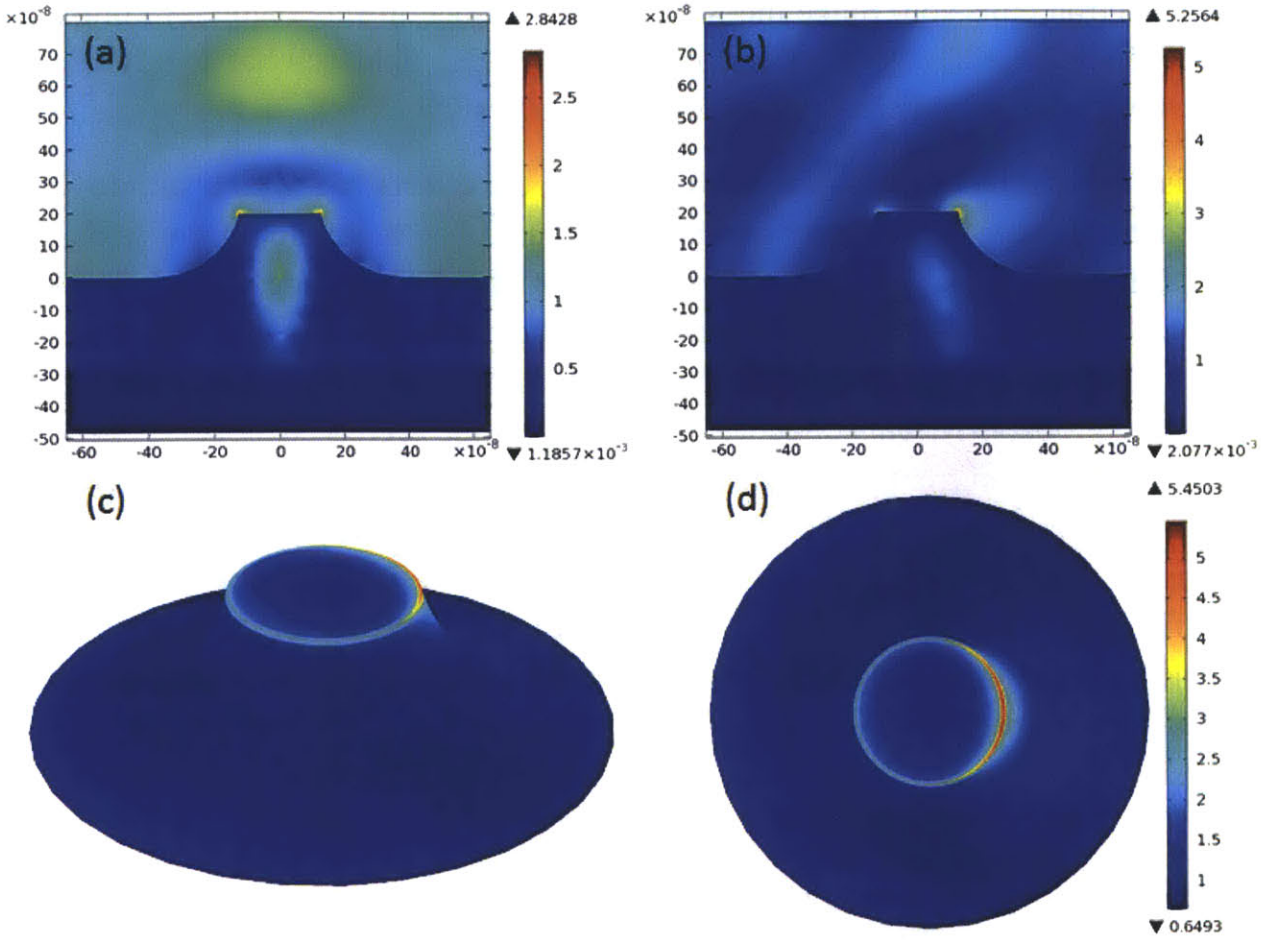

Fig. 3.18. Simulated optical near-field enhancement profile of the blunt Si mesa structure. (a) y-z cut plane. (b) x-z cut plane. (c) Side view and (d) top view of the 3D field enhancement profile evaluated at the surface of the mesa structure. Silicon ($n = 3.69 + 6.5 \times 10^{-3}$i) and vacuum ($n = 1$) are chosen as materials for the tip and surrounding medium, respectively. The color scale shows the local field enhancement factor. The strongest field enhancement is located at the ring-shape edge of the top surface with a field enhancement factor at the ring ranging from 2.8X to 5.3X.

3.6 Electrostatic Field Enhancement

For the photocathodes used in experiment, there is always an applied electrostatic (DC) or radio-frequency (RF) field extracting the photoelectrons from the photocathodes. Due to the nanometer scale sharpness of our optical field emitters, the local DC or RF field at the emitter surface can also be enhanced by crowding of the field lines, potentially interfering with the optical field enhancement. Thus, it is important to understand the DC/RF field enhancement and how it affects the

photoelectron emission. Since the RF field has a much lower frequency compared to the optical field, its effect is similar to the DC field so that the following discussion will primarily focus on the electrostatic situation.

As discussed in literature [8-15] and Chapter 2, the effects of DC field are different for photocathodes in different operating regimes. For multiphoton emission, the optical field is weak and comparable to the DC field. Therefore, the existence of DC field greatly reduces the thickness of the vacuum barrier, facilitating the transition from multiphoton emission to optical field emission by increasing the tunneling probability. This effect can be seen from the decreased slope of the curve of the emission current (or electron counts) versus laser power [10], indicating lower photon number is required due to tunneling assisted by the DC field. On the other hand, for optical field emission, the optical field is much stronger than the DC field of which the effect is much more suppressed. Furthermore, due to Schottky effect, the DC field can lower the effective work function, which enhances electron emission for both multiphoton emission and optical field emission. Finally, the DC field also alleviates the space charge effect of emitted electrons, hence improving the electron emission [61].

We ran electrostatic simulation of the Au nanopillar emitter on Si substrate in COMSOL AC/DC module. The diameter and height of the nanopillar is 10 nm and 35 nm, respectively. The geometry and meshing of the electrostatic model is identical to the optical models in previous sections. As Au is a metal and the Si substrate is heavily doped, the surface of the emitters and substrate was modeled as perfect electric conductor (PEC). Terminal and ground boundary conditions were applied to the top boundary and PEC, respectively. A background (pre-enhanced) DC field of 100 MV/m was created by choosing a 1000 V terminal voltage and a 10 μm dielectric (vacuum) spacer between the terminal and PEC. Periodic boundary condition was applied to simulate a square array of nanopillars. Two arrays with 100 nm and 1 μm pitches were considered.

The graphs displayed in Fig. 3.19 show the results of the simulations of local electrostatic field strength near the Au nanopillars. The graphs show a slight decrease in the field enhancement factor from 9.2X to 8.1X as the nanopillar pitch is reduced tenfold from 1 μm to 100 nm, caused by the screening effect. However, the areal nanopillar density increases by a factor of 100 as the pitch is reduced by a

factor of 10, and thus the total emission current would be expected to increase by a factor of 100, which far outweighs the loss in emission due to reduced electrostatic field enhancement. Consequently, an increased density of emitter tips should be expected to allow increased emission current for a given cathode.

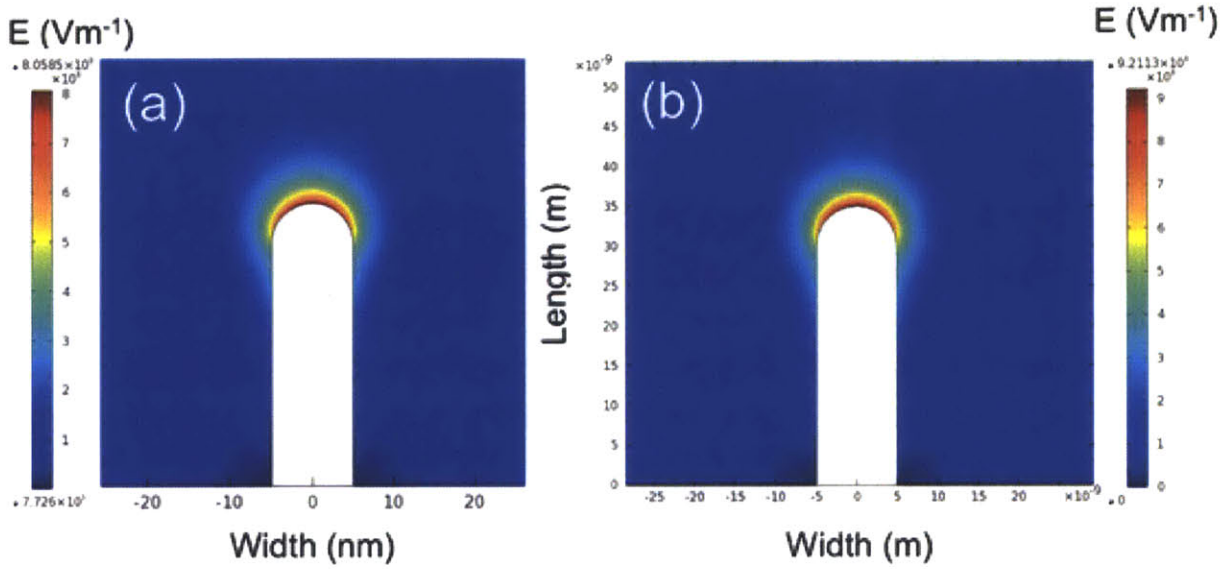

Fig. 3.19. Simulations of electrostatic field strength in the vicinity of a 10 nm diameter Au nanopillar with a height of 35 nm with an applied static field of 100 MV/m. (a) Nanopillar pitch of 100 nm results in a peak field enhancement factor of 8.1X at the nanopillar tip. (b) Nanopillar pitch of 1 μm results in a peak field enhancement factor of 9.2X at the nanopillar tip.

In the experiment, the applied DC field is below 1 MV/m. The enhanced DC field will be below 10 MV/m, which is much less than the GV/m scale optical field. Hence, the DC field is unlikely to perturb the photoelectron emission mechanism, except that it reduces the space charge effect and increases the emission current. On the other hand, the RF field in an RF cavity is on the order of tens of MV/m. The enhanced RF field can thus affect the emission mechanism, enhancing the probability of electron tunneling through the vacuum barrier.

3.7 Electromagnetic Heating of Optical Field Emitters

The effect of electromagnetic heating can be shown by investigating the temperature of the optical field emitters.

3.7.1 Heating of Au Nanopillars in Vacuum

We first studied the electromagnetic heating of Au nanopillars in vacuum. The Au nanopillar was modeled by a cylinder with a hemisphere cap on its top. The diameters of the nanopillars were fixed to 10 nm and the lengths of the nanopillars were swept to find the optimal geometry. Scattering boundary conditions were applied to the excitation and absorbing boundaries. The illumination light had a wavelength $\lambda = 800\,nm$ and was polarized along the axis of the nanopillar. Gold ($\epsilon = -24.9 + 1.57\mathrm{i}$) and vacuum ($\epsilon = 1$) were chosen as tip and dielectric materials, respectively. The thermal properties of Au were chosen as follows: thermal conductivity $k = 318\,W \cdot m^{-1} \cdot K^{-1}$, heat capacity $C_P = 129\,J \cdot kg^{-1} \cdot K^{-1}$, and density $\rho = 19300\,kg \cdot m^{-3}$. These properties are for Au at room temperature. The structure was meshed with tetrahedral-shaped elements with a 3 nm minimum dimension. The nanopillar was illuminated by a plane wave with 1 GV/m incident field strength. Here, we would like to point out final temperature of the tip depends on the incident intensity (or field strength) according to (2.4). 1 GV/m is on the same order of magnitude with the field strength of the laser used in the experiment. After heating with the incident optical wave for 100 fs, which is on the same order of magnitude with the laser pulse duration in the experiment, the temperatures of nanopillars with different lengths were investigated.

Fig. 3.20 shows simulated average temperatures of Au nanopillars with different lengths (L) as a function of time. It can be seen the 55 nm length nanopillar is subject to the strongest electromagnetic heating effect. This is expected as according to section (3.3.1), the nanopillar with this geometry exhibits LSPR at 800 nm and thus responds to the incident optical wave most strongly. The enhanced absorption cross section via LSPR leads to more deposited optical energy and higher final temperature. The resonant electromagnetic heating effect is also visualized in Fig. 3.21 where the final temperature distribution after heating is plotted for nanopillars with 45 nm (Fig. 3.21(a)), 55 nm (Fig. 3.21(b)) and 65 nm (Fig. 3.21(c)) lengths and the corresponding peak temperatures are 1500 K, 69114 K and 6533 K, respectively. In conclusion, LSPR can greatly enhance the electromagnetic heating of metallic nanoparticles and the final temperature of the on-resonance nanoparticle is much higher than the others. The simulated final temperature of the LSPR enhanced Au nanopillar is much higher than the Au melting temperature, suggesting the high power laser can damage the Au nanopillars even with short (e.g. 100 fs) heating time.

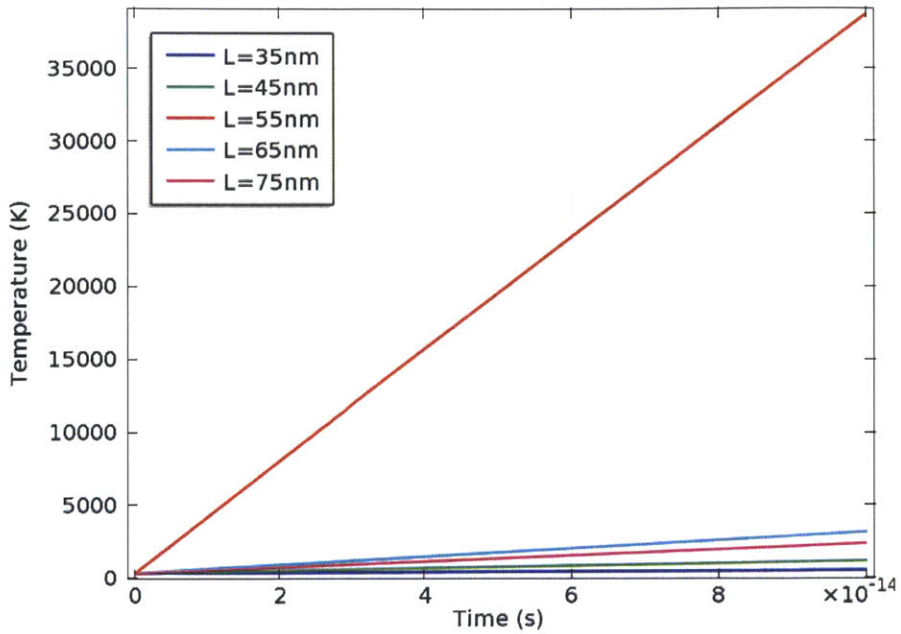

Fig. 3.20. Simulated average temperatures of Au nanopillars with different lengths (L) in vacuum heated by an 800 nm plane wave with 100 fs time duration and 1 GV/m incident field as a function of time. The 55 nm length nanopillar is subject to the strongest electromagnetic heating.

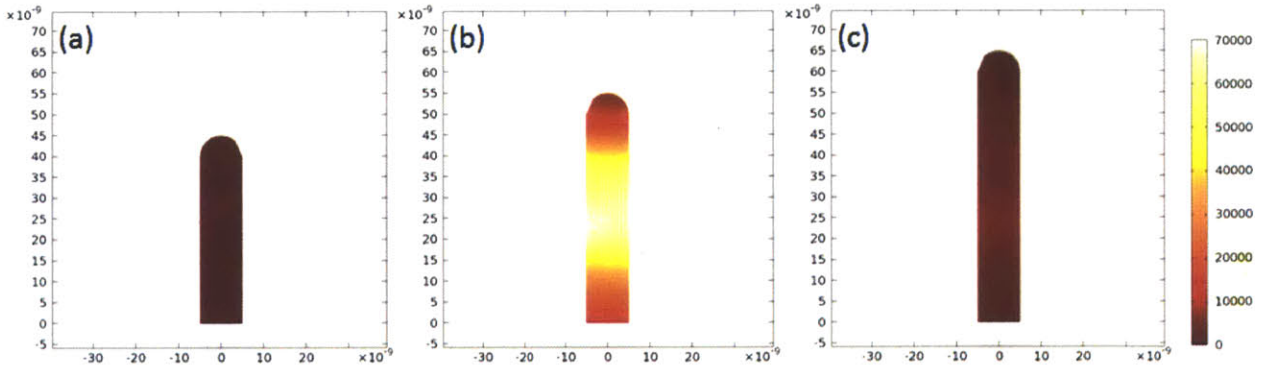

Fig. 3.21. Simulated temperature profiles of Au nanopillars in vacuum heated by an 800 nm plane wave with 100 fs time duration and 1 GV/m incident field. The nanopillar lengths are (a) 45 nm, (b) 55 nm, and (c) 65 nm. The color scale indicates local temperature in Kelvin (K). The corresponding peak temperatures are (a) 1500 K, (b) 69114 K and (c) 6533 K. The 55 nm length nanopillar (b) is subject to the strongest electromagnetic heating.

Note the temperature values presented here and in following sections are unphysical and can only be used for qualitative interpretation. We will discuss the

validity of the simulation and give a more reasonable estimation of the temperature in section 3.7.4.

3.7.2 Polarization Dependence of Electromagnetic Heating of Au Nanopillars

As suggested in [44], electromagnetic heating of Au nanorods (nanopillars) has a strong dependence on the polarization. For the same laser intensity, polarization along the long axis leads to a much higher post-heating temperature. This is due to the LSPR enhanced absorption cross section when the polarization is along the long axis and excites longitudinal plasmon resonance mode.

We modeled the LSPR enhanced Au nanopillar with 10 nm diameter and 55 nm length in vacuum. The model boundary conditions, material properties and FEM meshing were identical as the previous model. In this model, however, the electric field of incident light was polarized along or perpendicular to the long axis of the nanopillar. Fig. 3.22 shows the simulated average temperature of Au nanopillars with different polarizations of incident 800 nm plane wave with 35 fs time duration and 1 GV/m incident field as a function of time. The insets of Fig. 3.22 show temperature distributions at 35 fs for the two polarization states. As expected, polarization along the long axis results in much higher temperature rise (~3100 K), in drastic contrast to the negligible temperature rise of polarization perpendicular to the long axis.

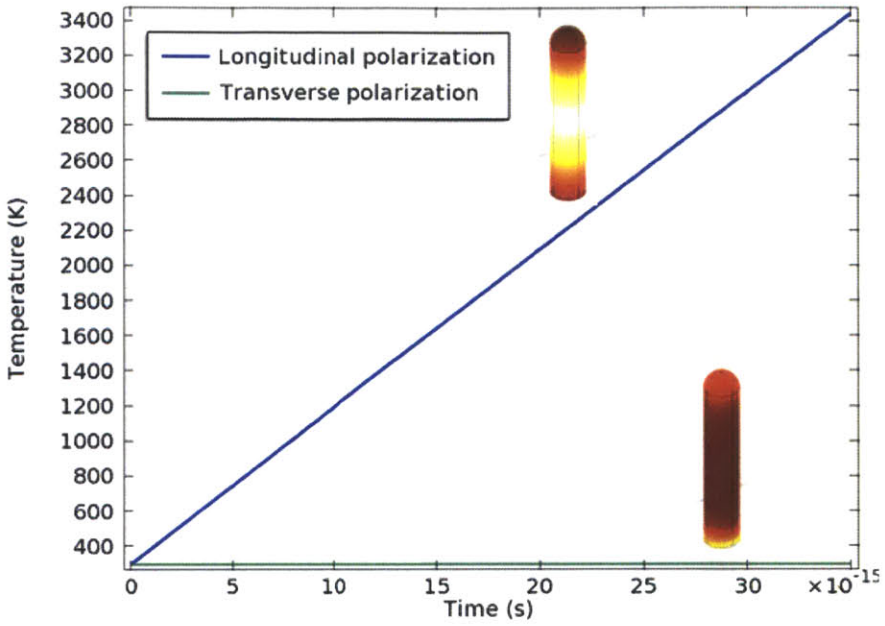

Fig. 3.22. Simulated average temperatures of Au nanopillars with different polarizations of incident 800 nm plane wave with 35 fs time duration and 1 GV/m incident field as a function of time. Blue: incident field is polarized along the long axis of the nanopillar. Green: incident field is polarized perpendicular to the along axis of the nanopillar. The insets show temperature distributions at 35 fs.

3.7.3 Heat Radiation from Au Nanopillars

It can be seen from previous sections that Au nanopillars are heated to very high temperatures by the high intensity incident laser. Therefore, the heat radiation from "hot" Au nanopillars, which is not considered in previous models, may have an effect on the temperature of the nanopillars.

We modeled the on-resonance Au nanopillar in vacuum with thermal radiation. The nanopillar was simply a cylinder with 10 nm diameter and 55 nm height, which is the optimal geometry of LSPR. The finite element meshing, electromagnetic excitation and material properties were identical to the model in section (3.7.1). Heat radiation from Au nanopillars was implemented via surface-to-ambient radiation (equation (2.99)). The ambient temperature was taken as the room temperature (293 K). The emissivity of Au varies from 0.02 to 0.4, depending on the surface morphology. To perform a systematic investigation of heat radiation from Au nanopillars, we ran a parametric sweep of the emissivity with values 0, 0.3, 0.6 and 0.9.

Fig. 3.23 shows the simulated average surface temperature of the Au nanopillar as a function of electromagnetic heating time. Results with the four different emissivity values are illustrated. For short heating time within 2 ps, the temperature of the Au nanopillar is below 2×10^5 K and the four curves coincide with each other, indicating the heat radiation takes a negligible effect. When the heating time is long, the Au nanopillar reaches high temperatures and the heat radiation assists cooling of the nanopillar and releases the heating effect. With heat radiation (non-zero emissivity), the temperatures of the Au nanopillar approach a constant value and do not further increase with heating time. This is because an increasing temperature leads to an increasing radiated power, and eventually the nanopillar reaches a temperature at which the radiation power is equal to the electromagnetic heating power so that the temperature will not further increase.

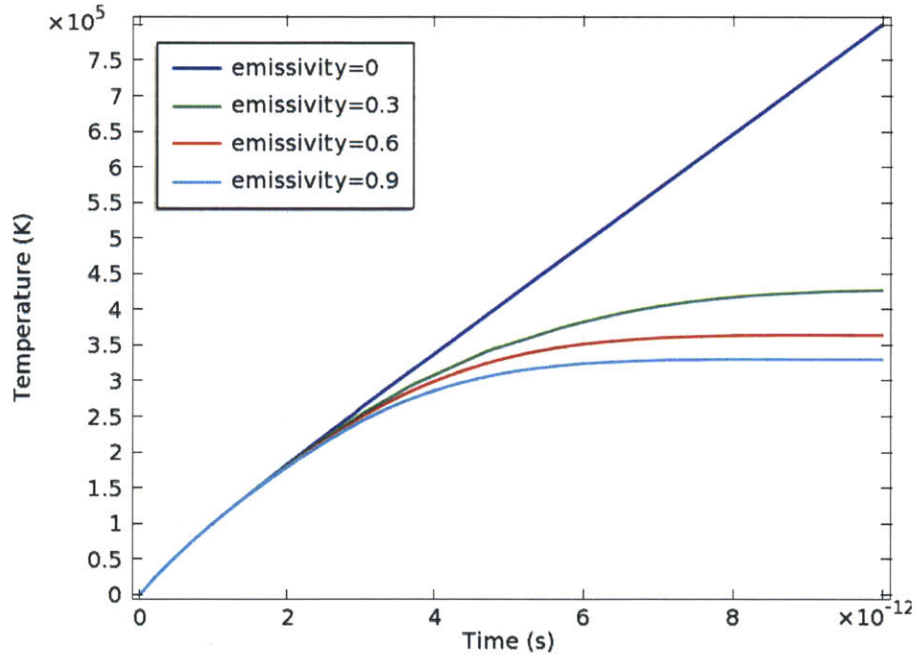

Fig. 3.23. Simulated Au nanopillar average surface temperature as a function of electromagnetic heating time. Heat radiation is considered and results with different emissivity values (0, 0.3, 0.6 and 0.9) are shown. For short heating time within 2 ps, the heat radiation takes a negligible effect. When the heating time is long, the Au nanopillar reaches high temperatures and the heat radiation assists cooling of the nanopillar and releases the heating effect. With heat radiation (non-zero emissivity), the temperatures of the Au nanopillar approach a constant value and do not further increase with heating time.

The final temperature can be determined analytically. According to surface-to-ambient radiation, equation (2.99), the radiation power is

$$P_{-} = \epsilon\sigma(T_{amb}^4 - T^4)S \tag{3.3}$$

Here, S is the surface area of the nanopillar. The electromagnetic heating power is simply the power absorbed by the nanopillar

$$P_{+} = \frac{\omega}{2}\epsilon''|E|^2 V \tag{3.4}$$

where ω is the electromagnetic angular frequency, ϵ'' is the imaginary part of the dielectric permittivity of Au, $|E|$ is the incident amplitude of the electromagnetic wave (1 GV/m in the model) and V is the volume of the nanopillar. The final temperature of the nanopillar will be reached if the radiation power equals the heating power

$$P_{-} = P_{+} \tag{3.5}$$

Solving equations (3.3), (3.4) and (3.5) with the parameters used in the model, the final temperature is

$$T_f = 4 \times 10^5\ K \tag{3.6}$$

This value is consistent with Fig. 3.23, showing agreement between numerical simulation and analytical calculation.

To summarize, the heat radiation will not take a significant effect until the temperature is very high (on the order of 10^5 K). Given that this temperature is far above the melting temperature of Au (and practically any material), the heat radiation can be safely neglected in the analysis of electromagnetic heating of our optical field emitters.

3.7.4 Electromagnetic Heating of Fabricated Au Optical Field Emitter

As discussed in section 3.4, fabricated Au optical field emitter has a different geometry from a perfect cylinder and is in a complex dielectric environment, which cause different electromagnetic power deposition and heat transfer. Hence, we simulated the electromagnetic heating of fabricated Au optical field emitter with dimensions taken from Fig. 3.8. The emitter geometry, materials and their electromagnetic properties, FEM meshing and electromagnetic excitation were discussed in section 3.4.1. The thermal properties of Au were chosen as: thermal

conductivity $k = 318\,W \cdot m^{-1} \cdot K^{-1}$, heat capacity $C_P = 129\,J \cdot kg^{-1} \cdot K^{-1}$, and density $\rho = 19300\,kg \cdot m^{-3}$. The thermal properties of Ti were chosen as: thermal conductivity $k = 21.9\,W \cdot m^{-1} \cdot K^{-1}$, heat capacity $C_P = 523\,J \cdot kg^{-1} \cdot K^{-1}$, and density $\rho = 4506\,kg \cdot m^{-3}$. The thermal properties of SiO_2 were chosen as: thermal conductivity $k = 1.46\,W \cdot m^{-1} \cdot K^{-1}$, heat capacity $C_P = 703\,J \cdot kg^{-1} \cdot K^{-1}$, and density $\rho = 2648\,kg \cdot m^{-3}$. The thermal properties of Si were chosen as: thermal conductivity $k = 149\,W \cdot m^{-1} \cdot K^{-1}$, heat capacity $C_P = 710\,J \cdot kg^{-1} \cdot K^{-1}$, and density $\rho = 2329\,kg \cdot m^{-3}$. Again, these properties are values for room temperature. The initial temperature was set to 293 K and the structure was illuminated by 800 nm plane wave with 1 GV/m electric field magnitude. After 35 fs heating, the light source was turned off and heat was dissipated through the backside of the Si substrate which was set to room temperature.

Fig. 3.24 shows the simulated emitter temperature as a function of time. Fig. 3.24(a) shows the peak temperature of the emitter, which reaches 4500 K after electromagnetic heating. However, for the average temperature of the emitter, the peak value is only about 500 K after electromagnetic heating as shown in Fig. 3.24(b). After heating by a 35 fs short optical pulse, the temperature of the emitter falls back to room temperature within tens of femtoseconds. Given that the repetition rate of the femtosecond laser pulse is only a few kHz in the experiment, there is no accumulation of residual heat from previous pulses. We also adopted simple calculation based on equation (2.101) to roughly estimate the temperature rise. The absorbed power was calculated by integrating the electromagnetic power dissipation density within the emitter and gave a result of $P_{abs} = 0.0606\,W$. This produced a temperature rise of 149 K and a final temperature of 442 K, agreeing with the numerical calculation in Fig. 3.24(b) reasonably well.

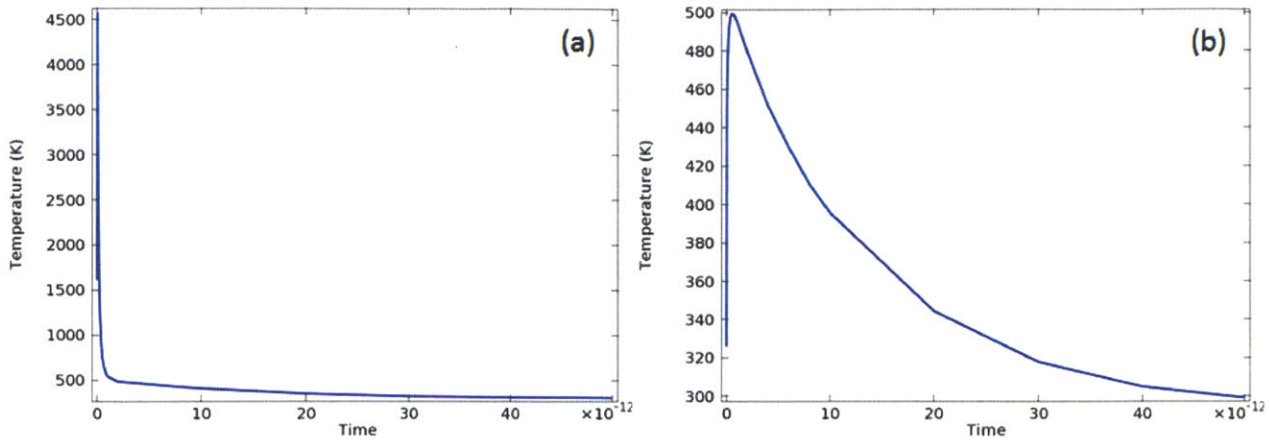

Fig. 3.24. Simulation of electromagnetic heating of fabricated Au optical field emitter. The emitter is illuminated by 800 nm plane wave with 1 GV/m electric field magnitude for 35 fs. Then, the light source is turned off. (a) Peak temperature as a function of time. (b) Average temperature as a function of time.

There are two paths for cooling of the electromagnetically heated emitter, radiative cooling via radiation of photons, and conductive cooling via heat transfer through the substrate. In order to compare the role of the two paths, we re-ran the simulation with varying surface emissivity for heat radiation and re-plotted Fig. 3.24(b). The result is shown in Fig. 3.25. Different surface emissivity values correspond to different thermal radiation abilities of the emitter, with 0 for no thermal radiation (hence no radiative cooling) and 1 for strongest thermal radiation (hence strongest radiative cooling). From Fig. 3.25, the different thermal radiation abilities make very little difference in the cooling process of the emitter. Therefore, the cooling of the emitter is primarily through the heat conduction via the substrate. Choosing a good heat conductor, such as sapphire, for the substrate can improve the heat dissipation into the substrate and reduce the probability of damaging the emitter.

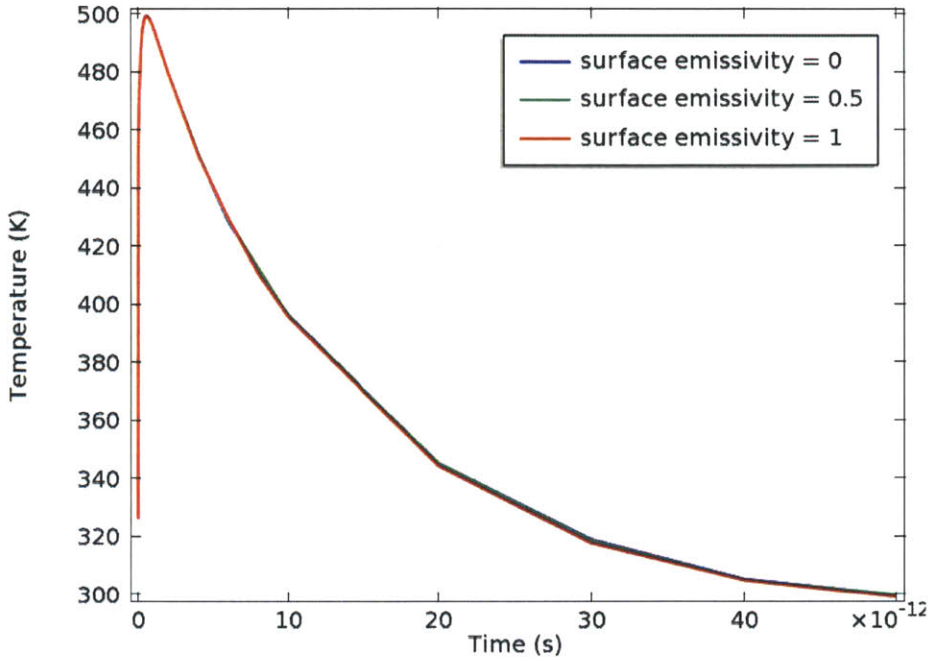

Fig. 3.25. Simulation of the average temperature of the emitter as a function of time with varying surface emissivity values: 0, 0.5 and 1. The emitter is illuminated by 800 nm plane wave with 1 GV/m electric field magnitude for 35 fs.

In the previous laser heating simulations, the backside of the Si substrate was set to room temperature. This specific boundary condition should be cautiously verified, because the Si substrate in the model was only 100 nm thick and it was unclear whether the temperature was room temperature at that distance away from the heat source, the electromagnetically heated optical field emitter. A simple estimation of the temperature rise at a certain distance away from the emitter was made based on equation (2.102) and equation (2.103) and the result is shown in Fig. 3.26. The absorbed electromagnetic power was 0.0606 W as was calculated and the thermal conductivity of the substrate/vacuum interface was calculated from the effective thermal conductivity model discussed in section (2.4.1). At 100 nm away from the emitter, the temperature rise was below 10 K, suggesting it was a good approximation in the model to assume the backside of the Si substrate remained at room temperature.

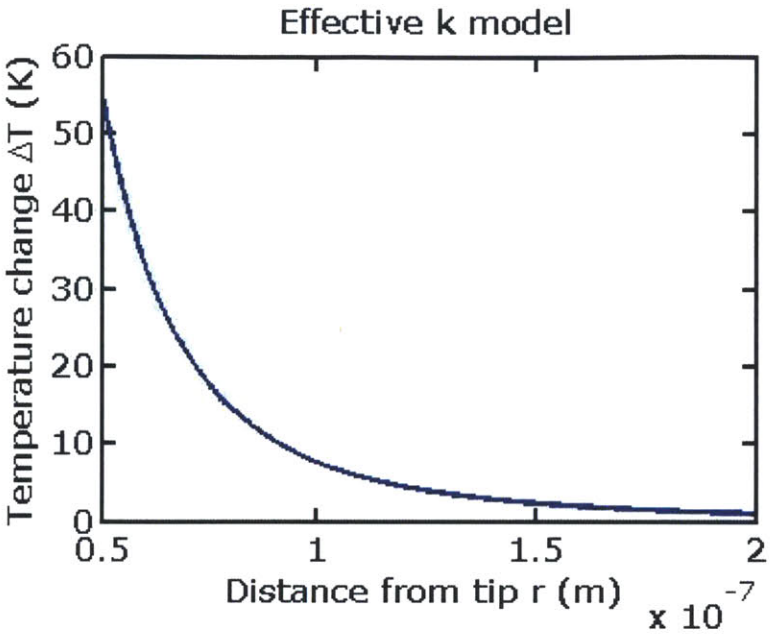

Fig. 3.26. Estimated temperature rise at a certain distance away from the emitter according to equation (2.102) and equation (2.103).

It is also interesting to investigate the temperature profile, shown in Fig. 3.27(a) of the fabricated emitter after heated by a femtosecond laser pulse. The Ti adhesion layer has a much higher temperature compared with the Au and accounts for most of the heating of the emitter. This can be explained by the optical field enhancement profile within the emitter shown in Fig. 3.27(b). The local field strength at the Ti layer is relatively strong. The strong field and heating effect are caused by substrate coupling effect on LSPR and LSPR damping via the Ti adhesion layer of lithographically defined metal nanoparticle, which we will discuss in more details in Chapter 4.

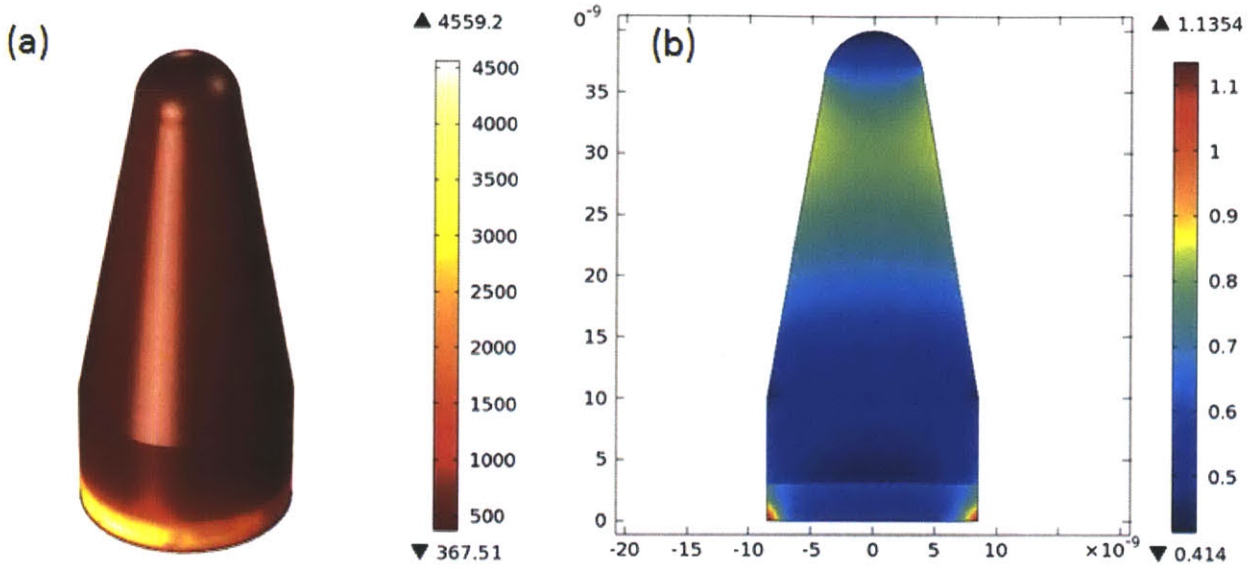

Fig. 3.27. (a) Temperature profile of the fabricated Au optical field emitter heated by a 35 fs laser pulse. (b) Optical field enhancement within the emitter.

It has to be noted here that the high temperature above several thousands of Kelvins simulated in this and previous sections are of course impractical. It may also be inaccurate since the simple electromagnetic heating model in COMSOL based on equation (2.98) does not take into account the details of ultrafast laser excitation discussed in section (2.4.2). The simple estimation developed in section (2.4.1) should be sufficient to get a general idea of the approximated temperature rise of the emitter after a femtosecond laser pulse heating and determine whether the emitter is damaged by referring to the material melting temperature and the typical reshaping temperature of the nanoparticles. To further understand the heating process and justify that the seemingly high temperature does not severely damage the optical field emitters, we calculated the electron temperature based on the discussion in section (2.4.3). The γ parameter we used was $3.47\ mJ/(kg \cdot K^2)$, within the range of theoretically and experimentally reported values for Au in literature, $3.26 - 3.70\ mJ/(kg \cdot K^2)$. The calculated final temperature from equation (2.106) with other quantities mentioned in this section is 3342 K. This value of electron temperature is relatively low compared with reported values in literature, indicating our optical field emitter will not be completely evaporated or ablated by the incident laser pulse. The reshaping of metal nanoparticles at temperatures lower than the melting point [51][52] and the alloying of metal nanoparticles with the substrate [62] remain as potential damage issues. To

guarantee a long lifetime of the nanostructured photocathode, intensity of the driving laser should be below the damage threshold.

3.7.5 Heating of Si Tips

We also modeled the electromagnetic heating of Si tips. The model geometry and meshing of Si tips were discussed in section 3.5.1. We studied the heating effect for a Si tip with 10 nm radius of curvature. We used refractive indices for the optical properties of materials, and $n = 3.69 + 6.5 \times 10^{-3}\mathrm{i}$ for Si while $n = 1$ for vacuum. As for thermal properties of Si, we used $k = 149\, W \cdot m^{-1} \cdot K^{-1}$ as the thermal conductivity, $C_P = 710\, J \cdot kg^{-1} \cdot K^{-1}$ as the heat capacity, and $\rho = 2329\, kg \cdot m^{-3}$ as the density. Initial temperature $T(t = 0)$ was set to room temperature, 293 K. These thermal properties are for Si at room temperature, as we are assuming the electromagnetic heating of Si is not significant and the temperature rise is minor so that thermal properties will not deviate too much from its values at room temperature. We will see later that this assumption is valid. The tip was illuminated by a plane wave with 1 GV/m incident field strength, similar to the models in section 3.5.1. Here, we would like to point out final temperature of the tip depends on the incident intensity (or field strength) according to (2.98). 1 GV/m is on the same order of magnitude with the field strength of the laser used in the experiment. After heating with the incident optical wave for 100 fs, which is on the same order of magnitude with the laser pulse duration in the experiment, the temperature profile of the tip was investigated and shown in Fig. 3.28. The highest temperature is observed at the tip apex where the field is strongest. After 100 fs heating, the highest final temperature $T(t = 100fs)$ is about 320 K, corresponding to a temperature rise of 27°. This minor temperature increase of the tip structure indicates the validity of using Si thermal properties at room temperature in the simulation. This temperature rise is relatively small because the refractive index of Si has a small imaginary part so that Si only absorbs a small amount of the incident electromagnetic energy. Also, the final temperature is well below the melting temperature of Si, so we can safely conclude that the Si tips will not be damaged by the incident laser pulse.

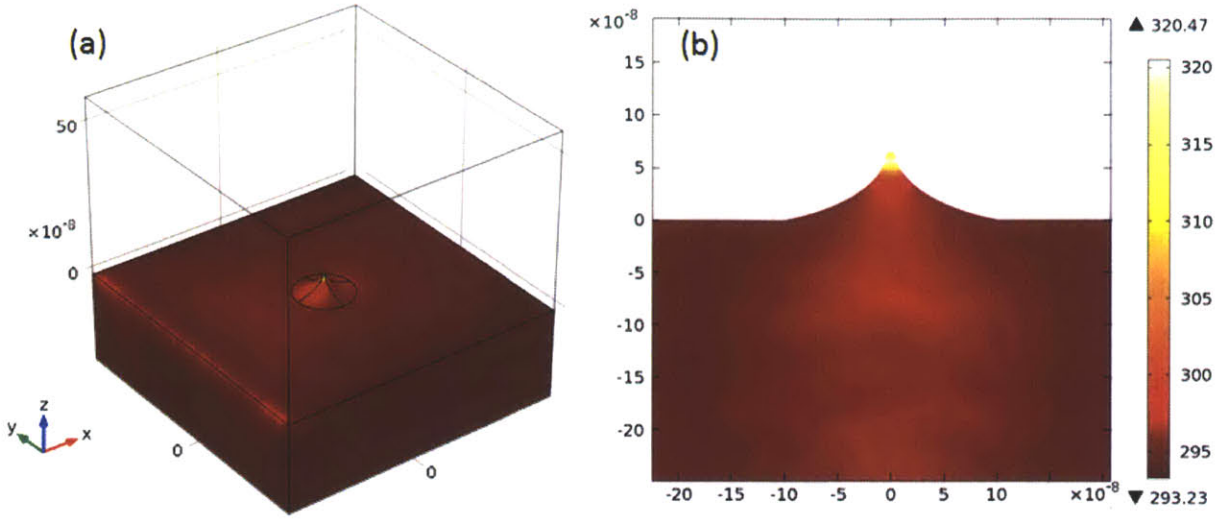

Fig. 3.28. Simulated temperature profile of the Si tip heated by incident plane wave with 1 GV/m electric field amplitude for 100 fs. The incident plane wave propagates in x-direction and polarized in z-direction to give a stronger field enhancement. The color scale indicates the temperature in Kelvin. (a) Temperature profile on the surface of the Si tip and substrate. (b) Temperature profile in the cut-plane across the center axis of the tip.

Chapter 4: Modeling of In-Plane Gold Nanostructures

The vertically standing optical field emitters require a polarization perpendicular to the substrate surface in order to achieve a strong field enhancement. Thus, a grazing incident light is required. However, normal incidence, where the optical wave propagates in the direction perpendicular to the substrate and polarized in the plane parallel to the substrate surface, is more commonly used in photocathode experiments. The final setup of the emittance exchange ICS X-ray sources also requires normal incidence as opening a transparent port on the sidewall of the RF cavity chamber can degrade the system performance. Thus, we pursued the design of in-plane plasmonic nanostructures excitable with normally incident light as optical field emitters. Besides the compatibility with most photocathode testing facilities and the setup of emittance exchange ICS X-ray source chamber, the in-plane nanostructures also have all their key dimensions in the substrate plane so that they provide more design flexibility and are friendlier to the standard planar micro-/nano-fabrication techniques.

Optical field enhancement by localized surface plasmon resonance of in-plane metallic nanoparticles has been intensively investigated. Kim *et al.* used gold bow-tie structures to enhance near-infrared optical field [63]. The strong field was used to ionize noble gas atoms and generated high-harmonics up to extreme ultraviolet spectral range. Novotny *et al.* showed the near-field enhancement by surface plasmon resonance can be utilized in the metal-based optical antennas [64]. The application of metallic nanoparticles as optical antennas shows their ability of coupling free space optical wave to subwavelength structures.

In this chapter, we will propose in-plane plasmonic nanostructures as the optical field emitters with normally incident excitation laser.

4.1 Single Gold Nanorod

We started by modeling a single Au nanorod in vacuum or on a substrate. The model setup and FEM meshing are shown in Fig. 4.1. The calculation domain was encapsulated in a spherical perfectly matched layer (PML) that absorbed all outgoing electromagnetic waves. The single Au nanorod was placed in vacuum or on a substrate. The length, width and thickness of the nanorod were 50 nm, 15 nm, and 10 nm, respectively. All sharp edges of the nanorod were rounded. Objects

within the calculation domain were adaptively meshed with free tetrahedral elements and the PML was sweeping-meshed. The minimum element size was kept small enough so that each edge of the nanorod contained at least tens of elements. The illumination light was in normal incidence, namely, the optical wave propagates in the z-direction.

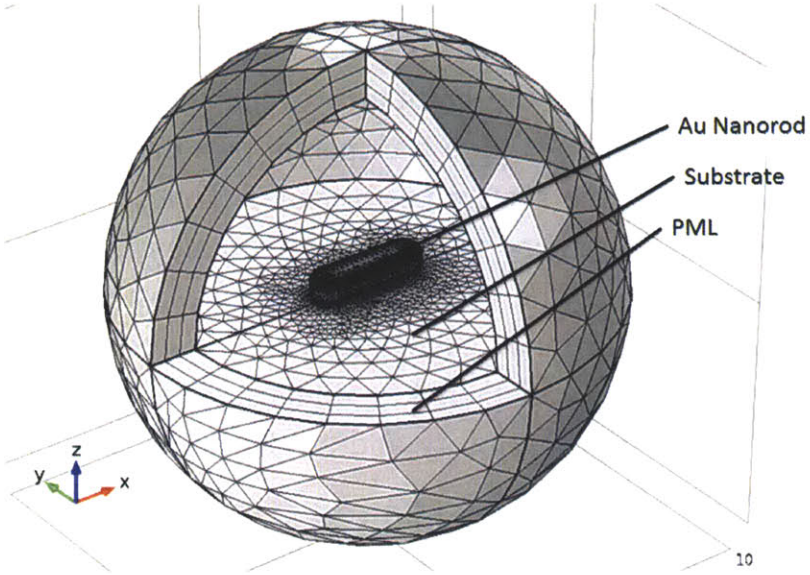

Fig. 4.1. Model setup and FEM meshing for simulating a single Au nanorod in vacuum or on a substrate.

4.1.1 Single Gold Nanorod in Vacuum

We simulated the optical response of a single Au nanorod in vacuum under a plane wave illumination with wavelength ranging from 400 nm to 1000 nm. We considered both longitudinal polarization, where the optical electric field was polarized along the long axis of the nanorod, and transverse polarization, where the optical electric field was polarized perpendicular to the long axis of the nanorod. The optical excitation in the model was implemented via the scattered field formalism. The dielectric permittivity of Au was taken from Johnson & Christy [58] and the permittivity of vacuum was kept as $\epsilon(Vacuum) = 1$.

The simulated normalized optical power absorption spectra and average field enhancement spectra are shown in Fig. 4.2. The absorption was calculated by integrating the electromagnetic power dissipation in the Au nanorod. The average field enhancement was calculated by averaging the local field enhancement over the surface of one end cap of the nanorod according to equation (3.2). The LSPR

peak can be seen for both longitudinal and transverse polarizations. The longitudinal polarization excited the longitudinal LSPR mode of the nanorod at around 660 nm wavelength. The transverse polarization excited the transverse LSPR mode of the nanorod at around 530 nm. The longitudinal mode was much stronger than the transverse mode, indicating it was preferred to polarize the incident field along the long axis of the nanorod in order to get stronger absorption or field enhancement. All these results agree well with literature.

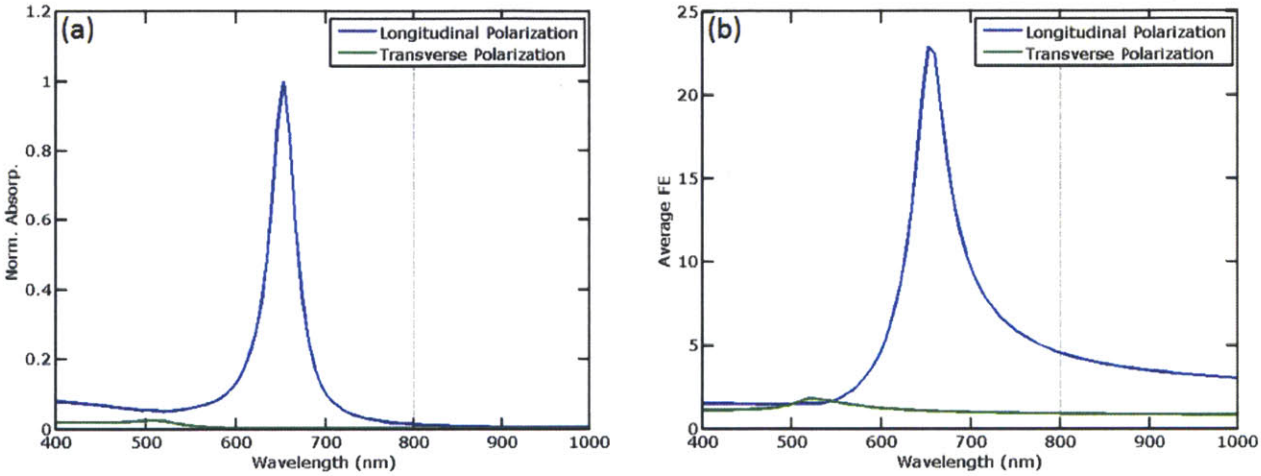

Fig. 4.2. Simulated normalized optical power absorption spectra and field enhancement spectra for a single Au nanorod in vacuum. Both longitudinal and transverse polarizations are considered. The dotted line indicates target operating wavelength, 800 nm, in the experiment.

4.1.2 Single Gold Nanorod on Dielectric Substrate

We simulated the optical response of a single Au nanorod on a dielectric substrate under a plane wave illumination with wavelength ranging from 400 nm to 1000 nm. We considered two different substrates with refractive index $n_s = 1.5$ and $n_s = 3.5$. The optical excitation in the model was implemented via scattered field formalism with analytically calculated reflection and transmission coefficient at normal incidence. Incident optical field was polarized along the long axis of the nanorod. The dielectric permittivity of Au was taken from Johnson & Christy [58] and the permittivities of vacuum and dielectric substrate are assumed to be wavelength-independent.

The simulated normalized optical power absorption spectra and average field enhancement spectra are shown in Fig. 4.3. The absorption and average field

enhancement were evaluated in the same way adopted in the previous section. Compared with the simulation in the previous section, it can be concluded that the existence of a substrate has the following effects on LSPR of nanoparticles. First, the substrate redshifts the LSPR peak position in the spectrum. The higher refractive index the substrate has, the stronger the redshift is. Second, the LSPR peak intensity is lowered and the width (FWHM) is broadened. Again, this effect increases with increasing substrate refractive index. The above two effects are frequently discussed in the literature and the sensitivity of plasmonic nanoparticles to the change of dielectric environment enables their application as sensors. Finally, recall the incident field is polarized so that only longitudinal LSPR mode can be excited, but Fig. 4.3 shows two LSPR modes are excited simultaneously, especially when the substrate index is 3.5. This is due to substrate-mediated LSPR mode coupling.

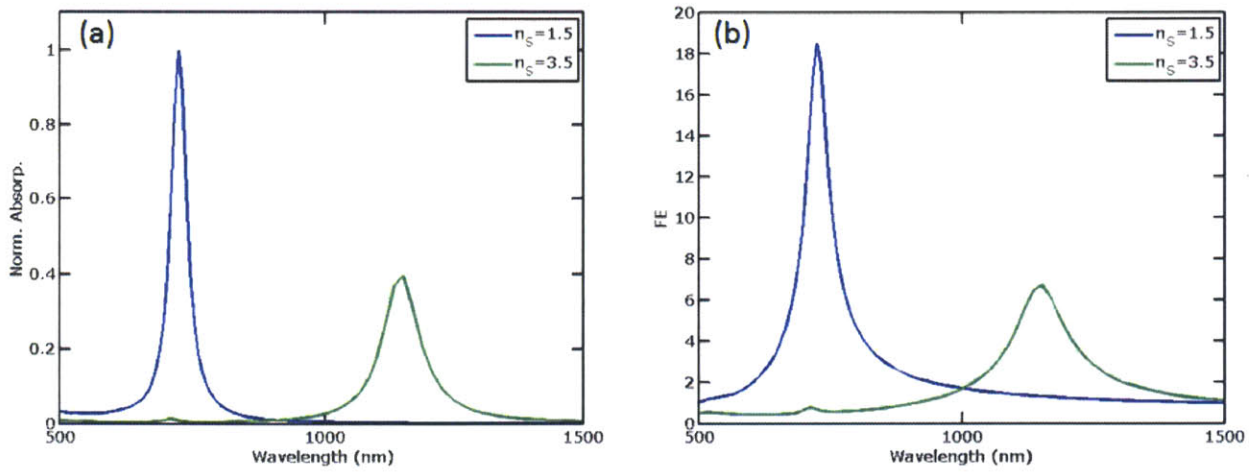

Fig. 4.3. Simulated normalized optical power absorption spectra and field enhancement spectra for a single Au nanorod on two different substrates with refractive index $n_s = 1.5$ and $n_s = 3.5$.

We also plotted the optical near-field enhancement profile for Au nanorods on the two substrates at their LSPR peaks in Fig. 4.4. In the case of substrate (B) it can be seen that the region of highest enhancement of the applied optical field is at the nanorod/substrate interface. Shifting the region of highest field enhancement to the Au/vacuum interface is desirable for more efficient electron emission from arrays of such Au nanorods. Fig. 4.4(A) shows that this may be achieved by placing

nanorods on a substrate with a lower refractive index. It is also clear that an Au nanorod on a low refractive index substrate exhibits stronger LSPR.

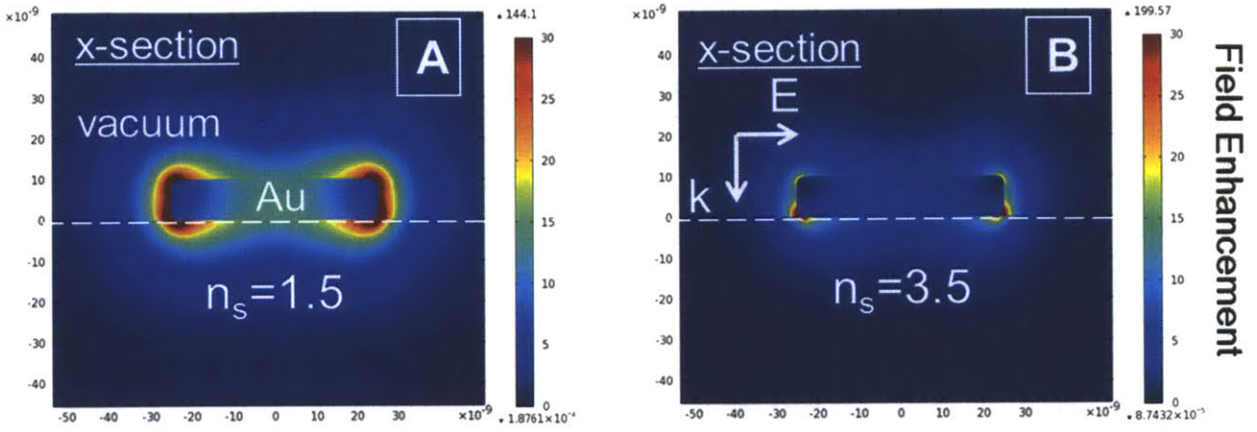

Fig. 4.4. Optical near-field enhancement profile for Au nanorods with 15 nm width, 50 nm length and 10 nm thickness on two different substrates with refractive index (A) $n_s = 1.5$ and (B) $n_s = 3.5$. The cross section is perpendicular to the substrate and along the long axis of the nanorod. Incident plane wave propagation direction **k** and polarization direction **E** are shown. The white dashed line indicates the surface of the substrate.

4.2 Substrate Effect on Gold Nanorod Plasmon Resonance

When metallic nanoparticles are placed on a substrate, the dielectric environment will be changed and the symmetry will be broken, both having an effect on the LSPR of the nanoparticles. Sherry *et al.* experimentally observed and theoretically verified that the LSPR mode of a single silver nanocube was split into two modes when placed on a glass substrate [65]. The near-field profiles of the two modes were very different, with one showing hot spots at the upper surface of the nanocube while the other showing hot spots at the lower surface, the Ag/glass interface. Knight *et al.* showed that the effect of dielectric substrate on LSPR was polarization dependent [66]. When the incident light was polarized such that dipole LSPR modes with different orientations could be excited, the image charge associated with the substrate lifted the degeneracy of the dipole modes and split the LSPR peaks in the scattering spectra. Zhu *et al.* studied the effect of a Si substrate on the Au nanoparticle LSPR [67]. The plasmon resonance of Au nanoparticles was split into two modes by the image charge effect of the Si substrate. Zhang *et al.* theoretically studied the substrate induced LSPR modes hybridization of a silver

nanocube [68]. Symmetry-breaking introduced by the substrate was shown to couple and hybridize the bright dipole mode and the dark quadruple mode of the nanoparticle. Chen *et al.* studied the effect of dielectric properties of substrates on the far-field scattering pattern of gold nanorods [69]. The scattering patterns of nanorods on high refractive index substrate showed unusual donut shape due to the substrate mediated enhancement of the transverse LSPR mode of the nanorods. Mahmoud *et al.* showed the effect of dielectric substrate on the LSPR of silver nanocubes [70]. The degenerate LSPR modes of the highly symmetrical nanocubes were split by the existence of a substrate and different modes had very different near-field distributions. Hutter *et al.* investigated the interactions of metallic nanoparticles with different dielectric substrates [71]. Substrates with higher refractive index were shown to induce stronger optical power localization between the nanoparticles and the substrates.

The simulation results in previous sections already illustrated the substrate effect on LSPR. Here we will report a systematic investigation of the substrate effect and highlight the influence of substrate refractive index and distance between nanoparticle and substrate. We used the model for a single Au nanorod on a substrate discussed in section 4.1.2. Besides choosing two different substrates with refractive index $n_s = 1.5$ and $n_s = 3.5$, we also placed the Au nanorod at a distance above the substrate. The gap between the nanorod and the substrate was set at 1 nm, 3 nm and 5 nm. The normalized optical power absorption spectra are shown in Fig. 4.5 to indicate the LSPR peak.

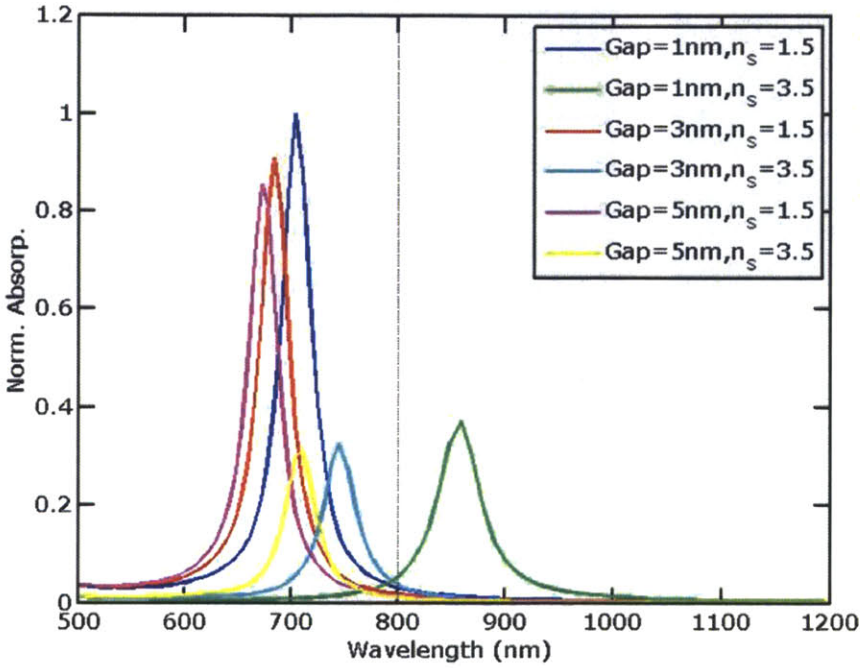

Fig. 4.5. Simulated normalized optical power absorption spectra for a single Au nanorod on two different substrates with refractive index $n_s = 1.5$ and $n_s = 3.5$ with 1 nm, 3 nm and 5 nm gap from the substrate.

As mentioned, the substrates redshift, lower, and broaden the LSPR peak. This effect increases with increasing substrate refractive index and decreasing gap between the nanoparticle and the substrate. Fig. 4.6 shows the optical near-field for Au nanorods with different gap distances from the substrate. It can be seen the strongest near-field is localized at the gap and this localization effect becomes stronger with smaller gap distance. Thus, when the gap distance becomes zero, namely the nanorod is directly placed on the substrate, strongest near-field should be at the nanorod/substrate interface, as illustrated previously in Fig. 4.6.

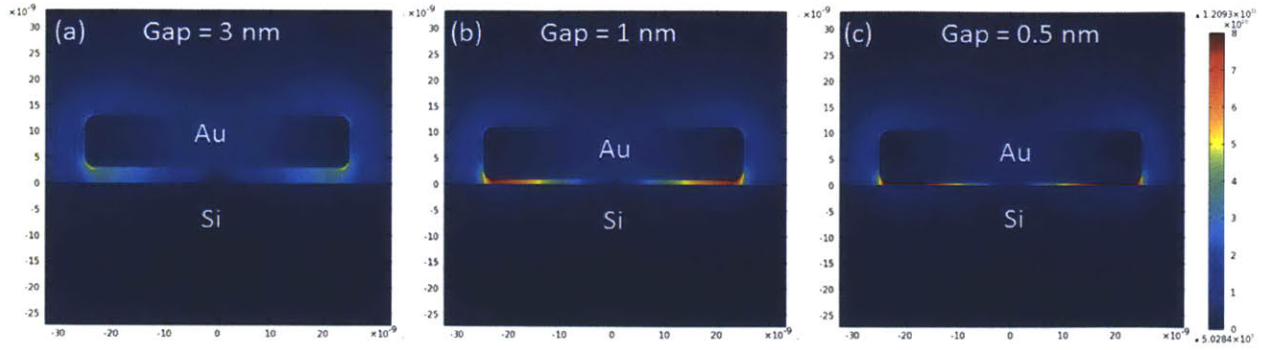

Fig. 4.6. Optical near-field profile for Au nanorods with 15 nm width, 50 nm length and 10 nm thickness on $n_s = 3.5$ substrates with (a) 3 nm, (b) 1 nm, and (c) 0.5 nm gap from the substrate. The near-field localization effect becomes stronger with smaller gap distance.

4.3 Gold Nanorod Array on Silicon Substrate

We also modeled Au nanorod array on Si substrate. The model setup and FEM meshing are shown in Fig. 4.7. Calculation domain was a unit cell of the array. Periodic boundary conditions were applied to the sidewalls of the unit cell in order to simulate a square array. The Au nanorod was placed on Si substrate. PML was under the substrate to absorb outgoing waves. The length, width and thickness of the nanorod were 50 nm, 15 nm and 10 nm, respectively. All sharp edges of the nanorod were rounded. Objects within the calculation domain were adaptively meshed with free tetrahedral elements and the PML was sweeping meshed. The minimum element size was kept small enough so that each edge of the nanorod contained at least tens of elements. The illumination light was in normal incidence, namely, the optical wave propagates in z-direction.

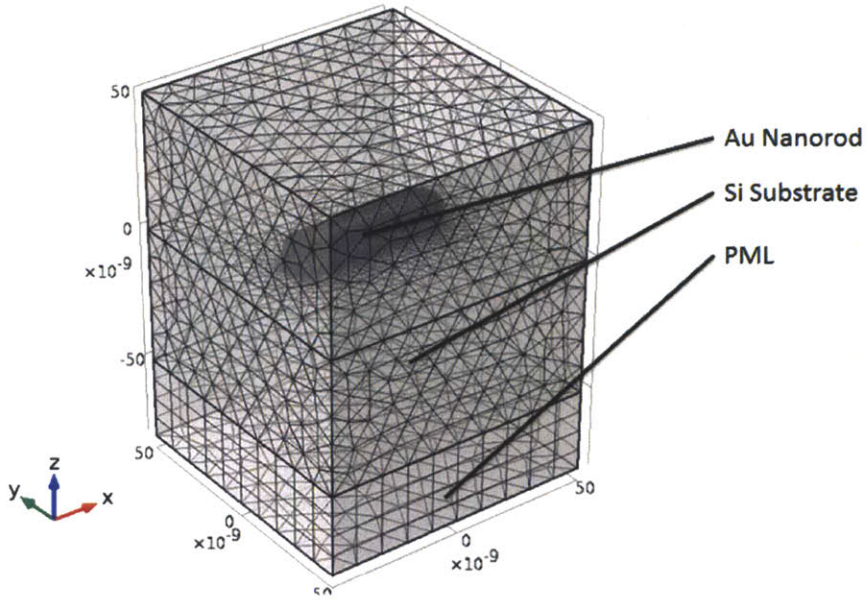

Fig. 4.7. Model setup and FEM meshing for simulating Au nanorod array on Si substrate.

4.3.1 Geometry Optimization

The LSPR is known to depend on the nanoparticle geometry. Specifically, the LSPR peak will redshift in the spectrum with increasing aspect-ratio of the nanorod. We simulated the optical response of Au nanorod arrays on Si substrate with different aspect-ratios under a plane wave illumination with wavelength ranging from 500 nm to 1500 nm. The width and thickness of Au nanorod were fixed at 15 nm and 10 nm, while its length was varied from 21 nm to 35 nm. Incident optical field was polarized along the long axis of the nanorod. The dielectric permittivity of Au was taken from Johnson & Christy [58] and the dielectric permittivity of Si was taken from Palik [59].

The simulated normalized optical power absorption spectra and average field enhancement spectra are shown in Fig. 4.8. The absorption and average field enhancement were evaluated in the same way adopted in previous sections. The optimal length of the Au nanorod (with 15 nm width and 10 nm thickness) that provides the strongest optical response (optical power absorption and field enhancement) to 800 nm excitation light is 22-23 nm. Also, with increasing nanorod length, the LSPR peak position redshifts and peak intensity increases, agreeing with theoretical and experimental results in literature.

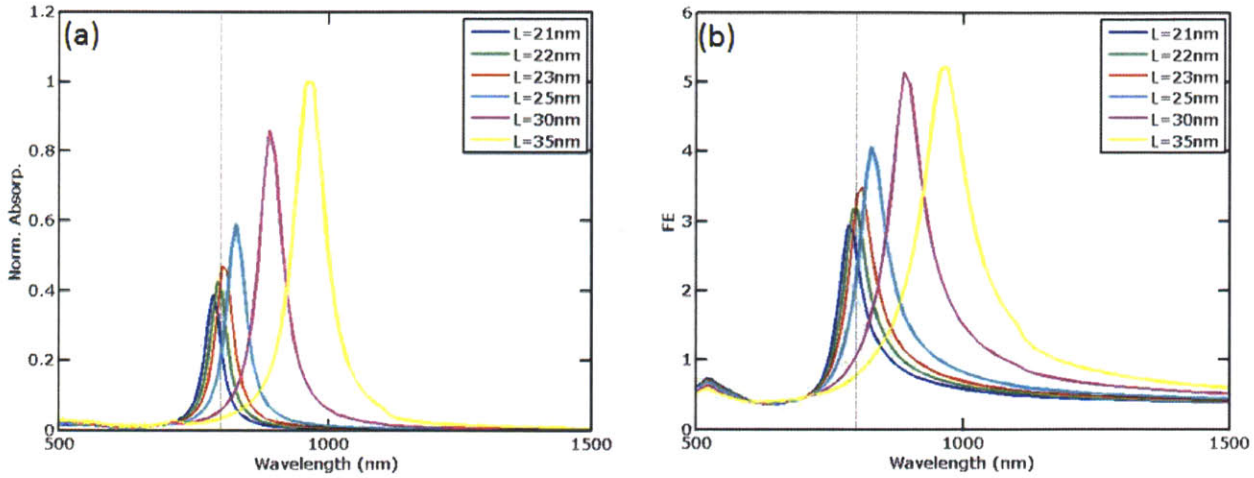

Fig. 4.8. Simulated normalized optical power absorption spectra and average field enhancement spectra for Au nanorod arrays on Si substrate with various aspect-ratios. The width and thickness of Au nanorod were fixed at 15 nm and 10 nm, while its length was varied from 21 nm to 35 nm. The dotted line indicates target operating wavelength, 800 nm, in the experiment.

4.3.2 Optical Near-field Profile

For the optimal Au nanorod geometry with 15 nm width, 22 nm length and 10 nm thickness, we plotted the optical near-field enhancement profile for 800 nm illuminating light in Fig. 4.9. Fig. 4.9(a) shows the cross section parallel to the substrate (x-y cut-plane). As expected, the strongest near-field is located at the two poles of the nanorod, corresponding to dipole LSPR mode. Fig. 4.9(b) shows the cross section perpendicular to the substrate and parallel to the nanorod long axis (x-z cut-plane). It is clear that the substrate breaks the symmetry of the optical near-field profile. The strongest field enhancement is located at the interface between the Au nanorod and the Si substrate, similar to Fig.4.6.

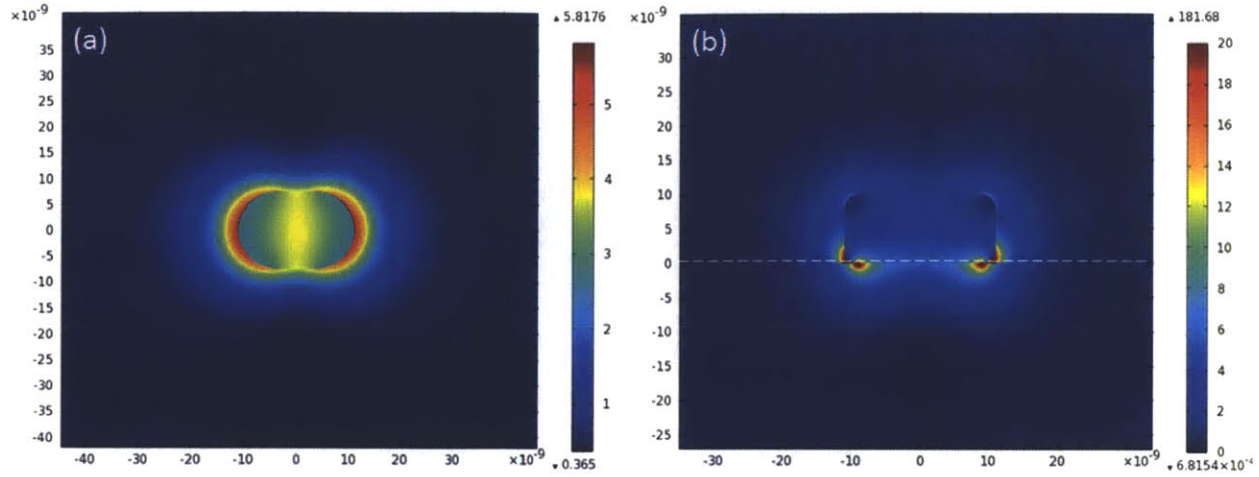

Fig. 4.9. Optical near-field enhancement profile for the optimal Au nanorod geometry with 15 nm width, 22 nm length and 10 nm thickness. (a) Cross section parallel to the substrate (x-y cut-plane); and (b) cross section perpendicular to the substrate and parallel to the nanorod long axis (x-z cut-plane). The white dashed line indicates the surface of the substrate.

4.4 Fabricated Gold Nanorod Optical Field Emitter Arrays

As discussed in section 3.4, the device architecture of fabricated Au nanostructures is slightly different from those in vacuum or directly placed on a substrate. Thus, we ran optical modeling for the exact structure of the fabricated Au nanorod optical field emitter arrays. Specifically, a 10 nm SiO_2 thin film was added to mask electron emission from the substrate and a 3 nm Ti layer was added between the Au nanorod and the substrate to promote adhesion. The model schematic is illustrated in Fig. 4.10. A SEM image of fabricated Au nanorod arrays on ITO substrate is shown in Fig. 4.11.

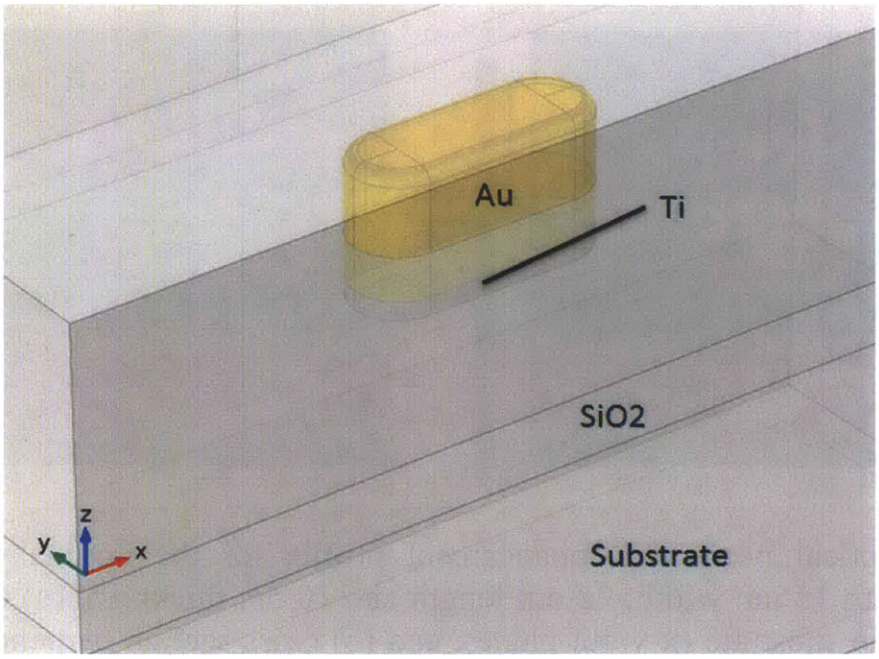

Fig. 4.10. Model schematic of fabricated Au nanorod optical field emitter arrays. A 10 nm SiO_2 thin film is used to mask electron emission from the substrate and a 3 nm Ti layer between the Au nanorod and the substrate is used to promote adhesion.

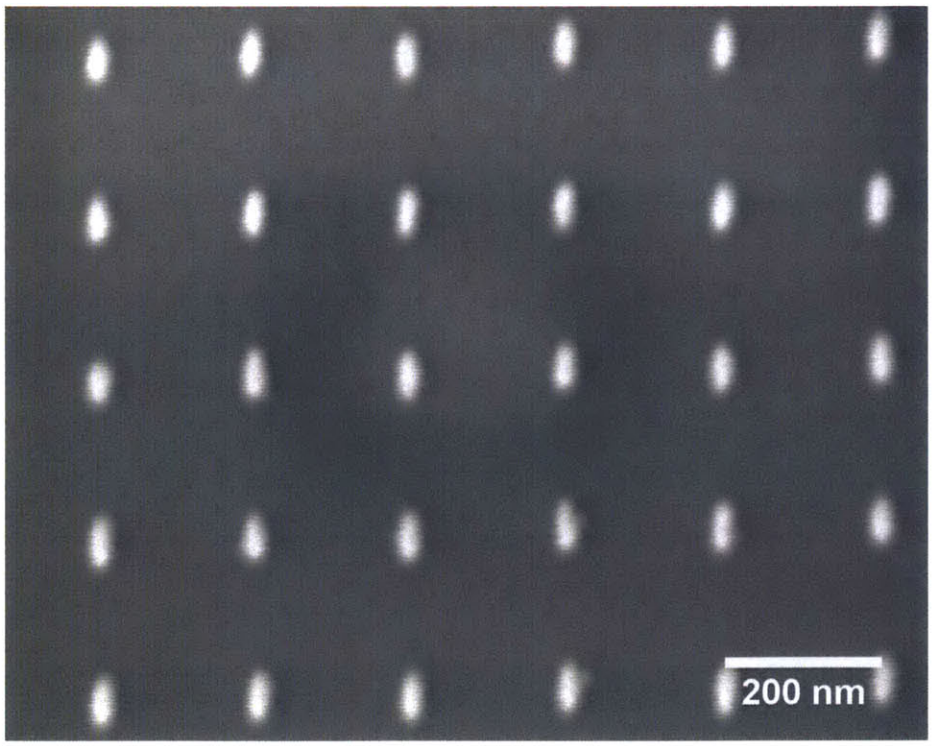

Fig. 4.11. SEM image of fabricated in-plane Au nanorods forming a square array with 200 nm pitch on ITO substrate.

4.4.1 Fabricated Gold Nanorod Array on Si Substrate

In this section, we will discuss the fabricated device on a Si substrate. We first fixed the pitch of the array at 200 nm, and the width and thickness of the Au nanorod at 15 nm and 20 nm (~10 nm above the SiO_2 thin film), respectively. The length of the nanorod was swept from 20 nm to 70 nm with 10 nm step in order to find the optical geometry tuning the LSPR to 800 nm wavelength. The incident optical field was polarized along the long axis of the nanorod. The dielectric permittivity of Au and Ti was taken from Johnson & Christy [58] and the dielectric permittivity of Si and SiO_2 was taken from Palik [59]. The simulated normalized optical power absorption spectra and average field enhancement spectra are shown in Fig. 4.12. The absorption and average field enhancement were evaluated in the same way adopted in previous sections. For longer nanorods, the spectra are similar to the ones shown in previous sections. Two LSPR modes are observed and the longitudinal LSPR mode redshift with increasing nanorod length. However, for shorter nanorods, only the transverse LSPR mode can be seen. According to the results in previous sections, the strong optical response of the Au nanorod at 800 nm is achieved via the longitudinal LSPR mode for nanorods with relatively small aspect-ratio (22 nm length for a 15 nm wide nanorod). This strong optical response can be no longer achieved with the fabricated Au nanorod arrays discussed here.

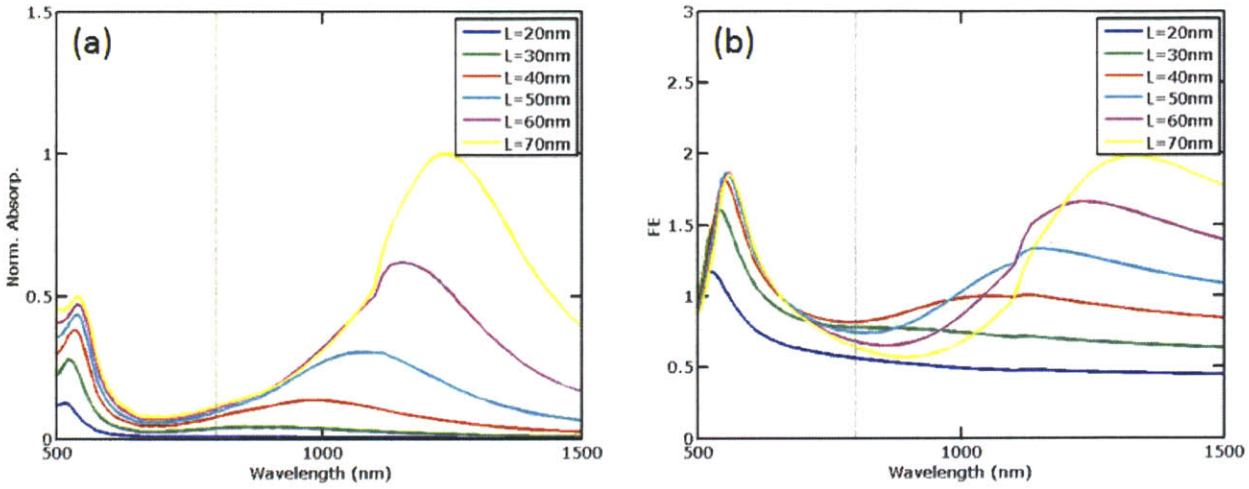

Fig. 4.12. Simulated normalized optical power absorption spectra and average field enhancement spectra for fabricated Au nanorod array with the Ti adhesion layer and SiO_2 thin film. The substrate is Si. The array pitch is 200 nm and the nanorod width and thickness is 15 nm and 20 nm, respectively. The length of the nanorod is swept from 20 nm to 70 nm with a 10 nm step. The dotted line indicates target operating wavelength, 800 nm, in the experiment.

We further modified the geometrical parameters of the fabricated Au nanorod arrays to search for the seemingly disappeared longitudinal LSPR mode for small length nanorod. We reduced the pitch from 200 nm to 100 nm and kept the other parameters unchanged (Figs. 4.13 (a)&(b)), and increased the Au thickness from 20 nm to 30 nm and kept the other parameters unchanged (Figs. 4.13 (c)&(d)). The spectra are only slightly modified by varying the geometrical parameters, while the longitudinal LSPR mode is still missing for short nanorods.

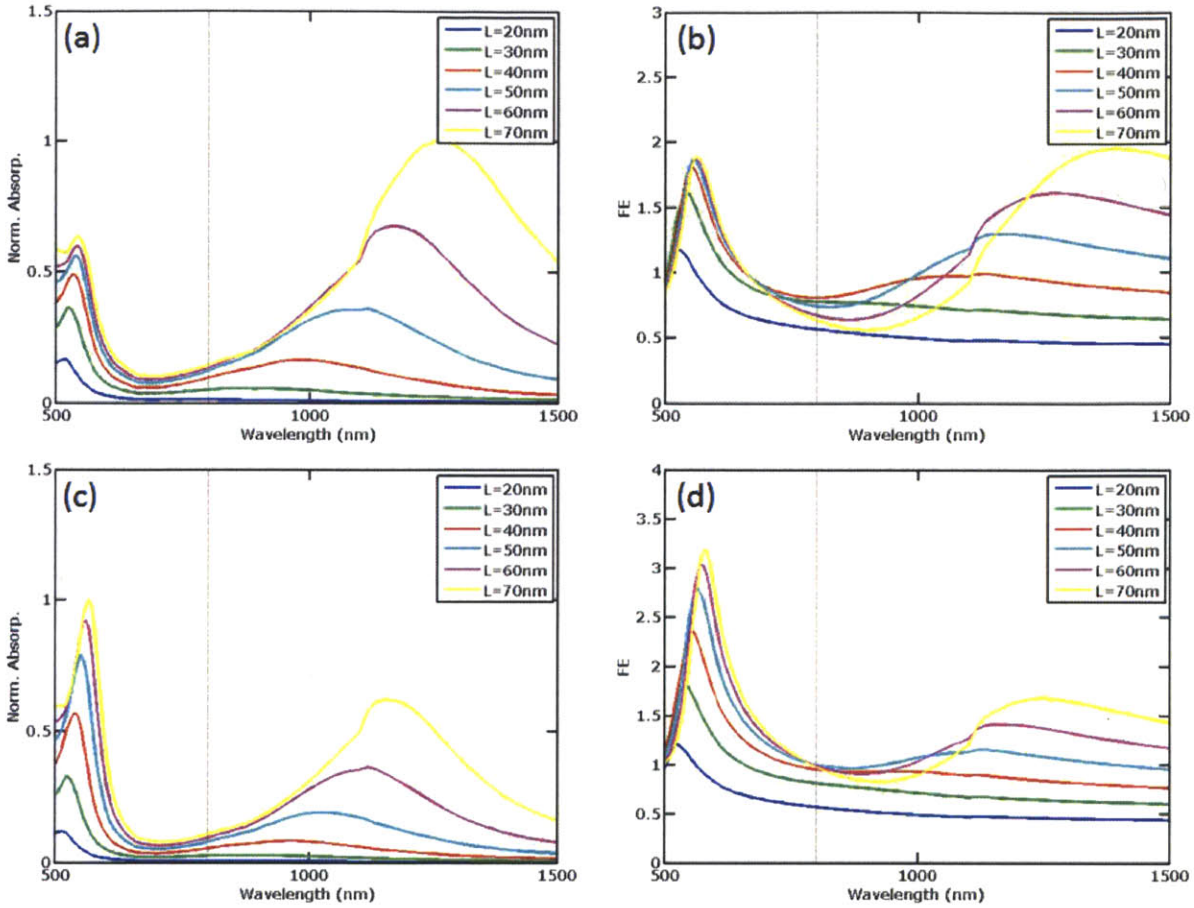

Fig. 4.13. Simulated normalized optical power absorption spectra and average field enhancement spectra for fabricated Au nanorod array with the Ti adhesion layer and SiO_2 thin film. The substrate is Si. The length of the nanorod is swept from 20 nm to 70 nm with 10 nm step. The dotted line indicates target operating wavelength, 800 nm, in the experiment. (a) and (b): The array pitch is 100 nm and the nanorod width and thickness is 15 nm and 20 nm, respectively; (c) and (d): The array pitch is 200 nm and the nanorod width and thickness is 15 nm and 30 nm, respectively.

The major difference between the fabricated Au nanorod and the nanorod in vacuum or directly placed on a substrate is the Ti adhesion layer and SiO_2 thin film. Given that the refractive index of SiO_2 is relatively low and only slightly changes the dielectric environment of the nanorod, we made an assumption that the extinction of the longitudinal LSPR mode of Au nanorod was due to the Ti adhesion layer. This assumption was verified by [72], where the damping of LSPR

mode induced by adhesion layers below lithographically defined metallic nanoparticles was discussed.

Therefore, we simulated the optical response of Au nanorod arrays with and without Ti adhesion layer to investigate its effect. The simulated normalized optical power absorption spectra and average field enhancement spectra are shown in Fig. 4.14. The array pitch was 200 nm, and Au nanorod width, length and thickness were 15 nm, 40 nm, and 20 nm, respectively. The intensity of the longitudinal LSPR peak for the Au nanorod was dramatically reduced by the Ti adhesion layer, verifying the above assumption. The weak mode with its peak between the transverse and longitudinal modes is a substrate-induced dark mode.

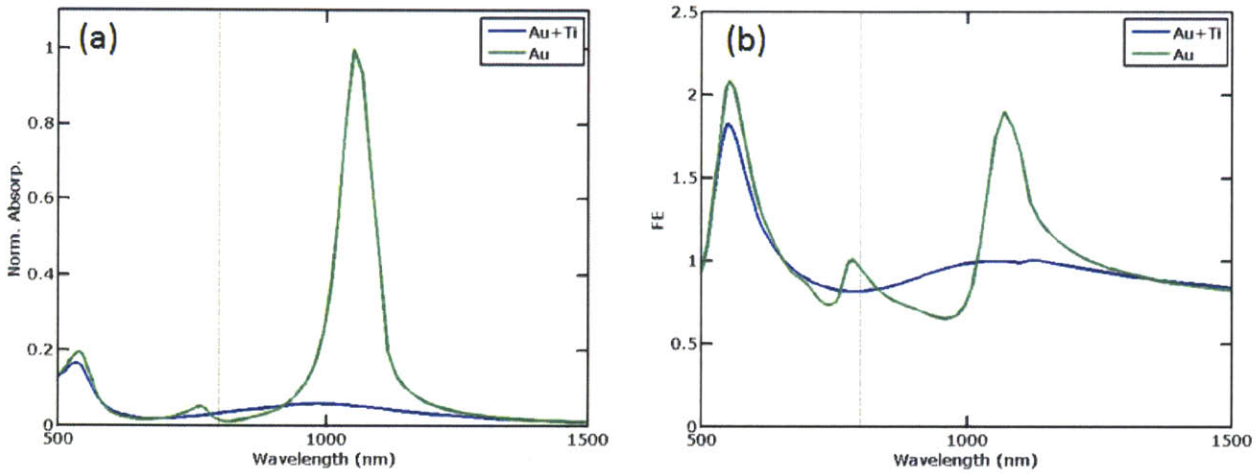

Fig. 4.14. Simulated normalized optical power absorption spectra and average field enhancement spectra for fabricated Au nanorod arrays with and without Ti adhesion layer. The existence of the Ti adhesion layer induces strong damping of the longitudinal LSPR mode. The weak mode with its peak between the transverse and longitudinal modes is substrate induced dark mode.

4.4.2 Fabricated Gold Nanorod Array on ITO Substrate

As discussed in previous sections, the dielectric substrate plays an important role in the performance of the Au nanorod optical field emitter arrays. Substrates with low refractive indices are preferred as the optical power is more evenly distributed around the nanorod rather than localized at the nanorod/substrate interface for high refractive index substrates. Therefore, we considered placing the Au nanorod array on a low-index substrate. The most commonly used substrate for plasmonic applications is SiO_2. However, for optical field emitters, the substrate should be

conductive in order to supply electrons to the emitters. Hence, we turned to Indium Tin Oxide (ITO), a commonly used transparent (low-refractive-index) conductor.

We simulated the optical response of Au nanorod arrays with different lengths on a Si or ITO substrate. The Au nanorod width and thickness were fixed at 15 nm and 20 nm, respectively, and its length was varied as 20 nm, 40 nm, and 60 nm. The 200 nm pitch Au nanorod array was placed on either Si or ITO substrate and a Ti adhesion layer was in between the nanorod and the substrate. Incident optical field was polarized along the long axis of the nanorod. The dielectric permittivity of Au and Ti was taken from Johnson & Christy [58] and the dielectric permittivity of Si and SiO_2 was taken from Palik [59]. The dielectric permittivity of ITO was taken from SOPRA N&K database. The simulated normalized optical power absorption spectra and average field enhancement spectra are shown in Figs. 4.15 (a)&(b), and the optical near-fields for 60 nm length nanorod on ITO and Si substrates at its longitudinal LSPR are shown in Figs. 4.15 (c)&(d), respectively. For 20-nm-long Au nanorod, the longitudinal LSPR mode is not observed for either Si or ITO substrate due to the Ti adhesion layer induced damping. For longer nanorods, the longitudinal LSPR mode can be observed in the spectra. Specifically, an Au nanorod with 60 nm length on ITO substrate has its longitudinal LSPR mode right at the 800 nm target operating wavelength. This is the optimal dimensional and device architecture of the Au nanorod array for application as optical field emitter arrays. Future design will focus on replacing the Ti adhesion layer with a molecular adhesion layer, as suggested in [72], to further enhance the LSPR of the Au nanorods.

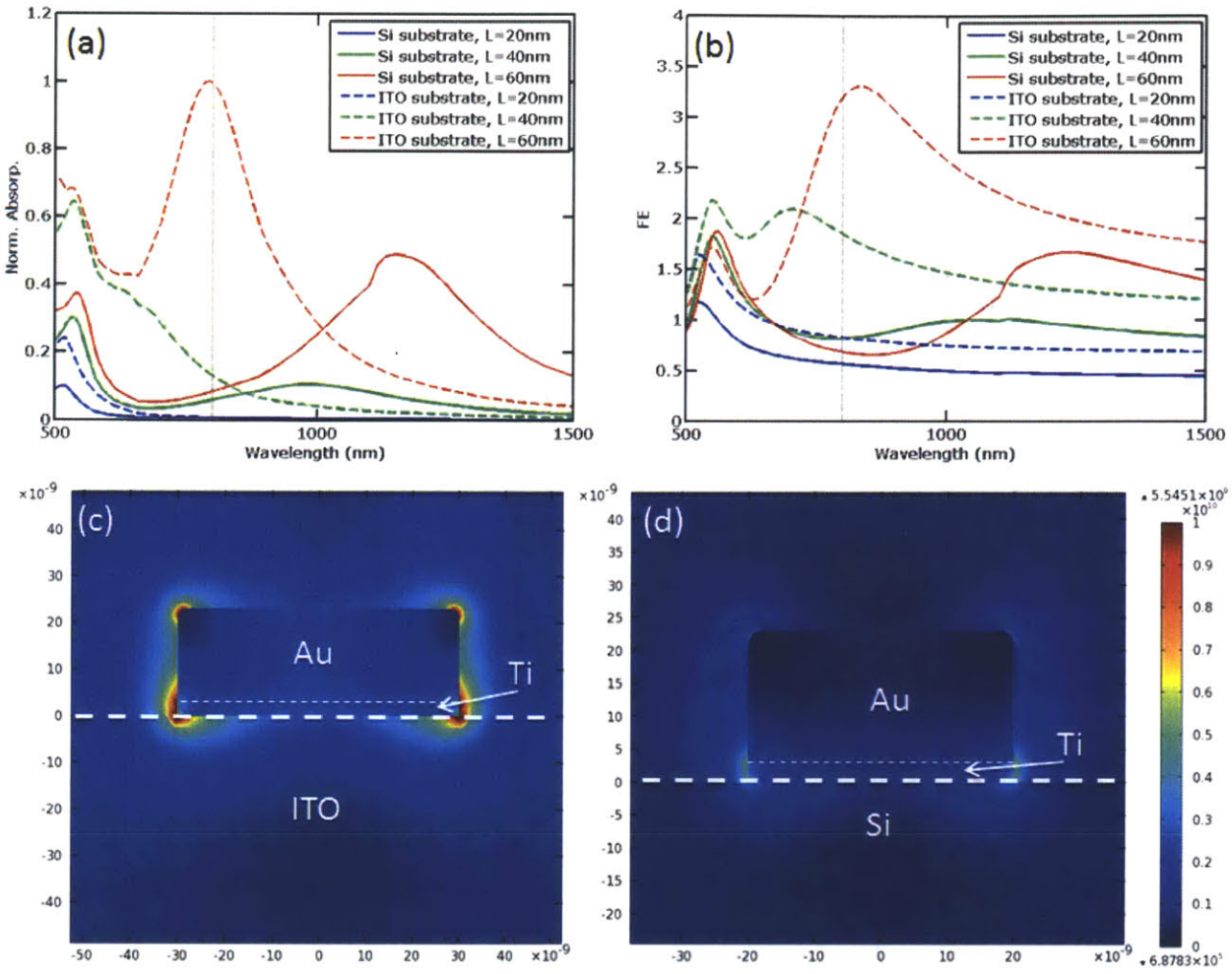

Fig. 4.15. Simulated normalized optical power absorption spectra (a) and average field enhancement spectra (b) for Au nanorod arrays with different lengths on a Si or ITO substrate. The Au nanorod width and thickness were fixed at 15 nm and 20 nm, respectively, and its length was varied as 20 nm, 40 nm and 60 nm. The array pitch is 200 nm. A Ti adhesion layer is in between the nanorod and the substrates. The dotted line indicates target operating wavelength, 800 nm, in the experiment. Optical near-field for 60 nm length nanorod on (c) ITO and (d) Si substrates at its longitudinal LSPR are also shown.

Chapter 5: Modeling Metallic Line Gratings

For the optical field emitter arrays discussed in Chapters 3 & 4, a 2D periodicity is imposed on the nanostructured photocathode. Many applications, however, only require 1D periodicity, namely, periodic arrays of line emitters. The periodic line array is the conventional (1D) metallic grating structure that has long been investigated. Moreover, in the sense of enhanced power absorption and multiphoton emission, the grating structure is compatible with excitation by normally incident light that is more commonly used in photocathode chambers. A nanostructured surface was shown to reduce reflection and improve absorption of light incident on metals, based on metamaterial behavior or the excitation of plasmon resonance. Hutley *et al.* reported total absorption of light by gold with a sinusoidally patterned surface [73]. Bonod *et al.* showed theoretically total absorption of light by lamellar metallic gratings, and ascribed absorption of the TM wave to excitation of surface plasmons and absorption of TE to cavity modes in deep grooves [74]. Popov *et al.* studied the absorption of light by shallow silver gratings and showed metamaterial behavior rather than plasmon resonance contributed to the full absorption [75]. Enhanced optical near-field and power absorption by periodically nanostructured metallic surface has been proposed for enhancing solar cell performance. Wang *et al.* used silver gratings as the back contact for thin film Si solar cells to enhance light absorption via excitation of SPP waves [76]. Abass *et al.* used a similar technique to enhance light absorption in thin film organic solar cells [77]. Multilayer plasmonic absorbers are recently showed to absorb almost all incident optical power and termed as "plasmonic blackbodies". Hao *et al.* theoretically investigated nearly total absorption by a plasmonic-metamaterial/dielectric-thin-film/metallic-back-layer stack structure [78].

However, there have not been many investigations of electron emission from metallic gratings. A nanostructured electron beamlet source should possess a number of features to find use in field emitter array displays or advanced multibeam EBL applications, as well as the recently proposed emittance exchange ICS X-ray sources. The electron source should contain a high density of emitters, thus maximizing the number of electron beamlets produced. Additionally, background electron emission brightness from interstitial sites between emitters

should be low with respect to the brightness of the emitters. Also, the filling factor of the emitter should be low ($\leq 25\%$) to enable emittance exchange. Many of the published strategies toward improved absorption of light described above possess inherent drawbacks for the preparation of a nanostructured electron beam array. Nanostructuring metal surfaces can be used to achieve high optical absorbance, however electron emission can occur from all areas of the metal surface. Metamaterials based on deep grooves or complicated surface structures suffer from not only background electron emission but also difficulties in fabrication. For multilayer plasmonic absorbers, emission of electrons requires that the majority of optical power should be absorbed in the top layer, and power absorption in the intermediate and back layers of the multilayer plasmonic absorbers only turns into heat.

In this Chapter, we will propose a discontinuous metallic grating structure with low filling factor and ideally no background emission as the optical field emitter. Theoretical analysis and numerical simulations via finite element software COMSOL were used for optimizing the design of metallic line grating optical field emitter arrays.

5.1 Copper Grating on Silicon Substrate

We started by considering a copper (Cu) grating structure on silicon (Si) substrate as a metallic line grating optical field emitter array since Cu was widely used as the material for photocathodes. Here we focused on the multiphoton emission from Cu when illuminated with infra-red (800 nm) laser. We also assumed a constant quantum efficiency for Cu, namely, the more optical power absorbed, the more electrons emitted. Hence, the goal of the design is to maximize optical power absorption.

For a continuous grating or discontinuous grating with few nanometer gaps, SPP can be excited if the condition in equation (2.78) is met. However, for the Cu grating structure discussed here, it is required by the application in emittance exchange X-ray sources to be discontinuous and possess a low filling factor. Thus, surface plasmons cannot be excited in the conventional way. We swept various geometrical parameters in the numerical simulation to find the optimal grating structure for an optical field emitter array.

5.1.1 Model Setup

Model setup and coordinate definition are illustrated in Fig. 5.1. 2D model (cross-section plane) in COMSOL was used as it assumed uniformity in the 3rd dimension, which agreed with the reality for a Cu line or grating. The Cu line had a rectangular cross section with the corners rounded in the model. A 3 nm thin Ti adhesion promoting layer was in between the Cu line and the Si substrate. Thin film SiO_2 with 10 nm thickness was used to block electron emission from the substrate. Perfectly matched layers (PMLs) were adopted for top and bottom layers, absorbing reflected, transmitted and scattered optical waves. Port boundary condition was used as the excitation source with normally incident plane waves. Both TE and TM incident waves were investigated, with TE defined as the plane wave whose electric field was parallel to the grating (in z direction), or perpendicular to the cross-section plane, and TM defined as the plane wave whose electric field was perpendicular to the grating (in x direction), or parallel to the cross-section plane. The Cu emitter was placed on Si substrate and in vacuum medium.

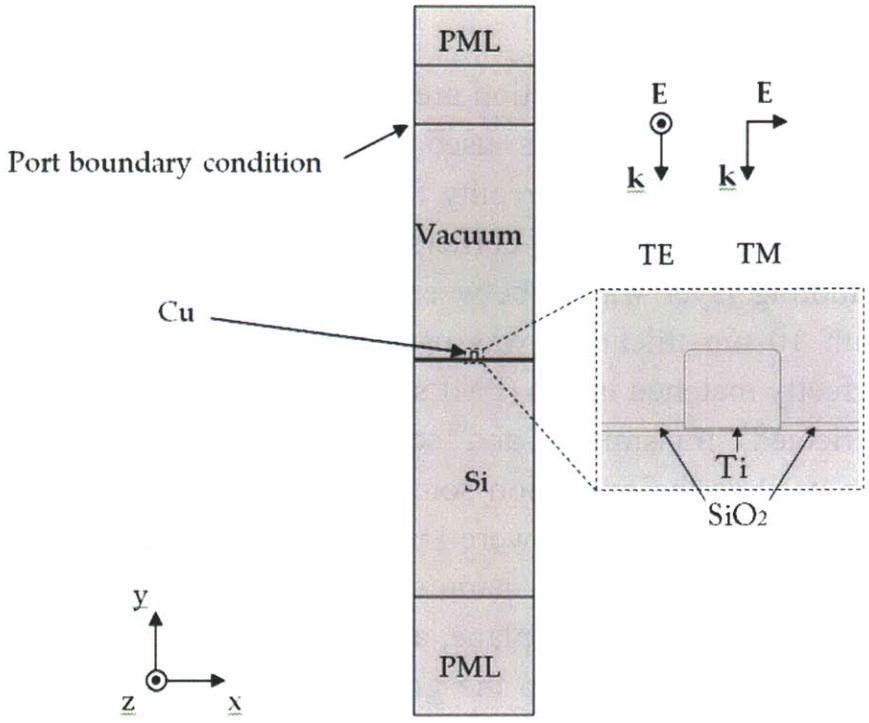

Fig. 5.1. Model setup and coordinate definition for modeling metallic line grating optical field emitter arrays. Top and bottom layers are PMLs used to absorb reflected, transmitted and scattered optical waves. TE and TM illuminations are shown. Inset: zoom-in figure of the Cu line illustrating Ti adhesion layer and SiO_2 thin film.

To model a single Cu line, scattering boundary condition was applied to the left and right boundaries. To model a periodic Cu grating, periodic boundary condition was applied to the left and right boundaries. The optical wavelength was fixed at 800nm if not specified otherwise. Total power absorption was evaluated by integrating the power dissipation ([W/m^3]) density over the Cu cross-section ([m^2]). Hence the unit of total power absorption was [W/m] and the value represented the total power absorption in a unit length (1 m) (in z direction) by a Cu line. The complex refractive indices of Cu, Si, Ti and SiO_2 at 800 nm were $n(Cu) = 0.250 + 5.03i$, $n(Si) = 3.694$, $n(Ti) = 2.861 + 3.317i$ and $n(SiO_2) = 1.54$, respectively. The 2D model was adaptively meshed with triangular elements with 1 nm minimum dimension for the thin Ti adhesion layer, 2 nm minimum dimension for the SiO_2 thin film and 3 nm minimum dimension for the Cu line.

5.1.2 Line Width Optimization: Surface Plasmon Polariton Cavity

In this section, the dependence of optical power absorption by an individual Cu line on its width is studied. A periodic boundary condition was used, and the pitch was set to a large value of 5 μm to avoid coupling between adjacent Cu lines.

First, the line width and height (thickness) parameters were swept and the power absorption calculated. The line width was swept from 30 nm to 120 nm with 10 nm step and the height was swept from 10 nm to 100 nm with 10 nm step. The simulation results for both TE and TM waves are shown in Fig. 5.2.

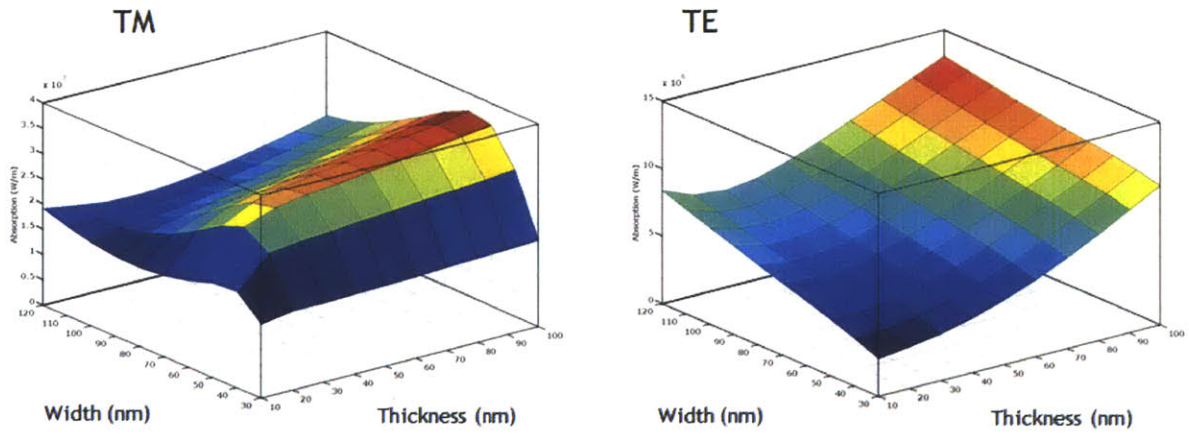

Fig. 5.2. Simulated power absorption of an individual Cu line under TM and TE illuminations as a function of Cu line width and thickness.

The relationship between power absorption and Cu line thickness is quite intuitive: the thicker the line, the higher the absorption. This simple rule is violated for ultra-thin lines, which will be discussed later.

The relationship between power absorption and Cu line width for TE illumination is also intuitive. Larger width corresponds to larger optical absorption cross section and leads to higher power absorption. However, for TM illumination, the power absorption reaches a peak value at around 60nm-70nm line thickness and this resonant absorption is quite counter-intuitive.

Further simulations were run with a fixed line thickness at 60nm, sweeping the width parameter over a larger range. The results of the width-dependent power absorption calculations for TM illumination are shown in Fig. 5.3.

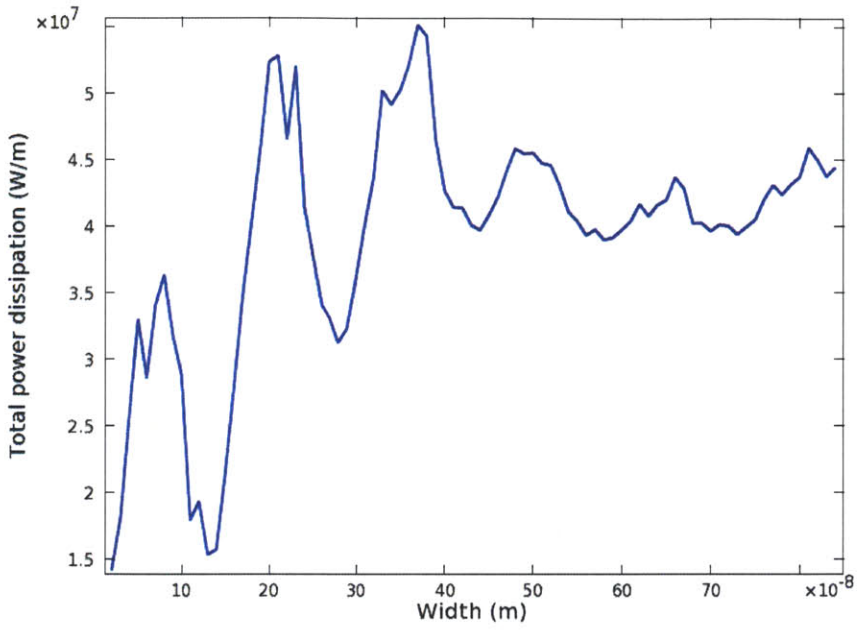

Fig. 5.3. Simulated width-dependent power absorption for TM illumination. Cu line thickness is fixed at 60nm.

From Fig. 5.3, it is clear that there are multiple absorption peaks and they are separated by approximately a line width value of 150 nm. To better investigate these resonant peaks, the near-field profile was plotted for lines with dimensions corresponding to each of these peaks. As the incident wave has a TM polarization, the only magnetic field component Hz is shown in Fig. 5.4 for four line width values corresponding to the first four absorption peaks in Fig. 5.3, at width values of 80, 230, 380, and 520 nm.

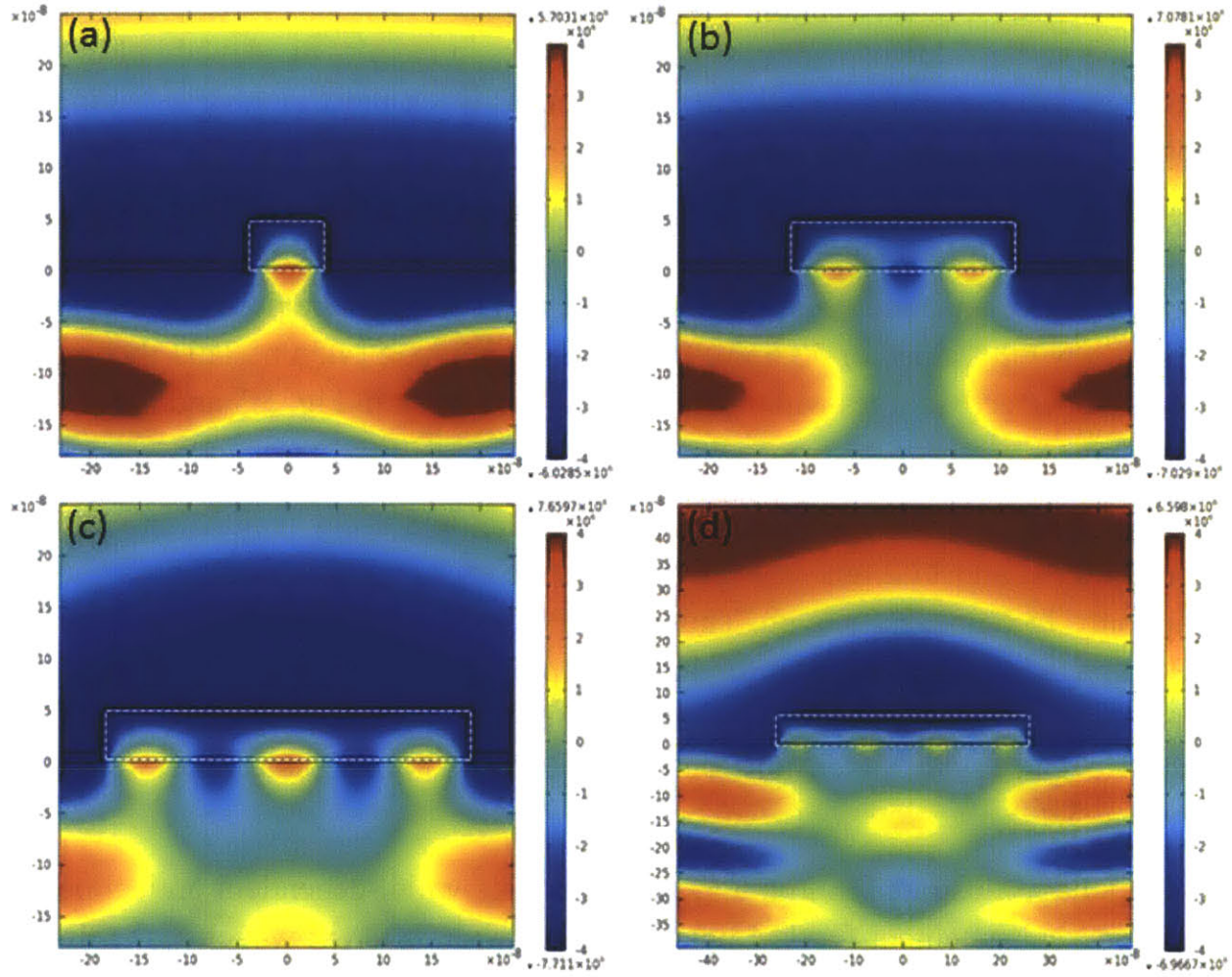

Fig. 5.4. Magnetic field profile (Hz) for line width of (a) 80nm; (b) 230nm; (c) 380nm; (d) 520nm. These line width values correspond to the first four peaks in Fig. 5.3. The plots display transverse cross-sections through the Cu nanowires. The cavity is formed by confining the SPP in the transverse direction by the nanowire's finite width. These SPP cavity modes are excited when the nanowire width matches an odd integral multiple of half the SPP wavelength (λ_{SPP}) at Cu/Si interface.

An interesting phenomenon illustrated in Fig. 5.4 is the standing wave profile at the interface between Cu line and Si substrate. The wave property along the interface and decay property perpendicular to the interface remind us of the characteristics of surface plasmon polariton (SPP) waves. Therefore, we proposed a hypothesis that absorption peaks were results of the excitation of SPP modes.

It can be evaluated from the SPP dispersion relation at Cu/Si interface, equation (2.77), that the SPP wavelength is 147nm. The value of 147 nm corresponds to the difference in the value of width for adjacent peaks in the plot displayed in Fig. 5.3. The peaks in the plot presented in Fig. 5.3 occur when the width value is an odd integral multiple of the SPP wavelength:

$$w_n = (2n+1)\frac{\lambda_{SPP}}{2}, n = 0, 1, 2, \ldots \quad (5.1)$$

From the above equation, the first four absorption peaks can be predicated to show up at line width values of 73.5nm, 220.5nm, 367.5nm, 514.5nm. This theoretical prediction perfectly agrees with the numerical simulation in Fig. 5.3 and Fig. 5.4.

It is also interesting to investigate the SPP decay length away from the Cu/Si interface. From the discussion in section 2.3.2, the field decay lengths into Cu and Si are 31.8 nm and 17.2 nm, respectively, and the energy decay lengths into Cu and Si are only 15.6 nm and 8.6 nm. Thus, the SPP cavity provides confinement in the SPP propagation direction, and the interface provides confinement in the direction transverse to SPP propagation, leading to a 3D confinement of optical energy in a nanoscale space with dimensions on the order of ~10 nm. This can be visualized from Fig. 5.4.

Further study, illustrated in Fig. 5.5, shows the line-width-dependent optical power absorption enhancement for TM polarized light with different wavelengths. In the numerical simulation, the wavelength dependent optical properties of Cu and Ti were taken from Johnson & Christy [58], while the wavelength dependent optical properties of Si and SiO_2 were taken from Palik [59]. The cavity lengths, which are odd integral multiples of the SPP wavelength, are also plotted. The two high power absorption regions in the figure correspond to the first two cavity lengths, $\frac{\lambda_{SPP}}{2}$ and $\frac{3\lambda_{SPP}}{2}$, respectively. The displacement between numerical simulation and theoretical calculation comes from the approximation that neglects the imaginary part of the dielectric function of Cu. SPP propagation constant is known to be shifted by a small amount due to leakage caused by absorption in metal. Also, the existence of the thin Ti adhesion layer can modify the SPP dispersion relation. Moreover, the theoretical calculation is based on the dispersion relation of a planar interface, which can be slightly different from a cavity with finite length.

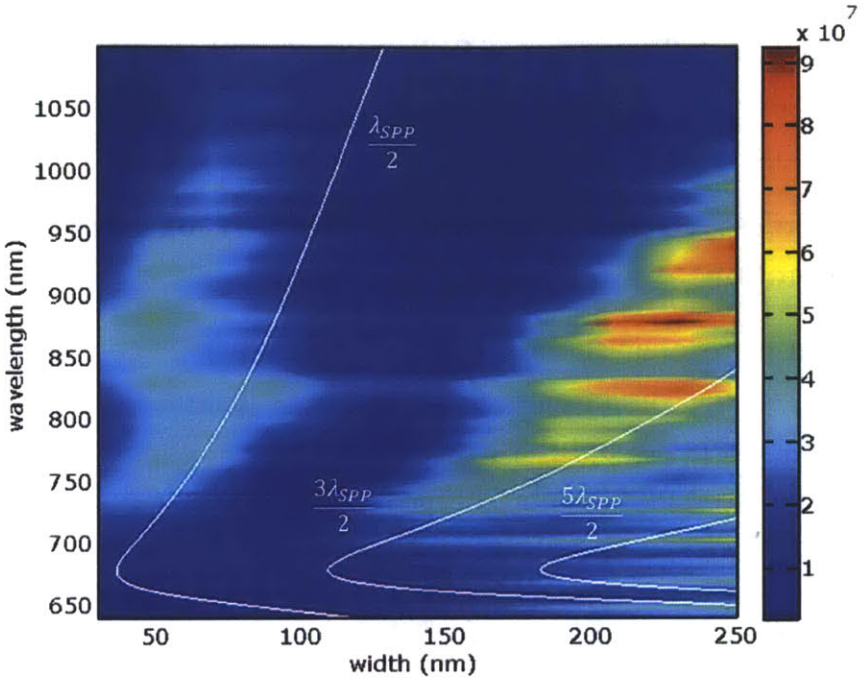

Fig. 5.5. Simulated Cu line width dependent power absorption for different optical wavelengths. The plane wave excitation is at normal incidence and TM polarized. Cavity lengths supporting the first three SPP cavity modes are plotted as white curve in the figure.

A single metallic wire illuminated by TM polarized optical wave is a well-known structure for localized surface plasmon resonance (LSPR) excitation and often serves as a textbook example due to its simplicity for mathematical analysis. Here we have shown that when placed on Si substrate, an SPP cavity can be created since the SPP wavelength is much smaller than the free space wavelength and comparable to the width of the metallic wire due to the large dielectric function of the substrate. This is in stark contrast to the SPP at metal/air interface where its wavelength is approximately the same as the free space wavelength. Moreover, for the SPP cavity discussed here, the excitation of the SPP wave comes from the coupling between LSPR and SPP, meaning no special phase matching techniques like Kretschmann or Otto configurations are needed as long as the cavity dimensions are carefully designed and fabricated.

In conclusion, SPP wave is excited by TM illumination and the finite width in the transverse direction of the Cu line serves as a "cavity" of the SPP wave localized at Cu/Si interface. SPP cavity modes are supported if the width of the Cu line is an

odd integral multiple of the SPP wavelength, and these SPP cavity modes lead to power absorption peaks. The ideas of SPP cavity based on an individual metallic wire placed on a dielectric substrate and the excitation of SPP wave by LSPR are both very interesting.

5.1.3 Line Thickness (Height) Discussion: Validity of Constant Quantum-Efficiency Assumption

There is no strong or resonant dependency of optical power absorption on Cu line thickness (height in the direction normal to the substrate surface). Hence this geometrical dimension is not optimized. However, the assumption we made earlier that multiphoton electron emission is directly related to optical power absorption is no longer valid for thick Cu line. As we have seen in Fig. 5.4, the optical energy is primarily localized at Cu/Si interface, while electron emission prefers energy localization at the metal surface, namely, Cu/Vacuum interface.

As shown in Fig. 5.2, the thicker the line, the higher the absorption. This simple rule is violated by ultra-thin lines when the thickness is below the skin depth of Cu at 800nm wavelength, 17nm. For such thin lines, the fields localized at upper and lower surface couple with each other and complicate the situation. Further study of this ultra-thin line can be conducted if this structure is desired to facilitate electron emission.

5.1.4 Grating Pitch Optimization: Rayleigh Anomalies

In this section, the dependence of optical power absorption by a Cu line grating on its pitch is studied. A periodic boundary condition is used, and the pitch is varied to optimize the power absorption.

First, we swept the line width and grating pitch simultaneously to investigate whether there are collaborative effects of the two. The line width was swept from 20 nm to 120 nm with 10 nm step, and the grating pitch was swept from 100 nm to 800 nm with 50 nm step. The simulation results for both TE and TM waves are shown in Fig. 5.6.

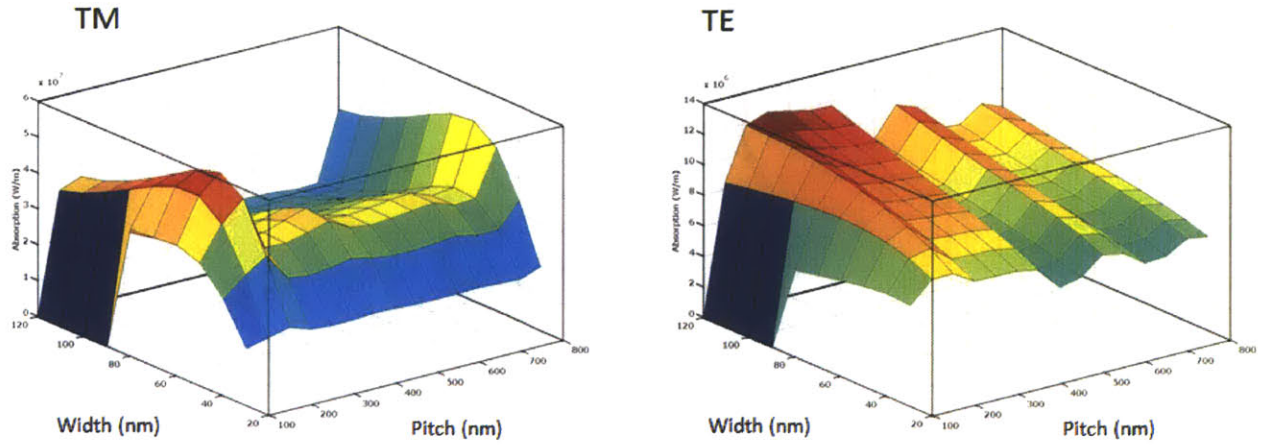

Fig. 5.6. Simulated power absorption of a Cu line grating under TM and TE illuminations as a function of line width and grating pitch.

It can be seen the dependences of power absorption on line width and grating pitch are not strongly relevant to each other. The 60-70 nm line width with TM illumination is optimal for enhancing power absorption, as discussed in section 5.1.2. TM illumination results in higher power absorption compared with TE illumination. The pitch dependence of TM case shows two peaks at around 200 nm and 800 nm pitch values, while the power absorption of TE case reaches its maxima at around 200 nm pitch.

We then fixed the line width to 60 nm, the optimized value, and the line thickness to 50 nm, and sweep the grating pitch parameter from 100 nm to 2100 nm with 25 nm step. The results of the pitch-dependent power absorption for both TE and TM incident waves are shown in Fig. 5.7. Several peaks can be observed indicating potential resonances when the grating pitch is at the position of one of these peaks.

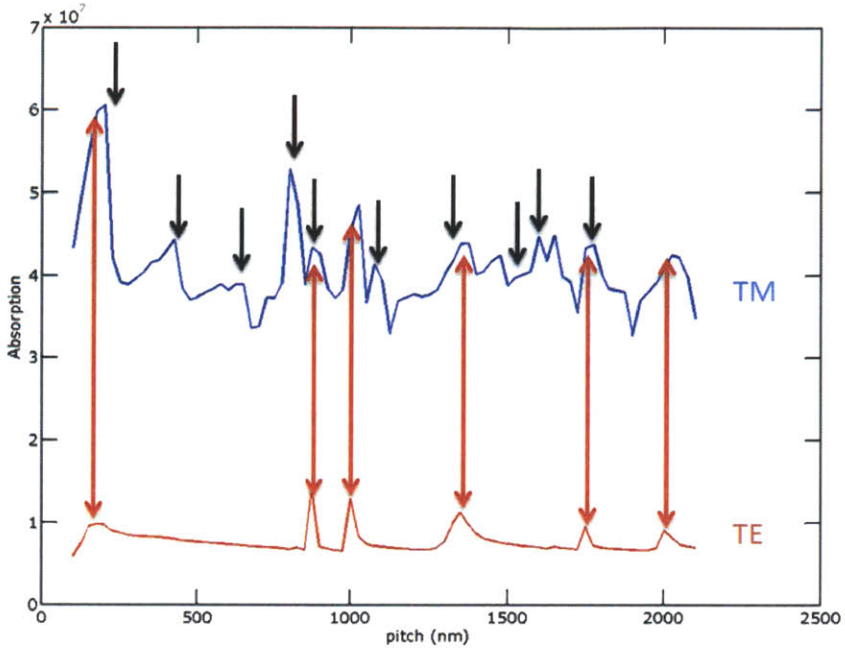

Fig. 5.7. Simulated pitch-dependent power absorption for both TE and TM illuminations. The black arrows indicate expected Rayleigh anomaly peak positions, and the red double-arrows indicate peaks in both TE and TM cases that cannot be explained by Rayleigh's theory (see text for details).

We assumed the absorption peaks in Fig. 5.7 were associated with Wood's anomalies which refer to the abrupt changes in energy distribution in different diffraction orders from a grating, discovered by and named after R. W. Wood [79]. Wood's anomalies are usually seen in TM or s-polarization where the electric field is perpendicular to the grating lines, and rarely observed in TE or p-polarization where the electric field is along the grating lines. For lossy gratings such as a metallic line grating, significant optical power absorption is often associated with Wood's anomalies.

Lord Rayleigh's diffraction theory provides a simple explanation of the Wood's anomalies [80]. The abrupt change of the energy distribution in different diffraction orders from a metallic grating and the associated resonant absorption in the lossy grating was ascribed to the emergence of a new diffraction order, which happened at grating pitch values satisfying

$$p_m sin\theta = m\lambda, m = 1, 2, \ldots \quad (5.2)$$

For normal incidence as in the numerical model, $\theta = 90°$. Moreover, since the grating is at the interface of two different dielectrics (vacuum and Si), the wavelength in equation (5.2) can be either wavelength in free space λ_0 or wavelength in Si λ_{Si}. Thus, the Wood's anomalies satisfying Rayleigh's condition, or Rayleigh anomalies, show up when

$$p_m = m\lambda_0 \; or \; m\lambda_{Si}, m = 1, 2, \ldots \tag{5.3}$$

One way to understand Rayleigh's theory is that when a new diffraction order just emerges, its direction is horizontal, namely, the newly diffracted beam will propagate horizontally and traverse the whole grating, resulting in peak power absorption (Fig. 5.8(a)). Another way of understanding Rayleigh's theory is that under TM illumination, each individual line in the grating will resonate like an electric dipole. When they are separated by an integer multiple of the wavelength, the electromagnetic wave generated from one dipole and propagating to another dipole is in-phase with the oscillation of the second dipole, leading to constructive interference (Fig. 5.8(b)).

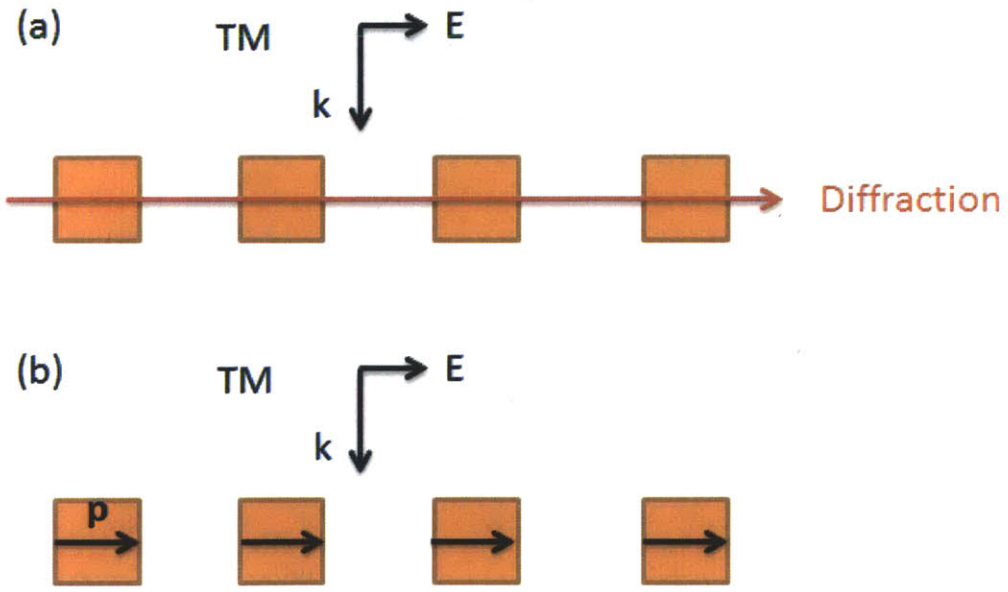

Fig. 5.8. Schematics showing Rayleigh's explanation for Wood's anomalies. (a) Horizontally diffracted beam; (b) constructively interfering dipoles.

The Rayleigh anomalies are highlighted with black arrows in Fig. 5.7, predicting most of the peak positions reasonably well. Thus, Rayleigh's theory matches the numerical simulation. Those peaks that cannot be explained by Rayleigh's theory exist at the same positions for both TE and TM waves, highlighted by red double-

arrows in Fig. 5.7. As will be seen later in this section, these peaks correspond to spurious modes caused by numerical artifacts and do not exist in reality.

Further study, illustrated in Fig. 5.9, shows the grating-pitch-dependent optical power absorption enhancement for TM polarized light with different wavelengths. In the numerical simulation, the wavelength dependent optical properties of Cu and Ti are taken from Johnson & Christy [58], while the wavelength dependent optical properties of Si and SiO_2 are taken from Palik [59]. The power absorption enhancement at 800 nm to 1000 nm wavelength region is due to the SPP cavity modes for optimized line width, while the high power absorption below 600 nm wavelength is due to intrinsic material properties (e.g. interband transitions). Rayleigh anomalies are shown as black dashed straight lines in the figure, matching well with numerical simulations. The red dotted curves indicate numerical artifacts induced spurious modes.

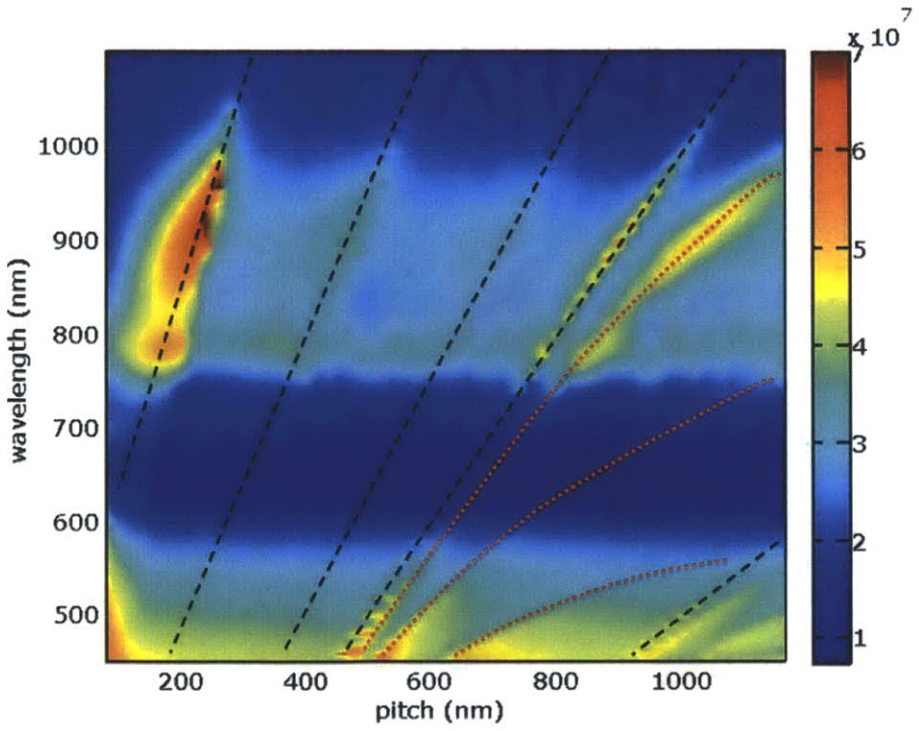

Fig. 5.9. Simulated Cu grating pitch dependent power absorption for different optical wavelengths. The plane wave excitation is at normal incidence and TM polarized. Rayleigh anomalies are shown as black dashed straight lines in the figure, matching well with numerical simulations. The red dotted curves indicate numerical artifacts induced spurious modes.

The spurious modes mentioned above occasionally happen due to discretization in finite element method. We further ran the simulation with different meshings and calculation domain sizes, and looked at the frequency-dependent absorption spectra to verify whether the absorption peaks at 800 nm free space wavelength ($3.75 \times 10^{14}\ Hz$ frequency) are real or spurious modes. We first ran the frequency-dependent simulation for exactly the identical model setup as mentioned above. The grating pitches were chosen as 800 nm corresponding to a Rayleigh anomaly for 800 nm light, and 875 nm, 1000 nm and 1350 nm corresponding to three absorption peaks for 800 nm light that cannot be explained theoretically. The absorption spectra for the four grating pitches under TE and TM illuminations are shown in Fig. 5.10. Though for TM illumination (Fig. 5.10(b)) all the four different pitches result in absorption peaks at 800 nm, the unusual weak absorption peaks at low frequencies and strong oscillations at high frequencies in the TE case (Fig. 5.10(a)) suggest spurious modes exist in the numerical simulation.

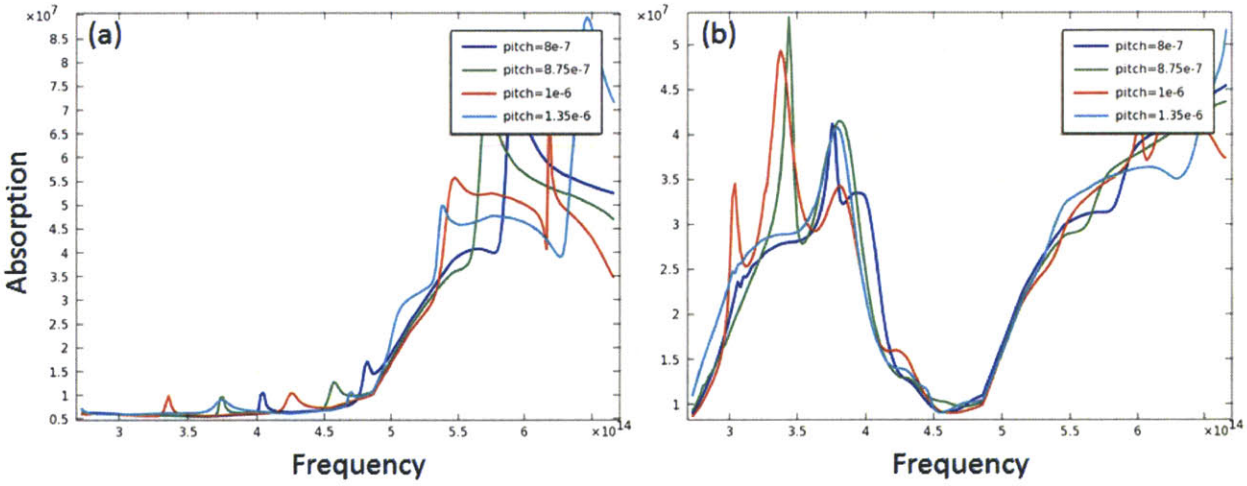

Fig. 5.10. Simulated absorption spectra of Cu grating with 800 nm, 875 nm, 1000 nm and 1350 nm pitches under (a) TE and (b) TM illuminations.

Therefore, we varied the meshing element size by $\pm 10\%$ and the calculation domain size from 300 nm to 1 um. One typical result for TE illumination is shown in Fig. 5.11(a). The changes of numerical parameters should not change the resultant absorption spectra, but the new result differs from the old one in Fig. 5.10(a). Thus, the modes are unphysical spurious modes caused by numerical artifacts and can be eliminated by carefully choosing the numerical simulation parameters. With the slightly changed numerical parameters, we also simulated the

optical power absorption under 800 nm wavelength TE illumination, sweep the grating pitch from 800 nm to 1100 nm. The result is shown in Fig. 5.11(b). Compared to Fig. 5.7, the spurious modes at 875 nm and 1000 nm pitches are eliminated.

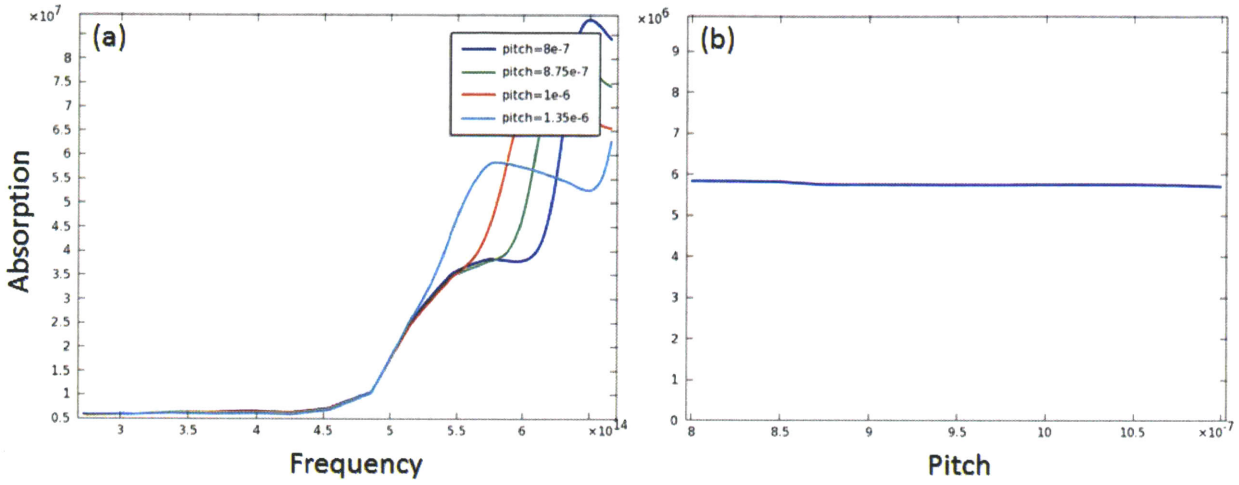

Fig. 5.11. (a) Simulated absorption spectra of Cu grating with 800 nm, 875 nm, 1000 nm and 1350 nm pitches under TE illumination with slightly changed numerical parameters including FEM meshing element size and calculation domain size. Compared to Fig. 5.10(a), the spurious modes are eliminated. (b) Simulated optical power absorption of Cu grating with pitch varying from 800 nm to 1100 nm under 800 nm wavelength TE illumination. Compared to Fig. 5.7, the spurious modes at 875 nm and 1000 nm pitches are eliminated.

Finally, we re-simulated the absorption spectra of Cu grating with 800 nm, 830 nm, 875 nm, 940 nm, 1000 nm, 1170 nm and 1350 nm pitches under TM illuminations. The results are shown in Fig. 5.12. The curves in the spectra become smoother after the elimination of spurious modes. Among these pitch values, only the 800 nm pitch Rayleigh anomaly gives a strong absorption peak at 800 nm free space wavelength ($3.75 \times 10^{14}\ Hz$ frequency) and the peak intensity gradually decreases with increasing pitch. This can be explained by the double-peak feature in the spectrum. One peak at 800 nm free space wavelength ($3.75 \times 10^{14}\ Hz$ frequency) does not shift with varying pitch. It is induced by the SPP cavity mode discussed in section 5.1.2 and irrelevant to the grating pitch. The other peak redshifts with increasing pitch. It is the Rayleigh anomaly so that its position in the spectrum strongly depends on the grating pitch according to equation (5.3). When the two

peaks coincide with each other, namely at 800 nm pitch value, a single strong absorption peak shows up in the spectrum.

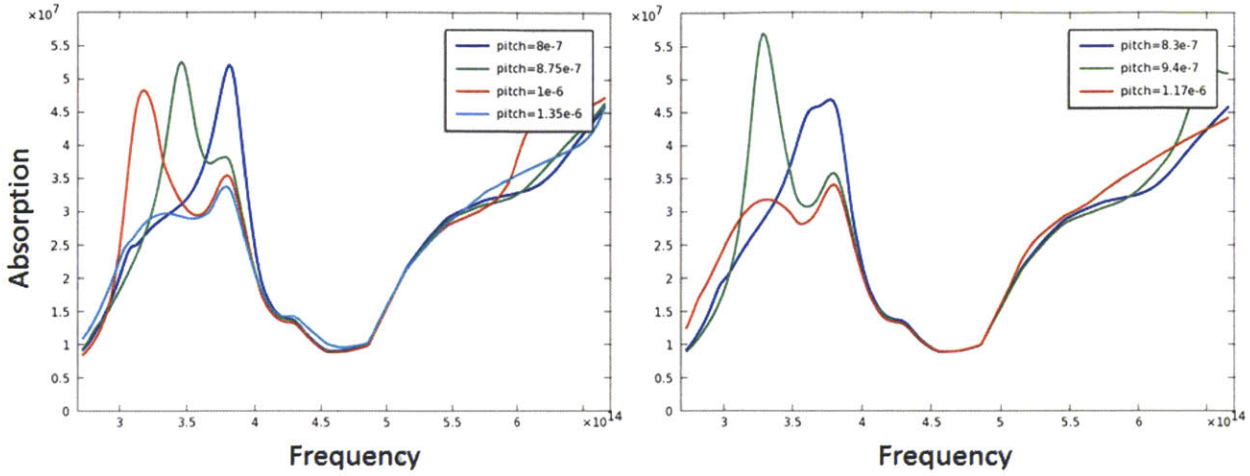

Fig. 5.12. Simulated absorption spectra of Cu grating with 800 nm, 830 nm, 875 nm, 940 nm, 1000 nm, 1170 nm and 1350 nm pitches under TM illuminations.

5.1.5 Metamaterial Behavior of Copper Gratings

Untill now, all real absorption peaks under TM illumination are well explained by Rayleigh's anomalies. We notice for TE illumination of 800 nm light, the power absorption reaches a maximum when the grating pitch is around 200 nm. Since Rayleigh's anomaly exists only for TM case, we turn to the metamaterial behavior of the grating for an explanation. For a grating with pitch much smaller than the optical wavelength, the grating can be treated as a metamaterial and its optical response can be analyzed by the effective medium theory. Given that 200 nm pitch is actually in the same order of magnitude with 800 nm wavelength, the metamaterial model can be inaccurate. But we expect to get a result matching with previous FEM numerical simulations qualitatively. Assuming the Cu grating line width is w and the grating pitch is p, the effective dielectric permittivity of the grating for TE and TM illuminations can be evaluated from [74]

$$\epsilon_{TE} = \frac{w}{p}\epsilon_{Cu} + \frac{p-w}{p}\epsilon_{Vacuum} \tag{5.4}$$

$$\epsilon_{TM} = \frac{p}{\frac{w}{\epsilon_{Cu}} + \frac{p-w}{\epsilon_{Vacuum}}} \tag{5.5}$$

With the grating treated as a thin film metamaterial, the Cu grating on Si substrate can be modeled by a simple vacuum/metamaterial/Si stack and the absorption can be calculated from standard transfer matrix method treatment of layered media. We evaluated the TE dielectric permittivity from equation (5.4) and used transfer matrix method to calculate the power absorption within the metamaterial. The result is illustrated in Fig. 5.13. The metamaterial thickness, or grating thickness, was varied from 0 to 100 nm. Grating pitch values were 100 nm, 150 nm, 200 nm, 250 nm and 300 nm, resulting in different metamaterial behavior. Our previous simulation chose 60 nm thick grating. According to Fig. 5.13, the metamaterial behavior of a 200 nm grating leads to highest power absorption compared to other pitch values. Thus, the absorption peak for TE illumination at 200 nm pitch is due to the material behavior.

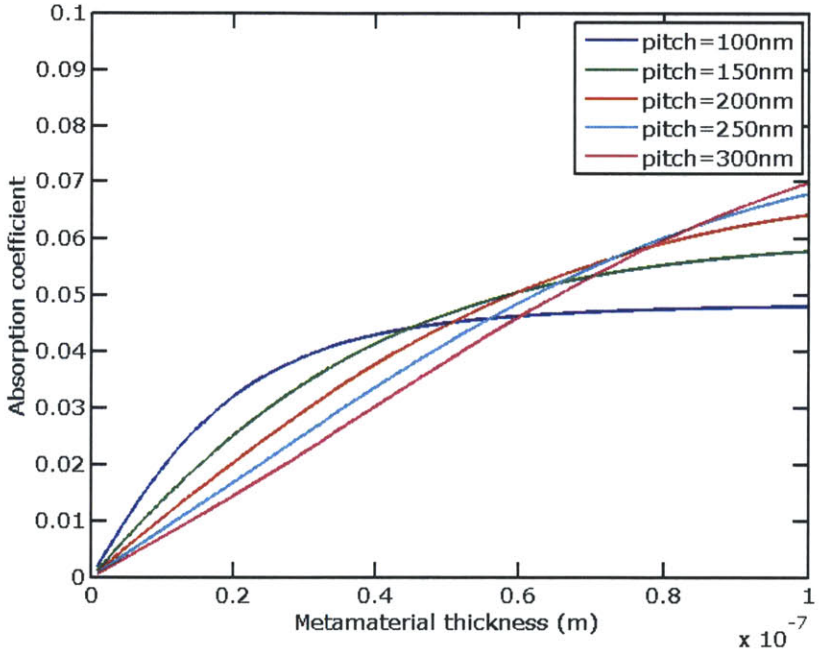

Fig. 5.13. Metamaterial behavior of Cu grating under 800 nm wavelength TE illumination on a Si substrate. The metamaterial thickness, or grating thickness, is varied from 0 to 100 nm. Grating pitch values are 100 nm, 150 nm, 200 nm, 250 nm and 300 nm, resulting in different metamaterial behavior. Absorption coefficient is calculated by transfer matrix of the vacuum/metamaterial/Si layered media.

Chapter 6: Summary and Future Work

In this thesis, optical field emitter arrays were developed for applications in emittance-exchange ICS X-ray sources. Several optical field emitter array structures, including vertically-standing gold nanopillars and silicon tips, in-plane gold nanostructures, and metallic line gratings, were studied via theoretical analysis and numerical simulations. Enhancement of the optical near-field and power absorption was achieved by geometrical and plasmonic effects, leading to enhanced charge yield of the optical field emitter arrays.

Based on the theoretical investigations in this thesis, future work will primarily focus on the experiments, including:

(1) Fabrication of the optical field emitter arrays that produces highly uniform and dense nanostructure arrays, meeting the requirements on periodic patterns and charge yield imposed by the emittance-exchange ICS X-ray sources;

(2) Optical characterization of the optical field emitter arrays that confirms the emitter structure is optimized so that strong optical response can be achieved at the drive laser frequency;

(3) Electron emission test of the optical field emitter arrays that characterizes important parameters including emittance, charge yield, and quantum efficiency;

(4) Final experiment with acceleration, emittance-exchange, and ICS components of the X-ray source where the system performance can be examined.

Bibliography

[1] Thomson, J. J. (1897). XL. cathode rays. *The London, Edinburgh, and Dublin Philosophical Magazine and Journal of Science, 44*(269), 293-316.

[2] Fowler, R. H., & Nordheim, L. (1928). Electron emission in intense electric fields. *Proceedings of the Royal Society of London.Series A, Containing Papers of a Mathematical and Physical Character, 119*(781), 173-181.

[3] Spindt, C. (1968). A thin-film field-emission cathode. *Journal of Applied Physics, 39*(7), 3504-3505.

[4] Dantus, M., Kim, S. B., Williamson, J. C., & Zewail, A. H. (1994). Ultrafast electron diffraction. 5. experimental time resolution and applications. *The Journal of Physical Chemistry, 98*(11), 2782-2796.

[5] Zewail, A. H. (2006). 4D ultrafast electron diffraction, crystallography, and microscopy. *Annu.Rev.Phys.Chem., 57*, 65-103.

[6] Lobastov, V. A., Srinivasan, R., & Zewail, A. H. (2005). Four-dimensional ultrafast electron microscopy. *Proceedings of the National Academy of Sciences of the United States of America, 102*(20), 7069-7073.

[7] Graves, W. S., Kaertner, F. X., Moncton, D. E., & Piot, P. (2012). Intense superradiant x rays from a compact source using a nanocathode array and emittance exchange. *Physical Review Letters, 108*(26), 263904.

[8] Hommelhoff, P., Sortais, Y., Aghajani-Talesh, A., & Kasevich, M. A. (2006). Field emission tip as a nanometer source of free electron femtosecond pulses. *Physical Review Letters, 96*(7), 077401.

[9] Hommelhoff, P., Kealhofer, C., & Kasevich, M. A. (2006). Ultrafast electron pulses from a tungsten tip triggered by low-power femtosecond laser pulses. *Physical Review Letters, 97*(24), 247402.

[10] Ropers, C., Solli, D., Schulz, C., Lienau, C., & Elsaesser, T. (2007). Localized multiphoton emission of femtosecond electron pulses from metal nanotips. *Physical Review Letters, 98*(4), 043907.

[11] Barwick, B., Corder, C., Strohaber, J., Chandler-Smith, N., Uiterwaal, C., & Batelaan, H. (2007). Laser-induced ultrafast electron emission from a field emission tip. *New Journal of Physics, 9*(5), 142.

[12] Yanagisawa, H., Hafner, C., Doná, P., Klöckner, M., Leuenberger, D., Greber, T., . . . Osterwalder, J. (2009). Optical control of field-emission sites by femtosecond laser pulses. *Physical Review Letters, 103*(25), 257603.

[13] Bormann, R., Gulde, M., Weismann, A., Yalunin, S., & Ropers, C. (2010). Tip-enhanced strong-field photoemission. *Phys.Rev.Lett, 105*(14), 147601.

[14] Schenk, M., Krüger, M., & Hommelhoff, P. (2010). Strong-field above-threshold photoemission from sharp metal tips. *Physical Review Letters, 105*(25), 257601.

[15] Krüger, M., Schenk, M., & Hommelhoff, P. (2011). Attosecond control of electrons emitted from a nanoscale metal tip. *Nature, 475*(7354), 78-81.

[16] Thomas, R., & Nathanson, H. (1972). Photosensitive field emission from silicon point arrays. *Applied Physics Letters, 21*(8), 384-386.

[17] Schroder, D. K., Thomas, R. N., Vine, J., & Nathanson, H. (1974). The semiconductor field-emission photocathode. *Electron Devices, IEEE Transactions on, 21*(12), 785-798.

[18] Aboubacar, A., Dupont, M., Gardes, J., Laguna, M., Querrou, M., & Says, L. (1994). Electron beams triggered by a laser pulse of a few tens ns duration from silicon cathodes with array of tips in high electric field. *Nuclear Instruments and Methods in Physics Research Section A: Accelerators, Spectrometers, Detectors and Associated Equipment, 340*(1), 74-79.

[19] Aboubacar, A., Aussoleil, E., Bergeret, H., Chbihi, A., Dupont, M., Gardes, J., . . . Marie, D. (1997). Silicon photocathodes with array of tips in a photo-injector. *Applied Surface Science, 111*, 246-250.

[20] Liu, K. X., Chiang, C., & Heritage, J. P. (2005). Photo-response measurements and temporal analyses of gated p-silicon field emitter array. *Vacuum Nanoelectronics Conference, 2005. IVNC 2005. Technical Digest of the 18th International,* 242-243.

[21] Chiang, C., Yankelevich, D. R., & Heritage, J. P. (2009). Picosecond photoassisted electron emission from gated< equation> p</equation>-silicon high density field emitter array. *Journal of Applied Physics, 106*(8), 084505-084505-6.

[22] Hudanski, L., Minoux, E., Gangloff, L., Teo, K. B., Schnell, J., Xavier, S., . . . Legagneux, P. (2008). Carbon nanotube based photocathodes. *Nanotechnology, 19*(10), 105201.

[23] Zeier, W. A., Kovaleski, S. D., & Mcdonald, K. F. (2009). Electron emission from thin film optically enhanced nano-forest cathodes. *Dielectrics and Electrical Insulation, IEEE Transactions on, 16*(4), 1088-1092.

[24] Mustonen, A., Beaud, P., Kirk, E., Feurer, T., & Tsujino, S. (2011). Five picocoulomb electron bunch generation by ultrafast laser-induced field emission from metallic nano-tip arrays. *Applied Physics Letters, 99*(10), 103504-103504-3.

[25] Irvine, S., Dechant, A., & Elezzabi, A. (2004). Generation of 0.4-keV femtosecond electron pulses using impulsively excited surface plasmons. *Physical Review Letters, 93*(18), 184801.

[26] Iwami, K., Ida, K., & Umeda, N. (2011). Gold-tip cathodes for plasmon-assisted field emitter array. *Vacuum Nanoelectronics Conference (IVNC), 2011 24th International,* 79-80.

[27] Nagel, P. M., Robinson, J. S., Harteneck, B. D., Pfeifer, T., Abel, M. J., Prell, J. S., . . . Leone, S. R. (2013). Surface plasmon assisted electron acceleration in photoemission from gold nanopillars. *Chemical Physics, 414*, 106-111.

[28] Li, R., To, H., Andonian, G., Feng, J., Polyakov, A., Scoby, C., . . . Musumeci, P. (2013). Surface-plasmon resonance-enhanced multiphoton emission of high-brightness electron beams from a nanostructured copper cathode. *Physical Review Letters, 110*(7), 074801.

[29] Polyakov, A., Senft, C., Thompson, K., Feng, J., Cabrini, S., Schuck, P., . . . Hess, W. P. (2013). Plasmon-enhanced photocathode for high brightness and high repetition rate X-ray sources. *Physical Review Letters, 110*(7), 076802.

[30] Binh, V. T., Garcia, N., & Purcell, S. (1996). Electron field emission from atom-sources: Fabrication, properties, and applications of nanotips. *Advances in Imaging and Electron Physics, 95*, 63-153.

[31] Keldysh, L. (1965). Ionization in the field of a strong electromagnetic wave. *Sov.Phys.JETP, 20*(5), 1307-1314.

[32] Novotny, L., & Hecht, B. (2012). *Principles of nano-optics* Cambridge university press.

[33] Sommerfeld, A. (1899). Ueber die fortpflanzung elektrodynamischer wellen längs eines drahtes. *Annalen Der Physik, 303*(2), 233-290.

[34] Zenneck, J. (1907). Propagation of plane EM waves along a plane conducting surface. *Ann.Phys.(Leipzig), 23*(1), 907.

[35] Jackson, J. D., & Fox, R. F. (1999). Classical electrodynamics. *American Journal of Physics, 67*, 841.

[36] Maier, S. A. (2007). *Plasmonics: Fundamentals and applications* Springer.

[37] Bohren, C. F., & Huffman, D. R. (1983). Absorption and scattering by a sphere. *Absorption and Scattering of Light by Small Particles,* , 82-129.

[38] Kreibig, U., & Vollmer, M. (1995). Optical properties of metal clusters.

[39] Van der Zande, Bianca MI, Böhmer, M. R., Fokkink, L. G., & Schönenberger, C. (1997). Aqueous gold sols of rod-shaped particles. *The Journal of Physical Chemistry B, 101*(6), 852-854.

[40] Hutter, E., & Fendler, J. H. (2004). Exploitation of localized surface plasmon resonance. *Advanced Materials, 16*(19), 1685-1706.

[41] Lee, K., & El-Sayed, M. A. (2005). Dependence of the enhanced optical scattering efficiency relative to that of absorption for gold metal nanorods on aspect ratio, size, end-cap shape, and medium refractive index. *The Journal of Physical Chemistry B, 109*(43), 20331-20338.

[42] Eustis, S., Hsu, H., & El-Sayed, M. A. (2005). Gold nanoparticle formation from photochemical reduction of Au3 by continuous excitation in colloidal solutions. A proposed molecular mechanism. *The Journal of Physical Chemistry B, 109*(11), 4811-4815.

[43] Mie, G. (1908). Beiträge zur optik trüber medien, speziell kolloidaler metallösungen. *Annalen Der Physik, 330*(3), 377-445.

[44] Ma, H., Bendix, P. M., & Oddershede, L. B. (2012). Large-scale orientation dependent heating from a single irradiated gold nanorod. *Nano Letters, 12*(8), 3954-3960.

[45] Baffou, G., Quidant, R., & García de Abajo, F Javier. (2010). Nanoscale control of optical heating in complex plasmonic systems. *ACS Nano, 4*(2), 709-716.

[46] Baffou, G., Quidant, R., & Girard, C. (2010). Thermoplasmonics modeling: A Green's function approach. *Physical Review B, 82*(16), 165424.

[47] Sun, C., Vallee, F., Acioli, L., Ippen, E., & Fujimoto, J. (1993). Femtosecond investigation of electron thermalization in gold. *Physical Review B, 48*(16), 12365.

[48] Sun, C., Vallee, F., Acioli, L., Ippen, E., & Fujimoto, J. (1994). Femtosecond-tunable measurement of electron thermalization in gold. *Physical Review B, 50*(20), 15337.

[49] Ahmadi, T. S., Logunov, S. L., & El-Sayed, M. A. (1996). Picosecond dynamics of colloidal gold nanoparticles. *The Journal of Physical Chemistry, 100*(20), 8053-8056.

[50] Perner, M., Bost, P., Lemmer, U., Von Plessen, G., Feldmann, J., Becker, U., . . . Schmidt, H. (1997). Optically induced damping of the surface plasmon resonance in gold colloids. *Physical Review Letters, 78*(11), 2192.

[51] Link, S., Burda, C., Nikoobakht, B., & El-Sayed, M. (1999). How long does it take to melt a gold nanorod?: A femtosecond pump–probe absorption spectroscopic study. *Chemical Physics Letters, 315*(1), 12-18.

[52] Link, S., Burda, C., Mohamed, M., Nikoobakht, B., & El-Sayed, M. (1999). Laser photothermal melting and fragmentation of gold nanorods: Energy and laser pulse-width dependence. *The Journal of Physical Chemistry A, 103*(9), 1165-1170.

[53] Horiguchi, Y., Honda, K., Kato, Y., Nakashima, N., & Niidome, Y. (2008). Photothermal reshaping of gold nanorods depends on the passivating layers of the nanorod surfaces. *Langmuir, 24*(20), 12026-12031.

[54] Bendix, P. M., Reihani, S. N. S., & Oddershede, L. B. (2010). Direct measurements of heating by electromagnetically trapped gold nanoparticles on supported lipid bilayers. *ACS Nano, 4*(4), 2256-2262.

[55] Novotny, L., Bian, R. X., & Xie, X. S. (1997). Theory of nanometric optical tweezers. *Physical Review Letters, 79*(4), 645.

[56] Bachelot, R., HDhili, F., Barchiesi, D., Lerondel, G., Fikri, R., Royer, P., . . . Lampel, G. (2003). Apertureless near-field optical microscopy: A study of the local tip field enhancement using photosensitive azobenzene-containing films. *Journal of Applied Physics, 94*(3), 2060-2072.

[57] Zhang, W., Cui, X., & Martin, O. J. (2009). Local field enhancement of an infinite conical metal tip illuminated by a focused beam. *Journal of Raman Spectroscopy, 40*(10), 1338-1342.

[58] Johnson, P. B., & Christy, R. (1972). Optical constants of the noble metals. *Physical Review B, 6*(12), 4370.

[59] Palik, E. D. (1998). *Handbook of optical constants of solids: Index* Access Online via Elsevier.

[60] Keathley, P. D., Putnam, W. P., Sell, A., Guerrera, S., Velásquez-García, L., & Kärtner, F. X. (2012). Laser induced annealing dynamics of photo-electron spectra from silicon field emitter arrays. *CLEO: Science and Innovations,*

[61] Jensen, K. L. (2010). Space charge effects in field emission: Three dimensional theory. *Journal of Applied Physics, 107*(1), 014905-014905-9.

[62] Hobbs, R. G. *et al. Unpublished results.*

[63] Kim, S., Jin, J., Kim, Y., Park, I., Kim, Y., & Kim, S. (2008). High-harmonic generation by resonant plasmon field enhancement. *Nature, 453*(7196), 757-760.

[64] Novotny, L., & van Hulst, N. (2011). Antennas for light. *Nature Photonics, 5*(2), 83-90.

[65] Sherry, L. J., Chang, S., Schatz, G. C., Van Duyne, R. P., Wiley, B. J., & Xia, Y. (2005). Localized surface plasmon resonance spectroscopy of single silver nanocubes. *Nano Letters, 5*(10), 2034-2038.

[66] Knight, M. W., Wu, Y., Lassiter, J. B., Nordlander, P., & Halas, N. J. (2009). Substrates matter: Influence of an adjacent dielectric on an individual plasmonic nanoparticle. *Nano Letters, 9*(5), 2188-2192.

[67] Zhu, S., Chen, T., Cen, Z., Goh, E., Yu, S., Liu, Y., & Liu, Y. (2010). Split of surface plasmon resonance of gold nanoparticles on silicon substrate: A study of dielectric functions. *Optics Express, 18*(21), 21926-21931.

[68] Zhang, S., Bao, K., Halas, N. J., Xu, H., & Nordlander, P. (2011). Substrate-induced fano resonances of a plasmonic nanocube: A route to increased-sensitivity localized surface plasmon resonance sensors revealed. *Nano Letters, 11*(4), 1657-1663.

[69] Chen, H., Ming, T., Zhang, S., Jin, Z., Yang, B., & Wang, J. (2011). Effect of the dielectric properties of substrates on the scattering patterns of gold nanorods. *Acs Nano, 5*(6), 4865-4877.

[70] Mahmoud, M. A., Chamanzar, M., Adibi, A., & El-Sayed, M. A. (2012). Effect of the dielectric constant of the surrounding medium and the substrate on the surface plasmon resonance spectrum and sensitivity factors of highly symmetric systems: Silver nanocubes. *Journal of the American Chemical Society, 134*(14), 6434-6442.

[71] Hutter, T., Elliott, S. R., & Mahajan, S. (2013). Interaction of metallic nanoparticles with dielectric substrates: Effect of optical constants. *Nanotechnology, 24*(3), 035201.

[72] Habteyes, T. G., Dhuey, S., Wood, E., Gargas, D., Cabrini, S., Schuck, P. J., . . . Leone, S. R. (2012). Metallic adhesion layer induced plasmon damping and molecular linker as a nondamping alternative. *Acs Nano, 6*(6), 5702-5709.

[73] Hutley, M., & Maystre, D. (1976). The total absorption of light by a diffraction grating. *Optics Communications, 19*(3), 431-436.

[74] Bonod, N., Tayeb, G., Maystre, D., Enoch, S., & Popov, E. (2008). Total absorption of light by lamellar metallic gratings. *Optics Express, 16*(20), 15431-15438.

[75] Popov, E., Enoch, S., & Bonod, N. (2009). Absorption of light by extremely shallow metallic gratings: Metamaterial behavior. *Opt.Express, 17*(8), 6770-6781.

[76] Wang, W., Wu, S., Reinhardt, K., Lu, Y., & Chen, S. (2010). Broadband light absorption enhancement in thin-film silicon solar cells. *Nano Letters, 10*(6), 2012-2018.

[77] Abass, A., Shen, H., Bienstman, P., & Maes, B. (2011). Angle insensitive enhancement of organic solar cells using metallic gratings. *Journal of Applied Physics, 109*(2), 023111-023111-7.

[78] Hao, J., Zhou, L., & Qiu, M. (2011). Nearly total absorption of light and heat generation by plasmonic metamaterials. *Physical Review B, 83*(16), 165107.

[79] Wood, R. (1902). XLII. on a remarkable case of uneven distribution of light in a diffraction grating spectrum. *The London, Edinburgh, and Dublin Philosophical Magazine and Journal of Science, 4*(21), 396-402.

[80] Rayleigh, L. (1907). On the dynamical theory of gratings. *Proceedings of the Royal Society of London.Series A, Containing Papers of a Mathematical and Physical Character, 79*(532), 399-416.